SAPIENZA
UNIVERSITÀ DI ROMA

Facoltà di ingegneria civile e industriale

Dipartimento di Ingegneria Meccanica e Aerospaziale

DOTTORATO DI RICERCA IN
MECCANICA TEORICA E APPLICATA
XXXV CICLO

Towards an optimal control system of an opto-mechanical resonator for quantum noise reduction in GW interferometers

---

Candidato:
Laura Giacoppo

Tutor
Prof. Ettore Majorana

Docente guida
Prof. Antonio Carcaterra

May 12, 2023

Ai miei genitori, zio Pippo, Marcello e Marco

Contents

Introduction

The first direct detection of a gravitational wave [1] has given further evidence for Einstein's theory of General Relativity and it has placed new perspectives on the investigation of the Universe. The detection was made possible thanks to the upgrades of the second generation detectors. The limit in sensitivity of gravitational wave (GW) detectors is set by different noise sources. In particular, in the high frequency band (above 200 Hz) it is dominated by *shot noise*. This noise is due to the quantum phase fluctuation of the coherent vacuum field entering the interferometer through its output port. As a solution to this limitation, the current generation of gravitational wave detectors adopted a technique based on the injection of phase-squeezed state, an idea initially proposed by Caves in 1981 [2]. A coherent state is a minimum uncertainty state, which means it has minimum quantum fluctuations on the two orthogonal quadratures. A squeezed state belongs to another class of minimum uncertainty states, with non-classical distribution of noise, for which the fluctuations on one quadrature are lower than those of a coherent state, whereas the fluctuations on the orthogonal quadrature are higher. This class of states can be produced by degenerate parametric down-conversion processes in second-order nonlinear crystals and they were first observed in 1985 [3] in the radio-frequency band. The first sensitivity enhancement of gravitational wave detectors by means of injection of squeezed vacuum was first demonstrated by the British-German GEO interferometer [4]. Later on, the effectiveness of this technique has been largely demonstrated in gravitational wave interferometers thanks to which, in the last two years, many new GW detections have been realized [5, 6]. During the last observing run O3, the injection of phase-squeezed vacuum from the dark port of the GW interferometers (LIGO and Virgo) demonstrated the quantum noise reduction (*shot noise*) in the high-frequency region of the detection band [7, 8]. Nevertheless, frequency-independent squeezing with phase-squeezed vacuum has the counter-effect of increasing *radiation pressure noise* at low frequency (below 100 Hz) [6]. Indeed, the second generation of GW detectors, due to the sensitivity improvement,are facing the limit imposed by the quantum nature of light: the Standard Quantum Limit (SQL) [2]. Hence, in order to enhance the detector sensitivity, also at low frequencies, the injection of squeezed states with a frequency-dependent squeezing angle is necessary, meaning that the ellipse representing the noise fluctuation is frequency dependent and, at low frequency reduce the noise on amplitude, while at high frequency on phase quadrature. This scientific reason lays below the realization of table-top experiments for the production of frequency dependent squeezing (FDS) in the audio frequency band of GW detectors. The FDS technique used in current gravitational wave advanced detectors consists in the filtering of the Frequency Inde-

pendent Squeezing (FIS) by means of suitable detuned cavity, so that the squeezing ellipse will be rotated as a function of the frequency inside its linewidth [9, 10, 11]. One of the most interesting alternative techniques for FDS generation is the ponderomotive technique. In this method, squeezing is generated by exploiting the radiation pressure effect on suspended mirrors inside an optical cavity. The coupling between the fluctuations of the optical field of the laser beam (coherent light) and the mechanical motion of the mirrors, due to the radiation pressure from the laser light, the so-called *optical spring* effect, creates a phase shift, in the light reflected from the mirrors, which depends on the intensity of the laser light incident on the suspended mirror. This results in a quantum correlation between phase (*shot noise*) and amplitude noise (*radiation pressure noise*), that is called ponderomotive squeezing. We have designed a tabletop suspended interferometer with low dissipation mechanical suspensions (*monolithic suspensions*) of the main optics, named SIPS (Suspended Interferometer for Ponderomotive Squeezing), that will be sensitive to radiation pressure noise in the audio frequency band of GW detectors.

The proposal of this thesis is to study and design a highly sophisticated mechanical control for an optomechanical resonator such as SIPS, based on Pontryagin's optimal control theory. The optimal control problem is analysed considering opto-mechanical interaction models developed from the model already described in literature for acoustic waves reflection in a wave guide. Indeed, a crucial point for this type of device is the mirror motion due to external mechanical disturbances, such as vibration and acoustic noise, which can bring the interferometer out of its working point. Moreover, the nonlinear optomechanical coupling is expected to generate the emergence of spurious frequencies in the reflected light spectrum, with respect to the monochromatic incoming laser spectrum. We consider how the control on suspended mirror position could take into account such non-linear effects. To this aim, we will apply Pontryagin's approach to develop an integro-differential model that can be used to build an adequate and optimized control system, which can be implemented and tested in our small-scale suspended interferometer. As a first application, SIPS interferometer will be used to test broadband quantum noise reduction through the injection of entangled vacuum states, i.e. Einstein Podolsky Rosen (EPR) states, generated by a non-degenerate Optical Parametric Oscillator (OPO), into a radiation pressure noise limited interferometer [12]. The integration of these two experiments is an important test bench for EPR squeezing technique applied to an interferometer before any possible integration in the next future in large scale detectors. Moreover, SIPS experiment will provide both a source of squeezed states by ponderomotive effect, for a broadband quantum noise reduction, and a suitable test bench for the optimal control algorithm we propose.

In *Chapter* 1 a brief introduction on the theory if General Relativity and on gravitational wave interferometers which made possible the first GW detection is exposed. *Chapter* 2 is focused on the description of quantum noise, which is one of tha major noise sources limiting the sensitivity of GW interferometers, and on the current method used to overcome this disturbance: the squeezing technique. In *Chapter* 3 SIPS (Suspended Interferometer for Ponderomotive Squeezing), a promising squeezing experiment for quantum noise reduction in GW detectors and the main objective

of this PhD thesis work, is described. The core of the work carried out during this PhD and the major results and achievements are discussed in the final two chapters. In particular, *Chapter* 4 retraces all the work done for the local control of the main optics of SIPS, while *Chapter* 5 collects all the theoretical study and work performed on the investigation for an optimised control of SIPS interferometer.

Chapter 1

Ground-based Gravitational Wave detectors

Gravitational Waves (GWs) were predicted by the theory of General Relativity (GR) formulated by Einstein in 1915. This theory states that a mass-energy distribution determines the curvature of space-time, and the curvature itself induces the motion of masses. Therefore gravitational interaction is not simply a force acting on space-time, but a property in the structure of space-time, due to the space-time curvature. The motion of masses generates oscillation of space-time which propagates at the speed of light. These propagating phenomena are known as Gravitational Waves (GWs). To build an experiment for the detection of GWs it is necessary to understand how this radiation interacts with the detector. In particular, the effect of gravitational radiation is to change the distance between two free falling masses, and the induced displacement is proportional to the gravitational wave amplitude (very weak) and to the initial distance between them. Then, the GW detection principle is based on the measurement of the variation of distance between two free falling masses induced by a GW. The most suitable device for the detection of gravitational signal is an interferometer, that is very sensitive to the variation of the distance between its mirrors (test masses). In particular a Michelson interferometer with suspended mirrors is the most accurate instrument, since its optical configuration is optimal to detect little differential displacements in its arms. The reason for which the mirrors must be suspended is that a suspended mass, in a range of frequency higher then its oscillation frequency, has a behavior similar to that of a free falling mass. To measure GWs with frequencies of the order of a few hundreds Hz, the optimal choice would be an arm length L of several hundred kms, that is why for ground-based interferometers the solution (adopted in LIGO and VIRGO) is to use Fabry-Perot arm cavities. To increase the detector sensitivity, other cavities (power recycling, signal recycling, input and output mode-cleaner) are used. The detection bandwidth, for a ground-based interferometer, ranges from roughly 10 Hz to 10 kHz. The present most important interferometric detectors are Virgo, located in Cascina (Pisa, Italy), LIGO in the US (one in Hanford, Washington and another in Livingston, Louisiana), GEO600 in Germany (Hannover) and one in Japan (KAGRA). Another detector is under construction in India (LIGO-Indigo). Compared to the original projects, work was carried out on the Virgo and LIGO sites to increase their

sensitivity through various improvements, bringing the three interferometers to the so-called Advanced state. The inauguration of Advanced Virgo (AdV) took place on February 20, 2017. In this chapter, we will focus on the understanding of this kind of devices: starting from the description of the interaction of GW signal with ground-based interferometers, we will then describe their working principle and the fundamental noises that limit their sensitivity.

1.1 Interaction of GW with free falling masses

In order to describe the interaction between GWs and a detector it is necessary to recall some general relativity concepts, in particular two important tools are *geodesic equation* and *equation of geodesic deviation*. Consider a curve parametrized by λ, $x^\mu(\lambda)$, we can write

$$ds^2 = g_{\mu\nu}dx^\mu dx^\nu = g_{\mu\nu}\frac{dx^\mu}{d\lambda}\frac{dx^\nu}{d\lambda}d\lambda^2 \tag{1.1}$$

For a time-like curve $ds^2 < 0$,

$$c^2 d\tau^2 = -ds^2 = -g_{\mu\nu}dx^\mu dx^\nu \tag{1.2}$$

where τ is the *proper time*, that is the time measured by a clock carried along this trajectory. Hence, we can replace λ with τ so that $x^\mu = x^\mu(\tau)$, and obtain

$$g_{\mu\nu}\frac{dx^\mu}{d\tau}\frac{dx^\nu}{d\tau} = -c^2. \tag{1.3}$$

Among all possible time-like curves, fulfilling boundary conditions, $x^\mu(\tau_A) = x^\mu_A$ and $x^\mu(\tau_B) = x^\mu_B$, the classical trajectory of a point-like test mass is obtained minimizing the action, that is

$$\delta S = -m\delta\int_{\tau_A}^{\tau_B} d\tau = 0. \tag{1.4}$$

This gives

$$\frac{d^2x^\mu}{d\tau^2} + \Gamma^\mu_{\nu\rho}(x)\frac{dx^\nu}{d\tau}\frac{dx^\rho}{d\tau} = 0 \tag{1.5}$$

that is the *geodesic equation*, the classic equation of motion of a test mass in the curved background described by $g_{\mu\nu}$, in absence of external non gravitational forces. Now, let us consider two nearby geodesics, $x^\mu(\tau)$ and $x^\mu(\tau)+\xi^\mu(\tau)$, and their geodesic equation. If $|\xi^\mu(\tau)|$ is much smaller that the typical scale of variation of gravitational field, taking the difference between the two geodesic equations, and expanding to first order in ξ, we obtain the *equation of the geodesic deviation*

$$\frac{d^2\xi^\mu}{d\tau^2} + 2\Gamma^\mu_{\nu\rho}(x)\frac{dx^\nu}{d\tau}\frac{d\xi^\rho}{d\tau} + \xi^\sigma\partial_\sigma\Gamma^\mu_{\nu\rho}(x)\frac{dx^\nu}{d\tau}\frac{dx^\rho}{d\tau} = 0 \tag{1.6}$$

or, using the covariant derivative [13]

$$\frac{D^2\xi^\mu}{D\tau^2} = -R^\mu_{\nu\rho\sigma}\xi^\rho\frac{dx^\nu}{d\tau}\frac{dx^\rho}{d\tau}. \tag{1.7}$$

From this equation we can see that two near time-like geodesic are subjected to a tidal gravitational force described by the Riemann tensor. Then, writing explicitly the geodesic equation or the equation of geodesic deviation in the reference frame of interest for us, we can understand the behaviour of test masses for the corresponding observer. As detailed explaining in [13], GWs have an especially simple form in TT gauge, then it is convenient to work in the TT reference frame and to understand the physical meaning of it. To do this we start from the geodesic deviation. If test mass is at rest at $\tau = 0$, we find that

$$\begin{aligned} \frac{d^2x^i}{d\tau^2}|_{\tau=0} &= -\left[\Gamma^i_{\nu\rho}(x)\frac{dx^\nu}{d\tau}\frac{dx^\rho}{d\tau}\right]_{\tau=0} \\ &= -\left[\Gamma^i_{00}(x)\left(\frac{dx^0}{d\tau}\right)^2\right]_{\tau=0} \\ &= 0, \end{aligned} \tag{1.8}$$

where the last equality follows from the fact that $\Gamma^i_{00} = 0$ for the condition imposed. Therefore it is possible to see [13] that in this reference frame, *particles that are at rest before the arrival of a GW, stay at rest also after the wave has passed.* The TT frame coordinates stretch themselves at the passage of the wave, so that the position of detector's test masses, initially at rest remains unchanged. Obviously, the fact that test masses position does not change to the passage of a wave does not mean that a GW do not have a physical effect, but it is only due to the choice of the coordinate system. The TT gauge illustrate the fact that, since GR is invariant under coordinate transformation the physical effects are not expressed by what happens to the coordinates. In fact, in this gauge the GWs have an evident physical effect only on *proper distance* or *proper time.*
Consider two events at $(t, x_1, 0, 0)$ and at $(t, x_2, 0, 0)$ respectively. If a GW propagate along the z axis, in TT gauge the *coordinate distance* $x_1 - x_2 = L$ remains constant, while the *proper distance* is

$$\begin{aligned} s &= (x_2 - x_1)[1 + h_+ \cos\omega t]^{\frac{1}{2}} \\ &\simeq L[1 + \frac{1}{2}h_+ \cos\omega t] \end{aligned} \tag{1.9}$$

which means that proper distance is modulated by GWs. If we consider as the two test masses the two mirrors of the detector, between which a light beam (laser beam) travels back and forth, the time taken by the light to make a round trip is determined by the proper distance. Then, the fact that GWs affect exactly the proper distance means that measuring of the round trip time gives measure of the passage of GWs. Although TT frame is the more suitable for GWs, it is convenient to describe the interaction of GWs with the detector using a reference frame which takes into account the features of the detector, that is *proper detector frame.* In this frame, test masses are free to move and so to be sensitive to the passage of a GW. Considering a small region of space, even in presence of GWs the metric can

be treated as flat

$$\begin{aligned} ds^2 \simeq & -c^2dt^2\left[1+\frac{2}{c^2}\mathbf{a}\cdot\mathbf{x}+\frac{1}{c^4}(\mathbf{a}\cdot\mathbf{x})^2-\frac{1}{c^2}(\mathbf{\Omega}\times\mathbf{x})^2+R_{0i0j}x^ix^j\right] \\ & +2cdtdx^i\left[\frac{1}{c}\epsilon_{ijk}\Omega^jx^k-\frac{2}{3}R_{0jik}x^jx^k\right] \\ & +dx^idx^j\left[\delta_{ij}-\frac{1}{3}R_{ikjl}x^kx^l\right], \end{aligned} \tag{1.10}$$

where $\mathbf{a}$ is the acceleration of laboratory with respect to a local free falling frame, Ω^i is the angular velocity of laboratory, the term $\frac{1}{c^4}(\mathbf{a}\cdot\mathbf{x})^2$ is a gravitational redshift, the term $\frac{1}{c^2}(\mathbf{\Omega}\times\mathbf{x})^2$ gives Lorentz time dilatation due to the angular velocity of the laboratory, the term $\frac{1}{c}\epsilon_{ijk}\Omega^jx^k$ is called "Sagnac effect", that is the Doppler effect due to the rotation of the Earth, and finally, terms proportional to Riemann tensor contain both the effect of the gravitational backgrounds and the effect of the GWs. Choosing some particular situations (e.g., by suspending the test masses) it is possible to simplify the metric 1.10 and to reduce to the previous TT gauge case. The effect of GWs is entirely in the term $O(r^2)$ and must compete with a number of other effects of many order of magnitude. But GWs can have high frequencies compared to all other effects, so that it is possible to have a frequency window where external noise can be isolated from the signal, to obtain a significant sensitivity to the GWs. If other effects are isolated, all terms in eq. 1.10 can be neglected, except the terms proportional to Riemann tensor which represent the contribution of GWs. Applying the geodesic deviation as in equation 1.7, we obtain

$$\frac{d^2\xi^i}{d\tau^2}=-R^i_{0j0}\xi^j\left(\frac{dx^0}{d\tau}\right)^2. \tag{1.11}$$

If we consider only the linear order in h, we can write $t=\tau$ and equation 1.11 can be rewritten as

$$\ddot{\xi}^i=-c^2R^i_{0j0}\xi^j, \tag{1.12}$$

where time derivative is done with respect to the coordinate time of the proper detector frame. Because of the Riemann tensor is invariant in the linearized theory, it is possible to choose to compute it in the TT frame, where the GWs have the simplest form [13]. Hence, the equation of the geodesic deviation in the proper detector frame is

$$\ddot{\xi}^i=\frac{1}{2}\ddot{h}^{TT}_{ij}\xi^j. \tag{1.13}$$

This equation states that in the proper detector frame, the effect of GWs on a point-like mass m can be described in term of a *Newtonian force*

$$F_i=\frac{m}{2}\ddot{h}^{TT}_{ij}\xi^j \tag{1.14}$$

and therefore the effect of GWs on test masses of the detector can be described in terms of Newtonian physics. It is important to remark that the expansions at the first order in h in the computation of the equation of geodesic deviation is valid as long as $|\xi^i|$ is much smaller than the typical scale over which the gravitational field

changes substantially. This length scale for a GW is given by $\frac{\lambda}{2\pi}$. If a detector has a characteristic linear size L, the equation of geodesic deviation can be used to study its interaction with GWs if and only if

$$L \ll \frac{\lambda}{2\pi}. \tag{1.15}$$

In order to study the interaction of GWs with the detector, we use the language of proper detector frame.

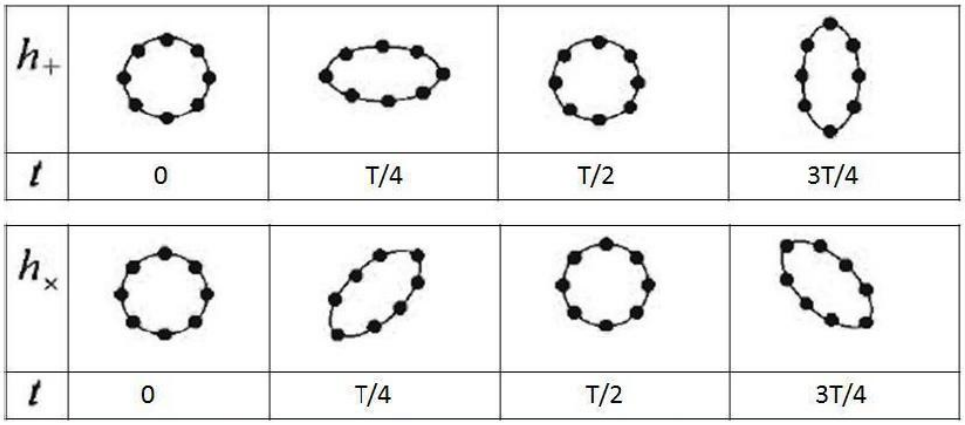

Figure 1.1: Deformation of a ring of free falling test masses due to GWs plus (+) and cross (×) polarized. The effect of plus and cross polarization is illustrated on the top and on the bottom, respectively.

We consider a ring of test masses initially at rest and we fix the origin of this reference frame in the center of the ring (see figure 1.5). Then ξ^i represents the distance of a test mass with respect to the origin itself. Let us consider a GW propagating along the z axis with + polarization, and the ring of test masses located in the plane (x, y). As mentioned before, GWs are transverse wave, then the component $\ddot{h}_{ij}^{TT}$ with $i = 3$ or $j = 3$ are zero and it is possible to see that the displacement is confined in the (x, y) plane.
GWs are transverse not only from a mathematical point of view but for their physical effect, so that test masses are physically displaced transversally with respect to their direction of propagation. To study this motion we can write for the amplitude of the GW

$$h_{ab}^{TT} = h_+ \sin\omega t \begin{pmatrix} 1 & 0 \\ 0 & -1 \end{pmatrix}, \tag{1.16}$$

where $a, b = 1, 2$ are the indices in the transverse plane. Defining (x_0, y_0) the unperturbed position and $\delta x(t)$, $\delta y(t)$ the displacement due to GW effect, we can write $\xi_a(t) = (x_0 + \delta x(t), y_0 + \delta y(t))$, then equation 1.1 becomes

$$\delta\ddot{x} = -\frac{h_+}{2}(x_0 + \delta x)\omega^2 \sin\omega t, \tag{1.17}$$

$$\delta\ddot{y} = +\frac{h_+}{2}(y_0 + \delta y)\omega^2 \sin\omega t. \tag{1.18}$$

Since δx and δy are $O(h_+)$, to linear order in h it is possible to neglect those terms with respect to the constant part x_0 and y_0. Then integrating:

$$\delta x(t) = \frac{h_+}{2} x_0 \sin \omega t, \tag{1.19}$$

$$\delta y(t) = -\frac{h_+}{2} y_0 \sin \omega t \tag{1.20}$$

and similarly, for cross polarization

$$\delta x(t) = \frac{h_\times}{2} y_0 \sin \omega t, \tag{1.21}$$

$$\delta y(t) = \frac{h_\times}{2} x_0 \sin \omega t. \tag{1.22}$$

1.2 Detection principle of Michelson interferometer

The conceptual scheme of a Michelson ITF is shown in figure 1.2. In the plane of the ITF arms, the two end mirrors can be considered in free falling condition (at least in one direction and in a specific frequency range, if properly isolated from the surrounding environment) and act as test masses. The monochromatic light beam of a laser is sent to a beam splitter (BS) which splits the two beams in two equal beams, propagating in the two orthogonal arms of the ITF and then reflected back by two end mirrors located at L_x and L_y from the BS.

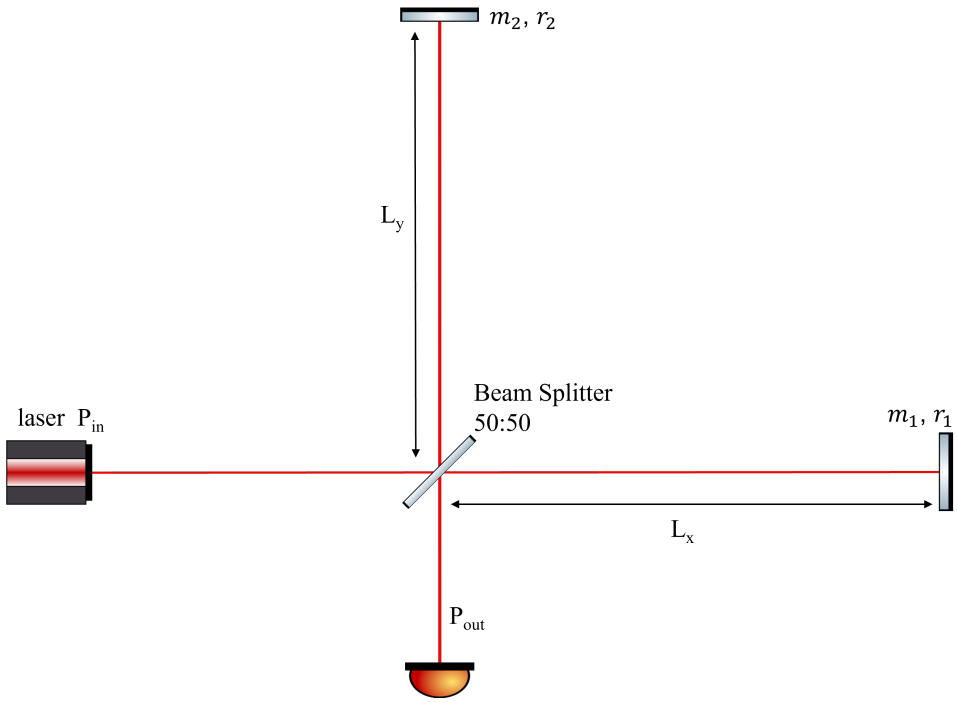

Figure 1.2: Layout of a simple Michelson ITF scheme.

After travelling back and forth through the arms, they recombine at the BS, and part of the resulting beam goes to a photodetector placed at the output port of the

ITF. Then, with this kind of device it is possible to measure the phase shift difference acquired by the two beams recombining at the BS after their paths in the ITF arms, caused by the difference in the optical path length between the two arms. If laser light is considered as a plane wave, the effect of a GW (for example + polarized and travelling perpendicularly to the ITF) can be explained as in the following [13]. If laser frequency is denoted by ω_L, then the wavelength and wavenumber of laser light are respectively $\lambda_L = \frac{2\pi}{k_\lambda}$ and $k_L = \frac{\omega_L}{c}$. The electromagnetic field coming from the laser has the form

$$E_L = E_0 e^{-i(\omega_L t + k_L x)}. \tag{1.23}$$

Considering the phase changes due to the travel time of light in the two ITF arms L_x and L_y, it is possible to find the total electric field that recombines at the BS as [13]

$$E_{out} = -iE_0 e^{-i\omega_L t + ik_L(L_x - L_y)} \sin k_L(L_x - L_y) \tag{1.24}$$

and write the power measured at the photodetector as:

$$P_{out} = |E_{out}|^2 = E_0^2 \sin^2 [k_L(L_y - L_x)], \tag{1.25}$$

where $E_0^2 = P_{in}$ is the input power, which means that any variation in the length of an arm results in a corresponding variation of the power at the photodetector. This is the starting point to understand the GW's detection principle of an interferometer, as will be explained in the next subsection.

1.2.1 Interaction of GWs in TT gauge and in proper detector frame

We recall from section 1.1 that, in the TT gauge description, a GW signal does not affect mirrors and BS coordinates, while it affects the propagation of light between the two fixed position of the mirrors. If we define the origin of the coordinate system at the position of the BS, and the position of the two mirrors in the x and y arms, respectively at the point with coordinate $(L_x, 0)$ and $(0, L_y)$, assuming that a photon leaves the BS at a time t_0, we can calculate the time of arrival of the photon after a round trip in x and y arm. Consider a plus-polarized GW

$$h_+ = h_0 \cos \omega_{gw} t, \tag{1.26}$$

after some math and neglecting terms $O(h_0^2)$ [13], we can write the time interval spent by the photon for a round-trip in the x-arm, after it leaves the BS, as:

$$t - t_0 = \frac{2L_x}{c} + \frac{L_x}{c} h(t_0 + L_x/c) \frac{\sin \omega_{gw} L_x/c}{\omega_{gw} L_x/c}, \tag{1.27}$$

where $t_0 + L_x/c$ is the value of a time t_1 at which the photon touches the end-mirror in the x-arm. The analysis is similar for the y-arm, and gives

$$t - t_0 = \frac{2L_y}{c} - \frac{L_y}{c} h(t_0 + L_y/c) \frac{\sin \omega_{gw} L_y/c}{\omega_{gw} L_y/c}. \tag{1.28}$$

This result can be physically understood if we use the proper detector frame [13], as will be explained in the following. Starting from the observation time t, i.e. the time at which the light recombines at the BS, we can use equations 1.42 1.28 to compute the value of t_0, that is the time at which light has started its round trip through x and y arms that will be inserted in the phase term for the expression of the electric field at the output. The electric fields of the light travelling in the x-arm and y-arm can be written as:

$$E^{(x)} = -\frac{1}{2}E_0 e^{-i\omega_L(t-2L/c)+i\phi_0+i\Delta\phi_x(t)}, \tag{1.29}$$

$$E^{(y)} = +\frac{1}{2}E_0 e^{-i\omega_L(t-2L/c)-i\phi_0+i\Delta\phi_y(t)} \tag{1.30}$$

and the total electric field at the output is

$$E_{tot}(t) = E^{(x)}(t) + E^{(y)}(t) = -iE_0 e^{-i\omega_L(t-2L/c)} \sin\left[\phi_0 + \Delta\phi_x(t)\right], \tag{1.31}$$

where, the phase

$$\phi_0 = k_L(L_x - L_y), \tag{1.32}$$

is a parameter that can be adjusted within the experiment by choosing the best working point of the interferometer (as we will see later), while

$$\begin{aligned} \Delta\phi_x(t) &= h_0 k_L L \frac{\sin \omega_{gw} L/c}{\omega_{gw} L/c} \cos\left[\omega_{gw}(t - L/c)\right] \\ &\equiv |\Delta\phi_x| \cos\left[\omega_{gw}(t - L/c)\right] = -\Delta\phi_y \end{aligned} \tag{1.33}$$

and the total phase difference induced by a GW in a Michelson interferometer is written as:

$$\Delta\phi_{Mich}(t) \equiv \Delta\phi_x - \Delta\phi_y = 2\Delta\phi_x. \tag{1.34}$$

In these equations, $\Delta\phi_x(t)$, is the quantity which contains the information on the effect of the GW and, in the limit $\omega_{gw}L/c \ll 1$, eq. 1.33 reduces to

$$\Delta\phi_x(t) \simeq h(t - L/c)k_L L. \tag{1.35}$$

If we compare this with eq. 1.32, we can see that the phase shift due to the GW is formally equivalent to a change of $L_x - L_y$ given by

$$\frac{\Delta(L_x - L_y)}{L} \simeq h(t - L/c) \tag{1.36}$$

The total power observed at the detection photodiode is modulated by the incoming GW signal as

$$P_{out} \sim |E_{tot}|^2 = P_{in} \sin^2\left[\phi_0 + \Delta\phi_x(t)\right] = \frac{P_{in}}{2}[1 - \cos\left(2\phi_0 + \Delta\phi_{Mich}\right)], \tag{1.37}$$

where we recalled that $\Delta\phi_{Mich} = 2\Delta\phi_x$. Clearly, it is necessary to maximize $\Delta\phi_{Mich}(t)$. This translates into the fact that the response of the interferometer is proportional to its arm-length, then to have a better sensitivity it is necessary to build interferometers with long arms. In particular, the optimal length of the arms is given by $\omega_{gw}L/c = \pi/2$ (where ω_{gw} is the frequency of the incoming GW), i.e.

$L = \lambda_{gw}/4$ [13]. Thus, in terms of $f_{gw} = \omega_{gw}/(2\pi)$, the optimal arm length depends on the frequency of the gravitational wave as

$$L \simeq 750km \left(\frac{100Hz}{f_{gw}}\right). \tag{1.38}$$

For such a value of L, the time shift induced by the GW on the light has the same sign all along its round trip in an arm, so the effect adds up. For longer arms, the GW amplitude inverts its sign during the round trip, so after this moment it starts canceling the phase shift that the light already accumulated. Then, to measure GWs with frequencies of the order of a few hundreds Hz, the optimal choice would be an arm length L of several hundred kms, which are impossible to obtain in a ground-based interferometer. That is why for this kind of interferometers the solution adopted (as in LIGO and VIRGO) is to use Fabry-Perot arm cavities, as it will be explained later in see section 1.2.3.

It is now useful, in order to better understand the physical meaning of the results of equations 1.42 and 1.28, to describe the interaction in the proper detector frame. This description is more intuitive because, in this frame, a GW does not affect the light propagation between the mirrors, while its effect is in the displacement of mirrors from their rest positions and the description is valid only in the limit of $L \ll \lambda_{gw}$, that is

$$\frac{\omega_{gw} L}{c} \ll 1. \tag{1.39}$$

Then the mirrors displacement is determined by the equation of geodesic deviation 1.1, that is, in terms of more intuitive Newtonian forces. At the same time, if we perform the computation to lowest order in $\omega_{gw}L/c$ we can consider a flat space-time metric to write the geodesic equation for mirror in both x and y arms, which can be solved in a perturbative way in h_0 and, to the zeroth order gives the equation of motion of the mirror as [13]:

$$\xi_x(t) = L_x + \frac{h_0 L}{2} \cos \omega_{gw}(t). \tag{1.40}$$

With these considerations, the round-trip time for a photon is

$$t - t_0 = \frac{2L_x}{c} + \frac{h_0 L_x}{c} \cos\left[\omega_{gw}(t_0 + L_x/c)\right]. \tag{1.41}$$

We can see that if we rewrite the eq. 1.42 in the TT gauge as

$$t - t_0 = \frac{2L_x}{c} + \frac{h_0 L_x}{c} \frac{\sin \omega_{gw} L_x/c}{\omega_{gw} L_x/c} \cos\left[\omega_{gw}(t_0 + L_x/c)\right], \tag{1.42}$$

then the equation 1.41 in the proper frame coincides with results in TT gauge, except for the function $[\sin(\omega_{gw}L_x/c)]/[\omega_{gw}L_x/c]$ replaced by 1, the lowest-order term of its Taylor expansion, as it is expected since the proper frame computation is valid only for the lowest order in $\omega_{gw}L_x/c$. This discussion shows how the proper detector frame picture is more intuitive than TT gauge description, since it allows to think in terms of Newtonian forces acting on mirrors, with the light propagating in a flat space-time. Nevertheless, this is an approximated results, while the TT gauge description allows to obtain the exact closed form of the dependence on $\omega_{gw}L_x/c$, and for this reason is much more powerful [13].

1.2.2 DC detection

We have shown that, in a Michelson interferometer, the mirrors represent the free falling masses, while the interferometer's arm-lengths are the segments located along the polarization axis in TT gauge. Let us now describe, in a more practical way, how this distance variation can be detected in such device. At the output port, where a photodetector was placed, the amplitude field is

$$E_{out} = r_{BS} t_{BS} E_{in} e^{-ik(L_x+L_y)}[r_1 e^{-ik(L_x-L_y)} + r_2 e^{ik(L_x-L_y)}], \tag{1.43}$$

where r_1 and r_2 are the reflectivity of mirror on x-arm and on y-arm respectively, while r_{BS} and t_{BS} are the reflectivity and transmissivity of the BS. Considering that the power is the complex modulus of the field amplitude, and that $|r_i|^2 = R_i$ and $|t_i|^2 = T_i$, the output power can be written as

$$P_{out} = |E_{out}|^2 = P_{in} R_{BS} T_{BS}(R_1 + R_2 + 2r_1 r_2 \cos\alpha), \tag{1.44}$$

where $\alpha \equiv 2\phi_0 = 2k_L(L_x - L_y)$ is the so-called *static tuning* [14] and it is the phase difference at the BS between the two reflected beams. It is easy to see that output power depends on the length difference of the two arms through the phase α, then, as already mentioned in the previous section, we can experimentally adjust this parameter. In particular, by changing this parameter we can obtain the maximum and minimum power. Thus, for $\alpha = 0$, which means that $L_x = L_y$, we obtain the maximum power

$$P_{max} = P_{in} R_{BS} T_{BS}(R_1 + R_2 + 2r_1 r_2), \tag{1.45}$$

while $\alpha = \pi$ gives the minimum power

$$P_{min} = P_{in} R_{BS} T_{BS}(R_1 + R_2 - 2r_1 r_2). \tag{1.46}$$

These results are consistent with the equations 1.35, 1.36 and 1.37, derived in the previous section using TT gauge, in the limit $\omega_{gw} L/c \ll 1$. By defining the *contrast* of the interferometer as

$$C = \frac{2r_1 r_2}{R_1 + R_2} = \frac{P_{max} - P_{min}}{P_{max} + P_{min}} \tag{1.47}$$

we can write the power detected at the output, also called *anti-symmetric* port as

$$P_{out} = P_{in} R_{BS} T_{BS}(R_1 + R_2)(1 + C\cos\alpha), \tag{1.48}$$

which shows that P_{out} depends only on α, and then on the difference in lengths of the two arms. If this difference is due to the passage of a gravitational wave, the beams coming back from the two arms and recombining at the BS undergo an additional different dephasing, given by the eq. 1.34. If we consider an almost perfectly 50:50 BS, which means $R_{BS} = T_{BS} = 1/2$, the power detected can be re-written taking into account this effect. Since the expected amplitude of GWs is very small, we can use the small angle approximation to obtain

$$\begin{aligned} P_{out} &= \frac{P_{in}}{4}(R_1 + R_2)[1 + C\cos(\alpha + \Delta\phi_{Mich})] = \\ &= \frac{P_{in}}{4}(R_1 + R_2)[1 + C(\cos\alpha - \sin\alpha \times \Delta\phi_{Mich})] \end{aligned} \tag{1.49}$$

which means also a variation of the power detected at the output port, expressed at first order in the gravitational wave amplitude as:

$$\begin{aligned}\delta P_{out} &= \frac{P_{in}}{4}(R_1 + R_2)C(\sin\alpha)\Delta\phi_{Mich} \\ &= \frac{P_{in}}{4}(R_1 + R_2)C(\sin\alpha)(2k_L h_0 L).\end{aligned} \tag{1.50}$$

In this computation, we consider that the term $[\sin(\omega_{gw}L_x/c)]/(\omega_{gw}L_x/c)$ is close to 1 for gravitational waves of frequency below few thousands of Hz [14]. Since the difference in length is proportional to the GW amplitude, δP_{out} directly contains the information on the quantity we are interested in, i.e. we can detect a gravitational signal using the power experimentally detected at the anti-symmetric port of the ITF. If there were no sources of noise limiting the capability to detect the power fluctuations, the best choice for the tuning of the ITF would be the one that maximizes $\sin\alpha$ in eq. 1.50. This corresponds to half of the maximum power detected at the output port, a condition usually called *gray fringe*. The tuning that give maximum and minimum powers, also given by equations 1.45 and 1.46, are called respectively *bright fringe* and *dark fringe*. The dark fringe condition is the usual working point for a GW detector (that is why the ITF output port is called dark port), and it is achieved when the configuration is such that $2k_L\Delta L = (1 + 2n)\pi$ with $n \in \mathbb{Z}$. It can be also better expressed as a relation between the optical path difference and the wavelength of the circulating light:

$$\frac{\Delta L}{\lambda_L} = \frac{1 + 2n}{4}. \tag{1.51}$$

In the ideal case, where $r_1 = r_2 = 1$, the power in eq. 1.46 would be exactly zero. In a real ITF there is a fundamental limitation to the accuracy of power measurements, given by the shot noise, which is connected to the quantum nature of light and will be better discussed in section 1.3.1. For the moment, it is enough to say that it is possible to find the best tuning for a Michelson ITF by maximizing the *signal-to-noise ratio*, written as [14]:

$$SNR(f) = \frac{1}{2}\sqrt{\frac{P_{in}}{h_p\nu}}\frac{C\sin\alpha}{\sqrt{1+\cos\alpha}}kLS_h(f), \tag{1.52}$$

where $S_h(f)$ is the *spectral density* of the gravitational wave signal, L is the average length of the two arms, and P_{in} is the input power of the interferometer, and will be better explained in section 1.3. We can write the maximum of the SNR with respect to the static tuning α as

$$\cos\alpha = \frac{-1 + \sqrt{1 - C^2}}{C}. \tag{1.53}$$

Since for highly reflective mirrors, which is usually the case of study, the contrast C is close to 1, being $\cos\alpha \simeq -1 + \sqrt{2}(1 - C)$, we can conclude that the best tuning for a Michelson ITF is when it is very close to the dark fringe condition. This detection technique is usually called *DC detection* [14].

1.2.3 Fabry-Perot cavities

In the previous section we have seen that the response of the interferometer is proportional to its arm-length, then to have a better sensitivity for measuring GWs with frequencies of the order of a few hundreds Hz, it is necessary to build long arms interferometers. Since this is technically impossible to obtain in a ground-based ITF, the solution adopted for this kind of devices, such as Virgo and LIGO, is the use of Fabry-Perot arm cavities, as shown in figure 1.3.

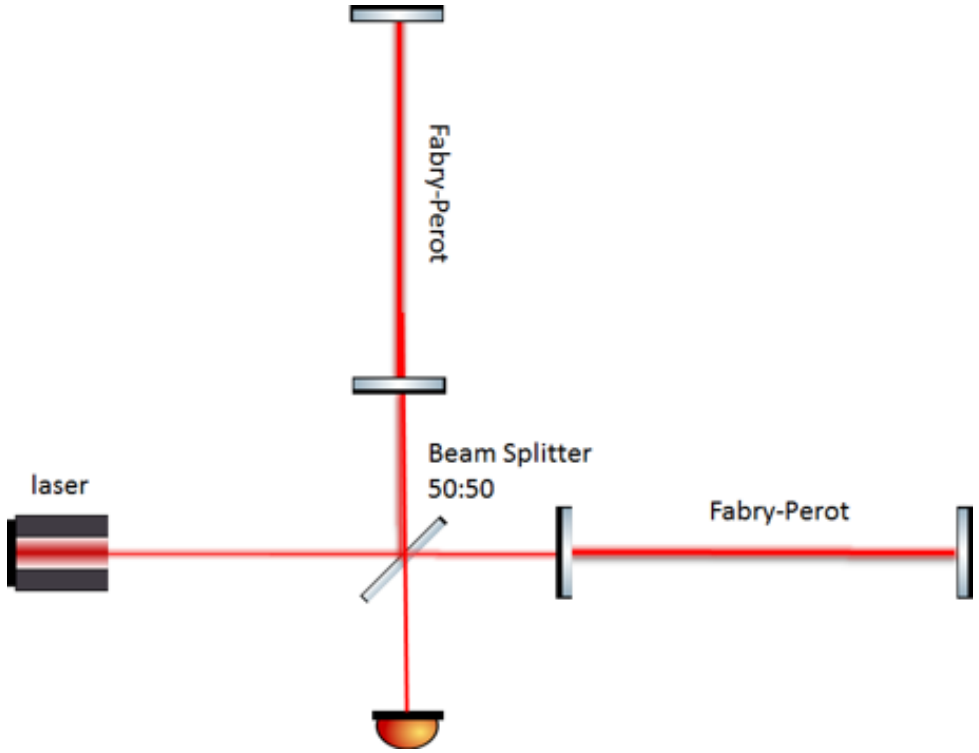

Figure 1.3: Scheme of a Michelson interferometer with Fabry-Perot cavities forming its arms.

Here, the effective length of the arms is increased by substituting them with Fabry-Perot cavities. A Fabry-Perot cavity is a linear optical resonator and when on resonance, the light is reflected back and forth inside the cavity, increasing the optical path travelled. This leads to a longer storage time for the light inside the arms and, therefore, to an enhancing of the dephasing due to gravitational waves. A detailed discussion on Fabry-Perot cavities as opto-mechanical resonators will be done in chapter 5. The cavity is on resonance when its length is tuned in order to have constructive interference between the field entering the cavity from the input mirror and the one which has done a round trip inside the cavity. This leads to an enhancement of the optical path, and then of the power stored inside the cavity, by a large factor, which is related to a parameter called **finesse** of the cavity, defined as the ratio of the free spectral range to the full width at half maximum [13]:

$$\mathcal{F} \equiv \frac{\Delta\omega_{FSR}}{\delta\omega_{FWHM}} = \frac{\pi}{2\arcsin\left(\frac{1-r_1r_2}{2\sqrt{r_1r_2}}\right)} \simeq \frac{\pi\sqrt{r_1r_2}}{1-r_1r_2}, \tag{1.54}$$

where

$$\Delta\omega_{FSR} = \pi c/L \tag{1.55}$$

is the *Free Spectral Range*, while

$$\delta\omega_{FWHM} = \frac{c}{L}\frac{1 - r_1 r_2}{\sqrt{r_1 r_2}} \tag{1.56}$$

is the *Full Width at Half Maximum*, or *linewidth* of the peak. *Finesse* is perhaps the most important parameter of an optical cavity, because it gives the information about how much the cavity is able to separate adjacent spectral orders, in relation to the linewidth. So, it can be considered as a quality factor of the cavity. The approximation in eq. 1.54 is valid for $r_1 \simeq r_2 \simeq 1$, that is the usual working condition. Speaking in terms of the phase, it can change from 0, when the cavity is not resonant, to π at resonance, and this extra phase accumulated due to a change on the length of a Fabry-Perot cavity is given by [14]:

$$\delta\phi_{FP} = \frac{2\mathcal{F}}{\pi} k_L \delta L. \tag{1.57}$$

If we compare this result with the change in phase for a simple Michelson which is

$$\delta\phi = k_L \delta L, \tag{1.58}$$

the effect of the resonant cavity is to amplify the optical response to a length change δL. If we expand around the resonant point the cavity tuning, i.e. $2k_L L = 2m\pi + \epsilon$ with $\epsilon \ll 1$, then the slope is given by:

$$\frac{d\phi}{d\epsilon} \simeq \frac{2\mathcal{F}}{\pi}. \tag{1.59}$$

Then, when on resonance, the sensitivity of the FP cavity to a phase shift is enhanced by a factor known as *optical gain* of the cavity, given by

$$G_{FP} = \frac{t_1^2}{(1 - r_1 r_2)^2} \simeq \frac{1 + r_1}{1 - r_1} \simeq \frac{2\mathcal{F}}{\pi}, \tag{1.60}$$

where we have considered the approximation for highly reflective mirrors, which is however very well verified in many cases, including GW interferometers. With this approximation, the circulating power inside the cavity is enhanced by a factor that scales linearly with the $finesse$. Moreover, a higher $finesse$, with fixed cavity length L, means narrower transmission lines, which will make the cavity locking process harder. This is the case of the complex experiment presented in this thesis and one of the main challenging goal of this work, as will be discussed in chapter 5. Since we are interested in the behaviour of a Fabry-Perot cavity as a function of the frequency, it is useful to define the *storage time*, which is the average time spent by a photon inside the cavity, defined in terms of the finesse $\mathcal{F}$ as

$$\tau_s = \frac{2L}{c}\frac{1}{1 - r_1^2} \simeq \frac{L\mathcal{F}}{c\pi}, \tag{1.61}$$

where the last expression is obtained considering $r_1 \sim 1$. Equation 1.61 shows that for a high finesse, light is trapped into the cavity for a long time. Therefore, for a Fabry-Perot ITF the response to GWs can be described in the proper detector frame, where we can obtain the result to lowest order in $\omega_{gw}L/c$. Indeed, in this frame, even in the presence of a GW the light propagates along the geodesics of flat space-time, while mirrors moves under the force exerted by GWs. This cause a change in the length of the cavity, which induces a total phase shift for the reflected field in a Fabry-Perot ITF, given by [13]:

$$\Delta\phi_{FP}(t) = |\Delta\phi_{FP}| \cos\omega_{gw}t, \tag{1.62}$$

where

$$|\Delta\phi_{FP}| = \frac{4\mathcal{F}}{\pi}k_L L h_0 \tag{1.63}$$

is the phase shift that would be induced in a Michelson ITF with arm length $2\mathcal{F}L/\pi$. From this we can assure that the optical gain $G_{FP} \simeq 2\mathcal{F}/\pi$ of a FP resonator represents not only the gain in stored power when on resonance, but also the dephasing gain of the Michelson-Fabry-Perot configuration with respect to the Michelson alone, with simply $\phi = \epsilon$ an then a unitary slope in eq. 1.59. This simply means that the effective interferometer length is amplified by a factor equal to G, and it represents the advantage of using FP cavities as the arms of a GW ITF.
Nevertheless, it is possible to show that FP cavities behave like a low-pass filter. Indeed, when the storage time is comparable to the period of the GW, as in eq. 1.52, the effects of a GW are attenuated by the cavity, and the result above is the lowest expansion in $\omega_{gw}\tau_s$. To obtain the result for a generic $\omega_{gw}\tau_s$, it is convenient to work in the TT gauge, and after some computation, already done in [13], we can write the phase shift of a Fabry-Perot Michelson ITF as

$$|\Delta\phi_{FP}| \simeq h_0 \frac{4\mathcal{F}}{\pi}k_L L \frac{1}{\sqrt{1+(f_{gw}/f_p)^2}}, \tag{1.64}$$

where, the frequency f_p is the so-called *pole frequency* and can be written as

$$f_p \equiv \frac{1}{4\pi\tau_s} \simeq \frac{c}{4\mathcal{F}L}. \tag{1.65}$$

This represents a cut-off frequency above which the effects start to be attenuated by the cavity, since it is sensitive to variation of the mirrors positions only if they happen with a frequency lower than the pole frequency f_p of the resonator. For Advanced Virgo, with Fabry-Perot cavities of $\mathcal{F} \sim 450$ and arm length of 3 km, the cut-off frequency is around 50 Hz [15]. From equation 1.64 it is easy to see that, for $f_{gw} \ll f_p$ we recover the result 1.63, found in the proper detector frame, as we expected. It is useful to define the *Transfer Function* of an interferometer with Fabry-Perot cavities, which better represents the frequency response of the device. Then, writing equation 1.64 as $|\Delta\phi_{FP}| = h_0 T_{FP}(f)$, the transfer function can be defined as [13]:

$$T_{FP}(f) \simeq \frac{4\mathcal{F}L}{\pi}k_L \frac{1}{\sqrt{1+(1+f_{gw}/f_p)^2}}. \tag{1.66}$$

This discussion demonstrates that the use of an interferometer with high finesse FP arm-cavities is the optimal choice to better amplify the GW strain signal.

1.3 Detector sensitivity

GWs signal must compete with a number of other effects that are many order of magnitudes larger. Due to the contribution of all these noises, the photodiode at the output of the ITF will continuously record a phase shift $\delta\phi$. Thus, it is necessary to achieve very high sensitivity in the frequency range of interest to reveal the GW signal. It is fundamental to understand which is the sensitivity that can be reached with a detector, defined by dominant noise sources in different frequency bands. The GW amplitude that can be detected crucially depends on the kind of signal that we are searching (burst, periodic, coalescence or stochastic signals). Since the typical GW amplitude detected on Earth is of the order of $(10^{-20} - 10^{-22})[1/\sqrt{Hz}]$ and the resulting displacement of the mirror of the ITF is $\Delta L = (1/2)h_0 L$ for $(\omega_{gw} L/c \ll 1)$, for $L = 4$ km, we have

$$\Delta L \sim 2 \times 10^{-18} m, \tag{1.67}$$

which means that it must be possible to monitor length variation of the ITF arms equal to $10^{-18} m$, that is less than the size of an atom, clearly too small. For an ITF with Fabry-Perot cavities the corresponding measured phase shift would be

$$\Delta\phi_{FP} \sim 10^{-8} rad. \tag{1.68}$$

Nevertheless, the performance of GWs detectors are limited by several disturbances, hence, it is essential to identify and suppress all noise sources which create spurious displacements of the mirrors which are not due to a GW.Therefore, in the next subsection, the dominant noise sources affecting the detector sensitivity will be described.

1.3.1 Noise sources

Noise sources in a GW ITF can be distinguished in two categories: *fundamental noises*, which are fluctuations, coming from fundamental physics principle (i.e. Heisenberg uncertainty principle), due to intrinsic properties of any physical system and, in principle, impossible to be removed, and *disturbance noises*, which are generated outside the detector and for this reason can be shielded. Noises show up as random signals so it is useful to describe them in terms of statistical quantities. Rather than the noise absolute value, is more important its size with respect to the signal, the *signal to noise ratio* (SNR), defined as the ratio between the mean square value of the signal s and that of the noise n

$$SNR = \frac{\langle s^2(t) \rangle}{\langle n^2(t) \rangle}. \tag{1.69}$$

We can define

$$s(t) = n(t) + h(t) \tag{1.70}$$

as the output signal of the detector, composed of a noise $n(t)$ and a GW signal $h(t)$, so the detection problem is to distinguish $h(t)$ from $n(t)$. This has the advantage that $n(t)$ gives a measure of the minimum value of $h(t)$ that can be detected, it is therefore the quantity that we can compare directly to the effect of incoming GWs,

expressed by $h(t)$. In order to determine the sensitivity of the detectors it is worth to define some useful quantities in the following:

- *noise spectral density*, $S_n(f)$ (or noise spectral sensitivity) measured in unit of $1/Hz$ and linked to the noise as

$$\langle n^2(t) \rangle = \int_{-\infty}^{\infty} S_n(f) df \tag{1.71}$$

- *spectral strain sensitivity*, or spectral amplitude, which is defined as $\sqrt{S_n(f)}$ and has dimension $1/\sqrt{Hz}$. If the noise increases by a factor λ, $n(t) \to \lambda n(t)$, then $S_n(f) \to \lambda^2 S_n(f)$ and the strain sensitivity scales linearly.

This quantity is plotted in the **sensitivity curve**, obtained from the square sum of the spectral densities of all the noises. It shows the minimum detectable amplitude of a signal over the frequency range in which the detector is working. Then it represents the main reference in order to understand the limits and the performances of the detector. The target is to maximize the signal caused by the passage of a GW, that is δP_{out} (see equation 1.50). In the absence of any noise, the interference condition that maximizes the sensitivity would be the *grey fringe*, meaning only half of the power arrives to the detection port (for an ideal contrast) [15]. In practice there are noises that limit the sensitivity and then the ITF working point will be different. As shown in figure 1.4, the different noise sources are dominant in a different frequency range. In particular, the lowest noise level that can be reached is the quantum noise.

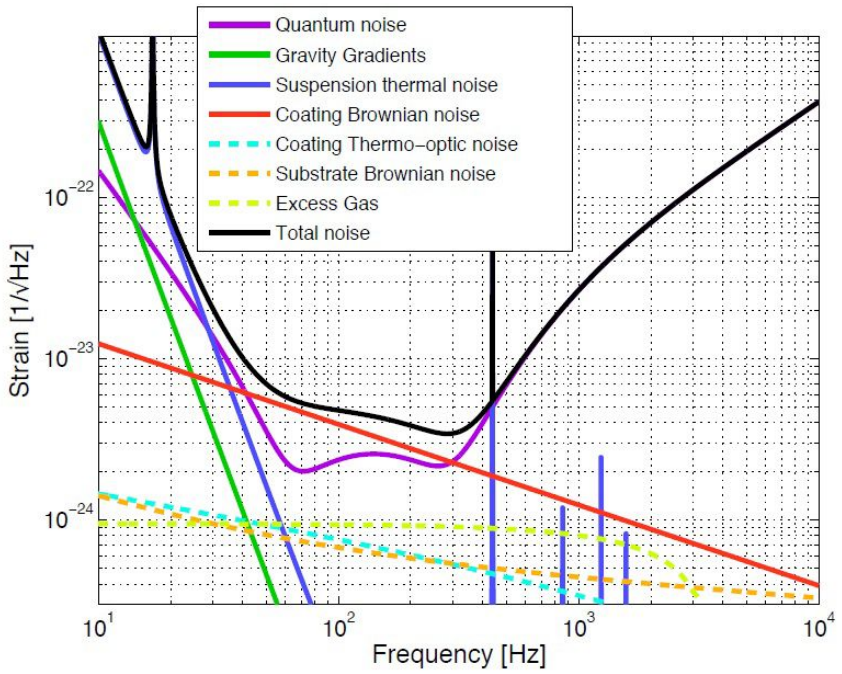

Figure 1.4: Advanced Virgo expected sensitivity curve showing noise contributions from different sources, for a full input power P=125 W [16].

First, we will focus on the component of quantum noise, which limit the sensitivity at high frequencies. Then we will present the different noises that contribute at low frequency.

1.3.2 Quantum noise

Quantum noise represents the lowest noise level that can be reached by an interferometric gravitational wave detector and is one of the most important noise sources limiting its sensitivity. For this reasons, many research and development activities are currently devoted on the study of the technique called **squeezing**, that will allow to improve the sensitivity beyond the quantum limit at high frequency and at low frequencies. This is the important goal of the research work developed in this thesis, which is important for an implementation of this technique in GW detectors in the very near future. In particular, quantum noise can be distinguished in *shot noise*, which arise from the statistical fluctuations in photons number, and *radiation pressure* fluctuations acting on the suspend mirrors of the ITF. Both these noises originate from the zero-point fluctuations (vacuum noise) of the electromagnetic field entering from the interferometer dark port and are related to the uncertainties of the two quadratures of the quantized electromagnetic vacuum field.
In the following, a semi-classical description of the quantum noise origin will be given. Nevertheless, the deep understanding of this kind of noise needs a quantum-mechanical explanation, that will be described in detail in the next chapter, together with the technique used to reduce quantum noise, the squeezing technique.

Photon shot noise
The shot noise originates from the fact that laser light comes in discrete quanta, the photons. In an interferometric detector we are interested in the measurement of the output power, that can be expressed in terms of the number n of photons collected at the photodetector, placed at the output port of the interferometer, during an observation time τ:

$$P_{out} = \langle N \rangle \frac{\hbar\omega}{\tau}. \tag{1.72}$$

As will be explained in the next chapter, the formalization of laser light as a coherent state leads to a Poisson's statistic. So, if $\langle N \rangle$ is the mean number per counting interval, then the probability distribution will be given by a Poisson distribution,

$$p(N) = \frac{\langle N \rangle^N e^{-\langle N \rangle}}{N!} \tag{1.73}$$

that, for $\langle N \rangle \ll 1$ can be approximated by a Gaussian distribution, with the standard deviation

$$\sigma = \sqrt{\langle N \rangle}. \tag{1.74}$$

Then the uncertainty on the output power measurement is

$$\sigma_P = \sqrt{\langle N \rangle}\frac{\hbar\omega}{\tau} = \sqrt{\frac{\tau P_{out}}{\hbar\omega}}\frac{\hbar\omega}{\tau} = \sqrt{\frac{\hbar\omega P_{out}}{\tau}}. \tag{1.75}$$

We now impose the condition for detecting a GW, $\delta P_{out} > \sigma_P$, that can be written as:

$$\frac{P_{in}}{4}(R_1 + R_2)(\sin\alpha)(2k_L h_0 L) > \sqrt{\frac{\hbar\omega}{\tau}\frac{P_{in}}{4}(R_1 + R_2)(1 + C\cos\alpha)/2} \tag{1.76}$$

So the smallest amplitude of the strain spectral density that we can detect due to the shot noise is [15]:

$$h_{shot} = \frac{2}{k_L L}\sqrt{\frac{\hbar\omega}{\tau P_{in}(R_1 + R_2)}}\frac{\sqrt{1 + C\cos\alpha}}{C\sin\alpha}. \tag{1.77}$$

As explained in section 1.2.2, our aim is to improve detector sensitivity by tuning the free parameters. From eq. 1.77 it can be shown [14] that, in the presence of shot noise, the optimal interference condition for an ideal interferometer is the dark fringe, that means $\alpha = (2n + 1)\pi$ with n integer number. Considering also perfect reflective mirrors, the ideal sensitivity is:

$$\widetilde{h}_{shot} = \frac{2}{k_L L}\sqrt{\frac{\hbar\omega}{P_{in}}}. \tag{1.78}$$

Referring to eq. 1.52, we can find that the minimum detectable signal is defined as the one having $SNR = 1$. For an ideal ITF, the best sensitivity is obtained with $C = 1$, but this is not possible in practice, so the sensitivity for a real ITF is given by [15]:

$$\widetilde{h}_{shot} = \frac{2}{k_L L}\sqrt{\frac{\hbar\omega}{P_{in}(R_1 + R_2)}}\frac{1}{\sqrt{1 - \sqrt{1 - C^2}}}, \tag{1.79}$$

where we have considered the equation 1.53. For an ideal ITF with a continuous wave laser with wavelength 1064 nm, 25 W of input power and Michelson arms of 1 m, the quantity $\widetilde{h}_{shot}$ is of the order of 10^{-17} $1/\sqrt{Hz}$, which is clearly not enough to detect GW signal and needs to be improved. From equation 1.78 we can see that, in order to reduce shot noise, arms with a great length L are needed. If the two arms of a Michelson interferometer are replaced by two resonant Fabry-Perot cavities, recalling section 1.2.3, the sensitivity that can be obtained is frequency dependent and the minimal strain that can be detected in this case is:

$$S_n(f) = \frac{1}{G_{FP}}\frac{1}{k_L L}\sqrt{\frac{\hbar\omega}{P_{in}(R_1 + R_2)}}\frac{1}{\sqrt{1 - \sqrt{1 - C^2}}}\sqrt{1 + \left(\frac{f_{gw}}{f_c}\right)^2}. \tag{1.80}$$

Comparing it with the expression in equation 1.79, it can be seen that the sensitivity is improved by a factor G_{FP} , which in the case of the Advanced Virgo arm cavities is ~ 290 [15]. Moreover, it is shown that also a high input power laser P_{in} is required, but this solution will cause thermal effects, because it will raise the power absorbed by the mirrors, and will also increase the other component of the quantum noise, the radiation pressure noise.

Radiation pressure noise
Radiation pressure noise is due to the statistical fluctuations of the photons that, impinging on the mirror, transfer momentum to the mirror itself, causing displacement noise. This fluctuations generate a stochastic force acting on the mirror test masses

$$F_{rad} = \frac{P_{in}}{c} \tag{1.81}$$

with power fluctuation

$$\Delta P_{in} = \hbar\omega\Delta n = \sqrt{\frac{2\pi c\hbar P_{in}\tau}{\lambda}} \tag{1.82}$$

which in the frequency domain gives the force fluctuation

$$\Delta\widetilde{F}_{rad}(\omega) = \frac{\Delta\widetilde{P}_{in}(\omega)}{c} = \sqrt{\frac{2\pi\hbar P_{in}\tau}{c\lambda}}. \tag{1.83}$$

The frequency-dependence arises from the fluctuations of the position of the mirror. Then, for a mirror of mass m and an input power P_{in} the displacement caused by the radiation pressure is

$$\Delta\widetilde{L}_{rad}(\omega) = \frac{\Delta\widetilde{F}_{rad}}{m\omega^2} = \frac{1}{m\omega^2}\sqrt{\frac{2\pi\hbar P_{in}\tau}{c\lambda}} \tag{1.84}$$

and the corresponding strain noise is

$$\widetilde{h}_{rad}(\omega) = \frac{2\Delta\widetilde{L}_{rad}(\omega)}{L} = \frac{1}{m\omega^2 L}\sqrt{\frac{8\pi\hbar P_{in}\tau}{c\lambda}}. \tag{1.85}$$

It can be noticed that the radiation pressure can be reduced again increasing L, but also decreasing P_{in}, contrary to the shot noise case: a right compromise it is then needed. The ITF mirrors respond to the force exerted by radiation pressure only at low frequencies. Then in this frequency band radiation pressure noise is higher than shot noise that, instead dominates in the high frequency band (above 300 Hz).

Standard Quantum Limit
The quadratic sum of the shot noise and the radiation pressure noise represents the total quantum noise, or *optical read-out noise*, of an ITF

$$\widetilde{h}_{total} = \sqrt{\widetilde{h}^2_{shot} + \widetilde{h}^2_{rad}}. \tag{1.86}$$

By minimizing the total quantum noise with respect to the light input power P_{in}, the resulting minimal noise can be obtained and this is called the *Standard Quantum Limit* (SQL), which is given by

$$\widetilde{h}_{SQL}(\omega) = \sqrt{\frac{4\hbar}{m\omega^2 L^2}}. \tag{1.87}$$

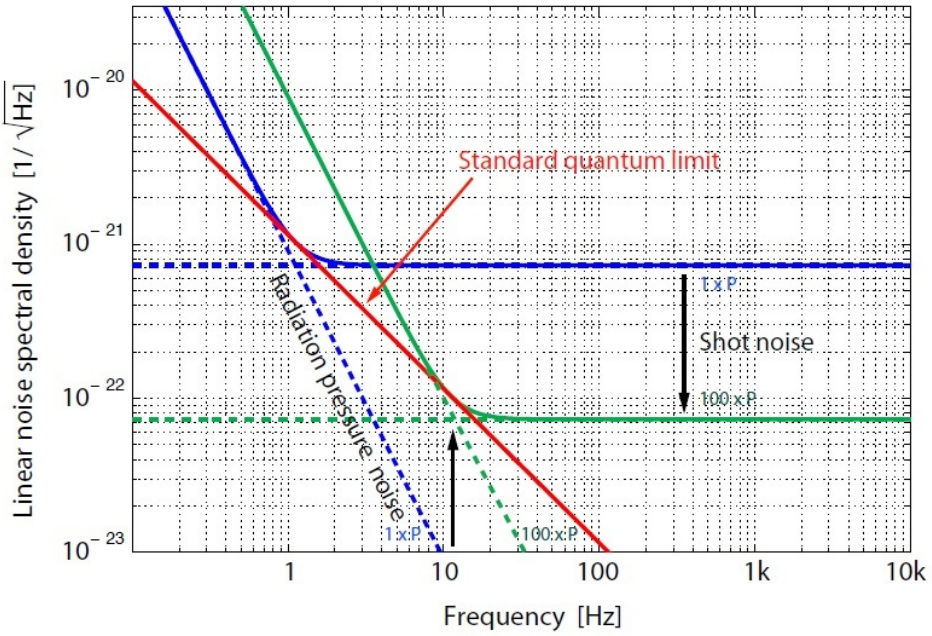

Figure 1.5: Blue curve: behaviour of the two quantum noise components at a given input power. Green curve: behaviour of these two components at a higher input power (increased by a factor 100). Red curve: The Standard Quantum Limit. In this picture, the effect of the FP cavities is not taken into account [17].

1.3.3 Thermal noise

The thermal noise is one of the most important limits to the interferometer sensitivity in the frequency band 10-300 Hz. It induces vibrations both in the mirrors and in the suspensions. The amplitude of the thermal noise in a macroscopic system is directly related to the dissipative processes occurring in the system itself, so its effect can be computed using the *the fluctuation-dissipation theorem* [18]. This theorem gives the spectral density of the force responsible for thermal fluctuations as

$$S_F(\omega) = 4kT \cdot Re[Z(\omega)], \tag{1.88}$$

where $Z(\omega)$ is the impedance of the system, that represents the resistance to the motion of the system when subjected to a force. The thermal noise affecting GW ITFs has two different origins:

- **Suspension thermal noise**
  Vibrations induced in the suspensions of the mirrors produce a *displacement noise*. In particular they are:
  - *pendulum thermal fluctuation*, which consists in a horizontal displacement of the mirrors. This is the dominant noise in 1-50 Hz frequency window;
  - *vertical thermal fluctuation*, acting on the vertical motion of the suspensions, and, although for GW interferometer it is interesting only the horizontal motion, together with the curvature of the Earth this causes a vertical-horizontal coupling order of the angle $\theta = L/2R_{earth} \simeq 2 \times 10^{-4}$;

  - *violin modes*, that is the noise due to the fluctuations of the normal modes of the wire used for the suspension of the mirrors.

- **Test-mass thermal noise**
  Thermal fluctuations within the mirror test masses themselves. They are:

  - *Brownian motion of the mirrors*, due to the kinetic energy of the atoms of the mirrors which are at a temperature T;
  - *thermo-elastic fluctuations*, which take place both in the bulk of the mirror and in the mirror coating. They are due to the thermal expansion of the material;
  - *thermo-refractive fluctuations*, due to the variation of the material refractive index of the mirror coatings with the temperature.

1.3.4 Newtonian noise

Newtonian noise, also knows as *Gravity gradient noise*, is due to the Newtonian forces of the local gravitational fields (quasi-static fields in the near region of their sources), which results in a time-varying gravitational force. It is due to the seismic waves in the ground, that produce the mass density fluctuation of the mirrors of the ITF. The Newtonian noise cannot be eliminated, since the gravitational force cannot be screened. This noise dominates in the frequency band below 5 Hz and acts directly on the mirrors bypassing their isolation system, so a ground-based detector is limited at frequency detection band below this frequency.

1.3.5 Seismic noise

The environmental disturbances such as ground vibrations induced by seismic or volcanic activity, wind, ocean activity, human activity, induce seismic noise. It is due to the coupling of the ground vibrations to the ITF mirrors by their suspension system, and significantly limits the low frequency band of the detection window (∼1-10 Hz). The strain sensitivity has the form

$$x(f) \simeq 10^{-7} \left(\frac{1Hz}{f^2} \right) mHz^{-1/2}. \tag{1.89}$$

Seismic noise is the major disturbance noise at low frequency, so it has to be reduced by a huge factor. In Virgo, to reduce the seismic noise, the mirrors are suspended through a system of mechanical pendulums in cascade in order to make the transfer function, that goes like $\sim 1/f^{2n}$ (with n number of pendulum in cascade), steeper, as simplified in figure 1.6 for the case of three filters. This chain is further suspended to an inverted pendulum. Thus giving an attenuation of the mirror motion of about 14 orders of magnitude (see figure 1.7). In Advanced Virgo this device is called *superattenuator* and is a 10-meter height system, as shown if figure 1.10.

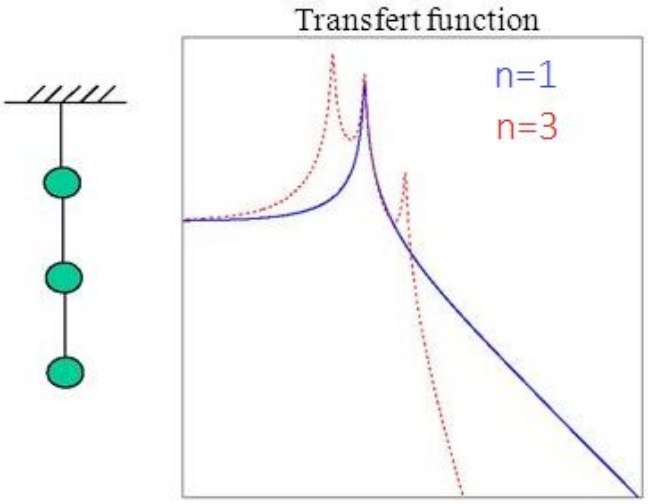

Figure 1.6: Typical transfer function of a system made by one (blue) and three (red) filtering stages.

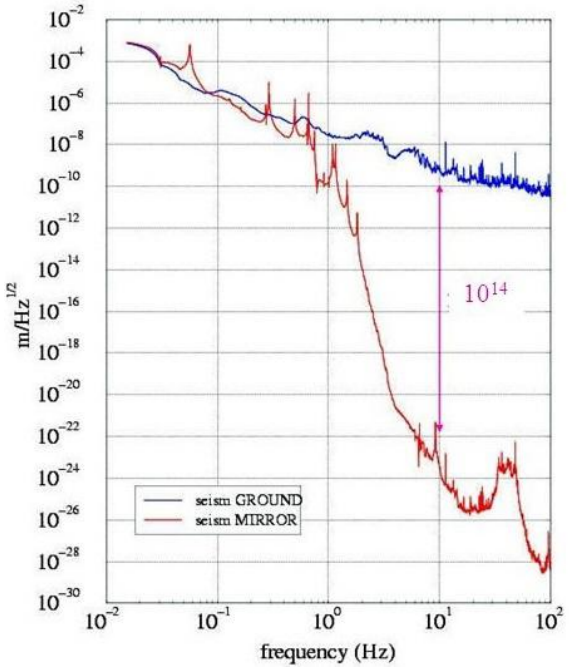

Figure 1.7: Seismic noise level before (blue curve) and after (red curve) the superattenuator filtering.

1.3.6 Homodyne detection vs frontal modulation

Even if seismic noise is attenuated in an efficient way, there is enough residual motion of the suspended mirrors which brings the cavities out of resonance and the interferometer out of the dark fringe condition. For this reason, the position of the mirrors needs to be controlled to keep the desired working point. In this section, the basic knowledge to understand the type of detection scheme used in Advanced Virgo is described, which will be the starting point for the one to be used for SIPS

experiment. Since this is one of the main topic of this thesis, it will be developed in more detail in chapter 5. The main technique used for the locking and control of the Fabry-Perot cavities in gravitational wave interferometers is the Pound-Drever-Hall (PDH) technique [19]. In GW detectors it is used to control the cavity length with respect to the wavelength of the laser which has been previously stabilized [20]. In particular, PDH technique is used to obtain the error signal, which is the key element to control a Fabry-Perot cavity since it contains the information about the length of the cavity with respect to the resonance point. An Electro Optical Modulator (EOM) is used to create the sidebands by modulating in phase the laser beam, then, accordingly to PDH technique, sidebands are added around the carrier field with a frequency shift that is chosen to be anti-resonant in the FP cavity while the carrier is resonant. In this way, they act as phase reference for the carrier which enters into the cavity, and carries information about the cavity length. The beating between sidebands and carrier is the error signal we are interested in, since it is proportional to ΔL (and thus to h) [15]. Although the PDH technique is quite simple when applied to a single resonant cavity, since the Michelson interferometer is tuned in order to be in the dark fringe condition, it is not possible to simply use the power read by a photodiode to read the GW signal. Nevertheless, it is possible to extend PDH technique to the control of a full ITF for GW detection, with the *frontal modulation* approach. Here, the laser beam is modulated at a radio-frequency, which is chosen as before in order to be anti-resonant inside the arm Fabry-Perot cavities. Since the sidebands need to reach the detection photodiode in dark fringe, to provide a phase reference, the so-called *Schnupp asymmetry* was implemented (both in Virgo and SIPS setup). It consists in adding a macroscopic difference between the two short Michelson arm, which means to make the two distances between BS and input mirrors slightly different. When the sidebands recombine at the BS, the phase difference accumulated, because of the Schnupp asymmetry, is related to the power detected at the anti-symmetric port. The photodiode will detect a power which contains a beat note coming from the interference of the carrier and the two sideband fields, then, the amplitude of this beat note, proportional to the differential displacement, can be extracted using a demodulation technique, as in the PDH scheme. In this way, the optical gain of the system will be proportional to the square root of the sideband power leaking to the antisymmetric port [21]. However, this method depends strongly on the quality of the sidebands, then, if they are noisy or largely unbalanced, there will be technical noises, such as phase and amplitude noise, that will spoil the sensitivity of the ITF. For this reason, a different signal read-out scheme has been chosen for all the Advanced GW detectors: the *Homodyne read-out*, or *DC read-out*. It consists in adding a static offset to the differential length of the arms by making one of the two cavities slightly longer than the other. This results in a small difference in the static phase of the two beams recombining at the BS and a small fraction of the carrier field leaks to the photodetector. In this way, the perfect destructive interference is spoiled when detected at the antisymmetric port. Nevertheless, this offset must be smaller than the arms resonance, in order to keep the two cavities at their correct working point, i.e. well inside their resonance width. With this scheme the static carrier field plays the role of the phase reference against which the carrier GW signal beats to provide a read-out signal. In this

configuration the power detected is proportional to the length difference between the arms, and so to the amplitude h of the GW signal. It can be seen from figure

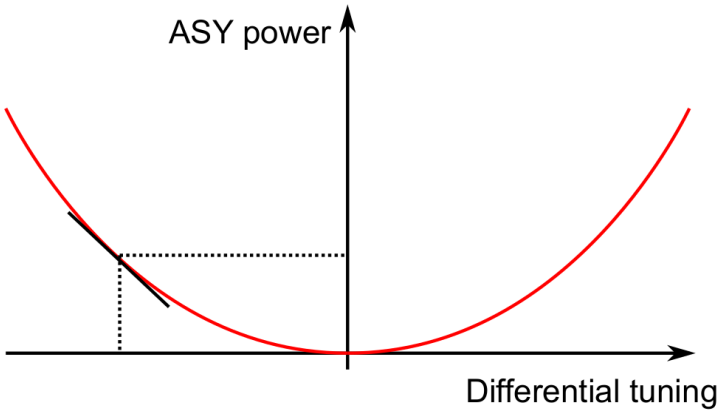

Figure 1.8: Variation of the power detected at the antisymmetric port as a function of differential tuning of the ITF, i.e. the length difference between the arm cavities [21].

1.8 that, in dark fringe, the power is almost insensitive to a differential detuning, while it is almost linear when an offset is added. It can be shown that the signal to noise ratio is independent from the value of this offset [21]. However, in the real case, any spurious field reaching the photodiode will increase the total power (and the shot noise) without increasing the optical gain and thus the signal, spoiling the sensitivity. Sidebands are one of these spurious field, but since they are still needed to control all the other lengths of the ITF, we need to filter them out before they reach the photodiode. The only way is to add an *Output Mode Cleaner* cavity before the detection photodiode, where only the carrier field will be resonant, while sidebands will be reflected out. Moreover, due to the detuning of the arm cavity lengths, the effect of radiation pressure is stronger, so it will be necessary to take it in account in the design of control system [15].

1.4 Advanced Virgo

The construction of the initial Virgo detector was completed in June 2003 and several data taking periods followed between 2007 and 2012, when it has been turned off in order to start the upgrade to the second generation detector: Advanced Virgo (AdV). AdV started its commissioning in 2016. Advanced Virgo aimed at achieving an improved sensitivity respect to the original Virgo by one order of magnitude, which corresponds to an increase of the volume of universe explored and of the detection rate by a factor of ~ 1000. AdV joined the two advanced LIGO detectors (aLIGO) for its first engineering and observing periods in May and August 2017. On 14 August 2017, LIGO and Virgo detected a signal for the first time together, GW170814, which was announced later on 27 September 2017. It was the first binary black hole merger detected by both LIGO and Virgo. Nevertheless, the first detection already occurred on the 14th September 2015 during the first observing

run of Advanced LIGO [1]. Although the working principle is the same of a simple Michelson ITF, a GW detector is a much more complicated instrument. In the following a brief description of the main components is reported (for a deep view see [22, 23]). Virgo is in principle a Michelson laser interferometer with two orthogonal

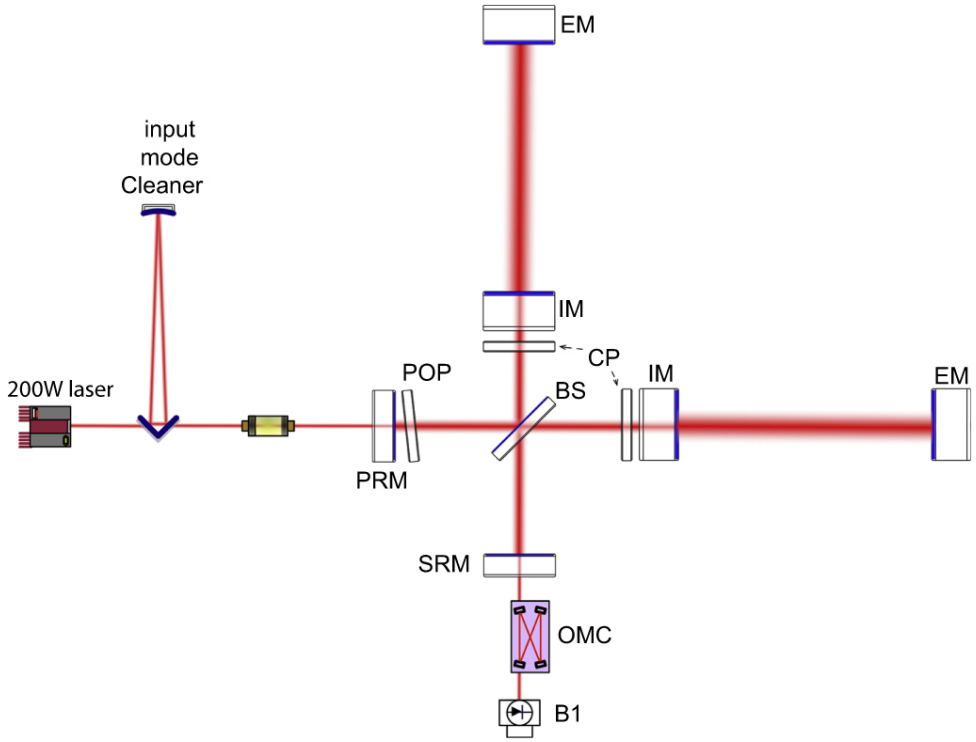

Figure 1.9: Simplified scheme of Advanced Virgo optical layout from [23]: it has a dual recycled configuration, with recycling cavities formed by the Power Recycling Mirror (PRM), the Signal Recycling Mirror (SRM), the two Input Mirrors (IM) and the two End Mirrors (EM).

arms each 3 kilometers long. A beam splitter (BS) divides the incident laser beam into two equal components sent into the two arms of the interferometer. In each arm, a two mirrors Fabry-Perot resonant cavity is implemented to extends the beam optical path from 3 to about several hundreds of kilometers. The two beams of laser light coming from the two arms are recombined out of phase on a detector so that, in principle, no light reaches the detector. The layout of the second generation of Virgo experiment is shown in figure 1.9. In order to increase the power circulating into the interferometer and then to improve the sensitivity of the detector, a *Power Recycling Mirror* (PRM) is placed in front of the laser, so that light coming back arrives in phase with the incident beam. In this way the mirrors forms another cavity (*recycling cavity*), thus increasing the light power that can reach several tens of kilowatts in the Fabry-Perot cavities. With these resonant cavities coupled together, the interferometer can be seen as a giant light trap. In the optical scheme of Virgo there are also two Mode Cleaner cavities: the Input Mode Cleaner is placed before to inject the laser light into the interferometer making sure that a good TEM_{00} mode enters the interferometer, and the Output Mode Cleaner is placed before the output photodiode, and is used to filter the signal and so to improve the signal to noise ratio.

If the optics are almost perfect and the mirror suspensions perfectly stable, no light should normally reach the detector except when the interferometer plane is crossed by a GW at the output port of the interferometer. To reach a very good stability, as previously mentioned, the mirrors are suspended by a chain of seismic filters that constitutes a very sophisticated isolation system called Superattenuator (SA)(see figure 1.10). It allows to have a very good sensitivity also at low frequencies, above

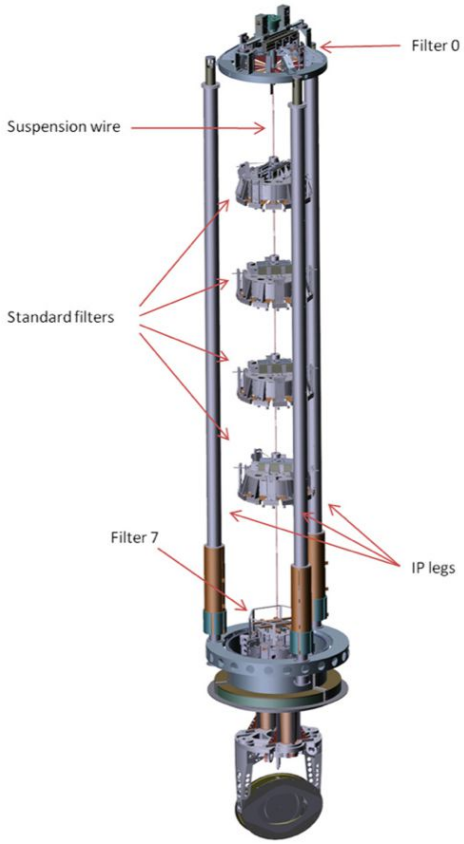

Figure 1.10: The Advanced Virgo Superattenuator (SA).

0.6 Hz, and a total attenuation of the mirror displacement of more than 10 orders of magnitude (see figure 1.6) [24, 23, 25].

1.4.1 Observational runs and main results

On September 14th, 2015, at 09:50:45 UTC, during the *first Observing Run* 'O1' the LIGO Hanford (WA) and Livingston (LA) observatories detected in coincidence the signal GW150914 [1], shown in figure 1.11. Only the LIGO detectors were observing at the time of GW150914 because of the Virgo detector was being upgraded, and GEO 600 was operating but not in observational mode because though not sufficiently sensitive to detect this event. This GW discovery provides the first robust confirmation of several theoretical predictions. It is the first direct observation of a binary Black-Hole (BH-BH) system merging to form a single BH and the first direct observation of stellar mass BHs [1]. This event inaugurates a new era of observations: the GW Astronomy. The two black holes had a mass of $M_1 = 35.4 M_\odot$

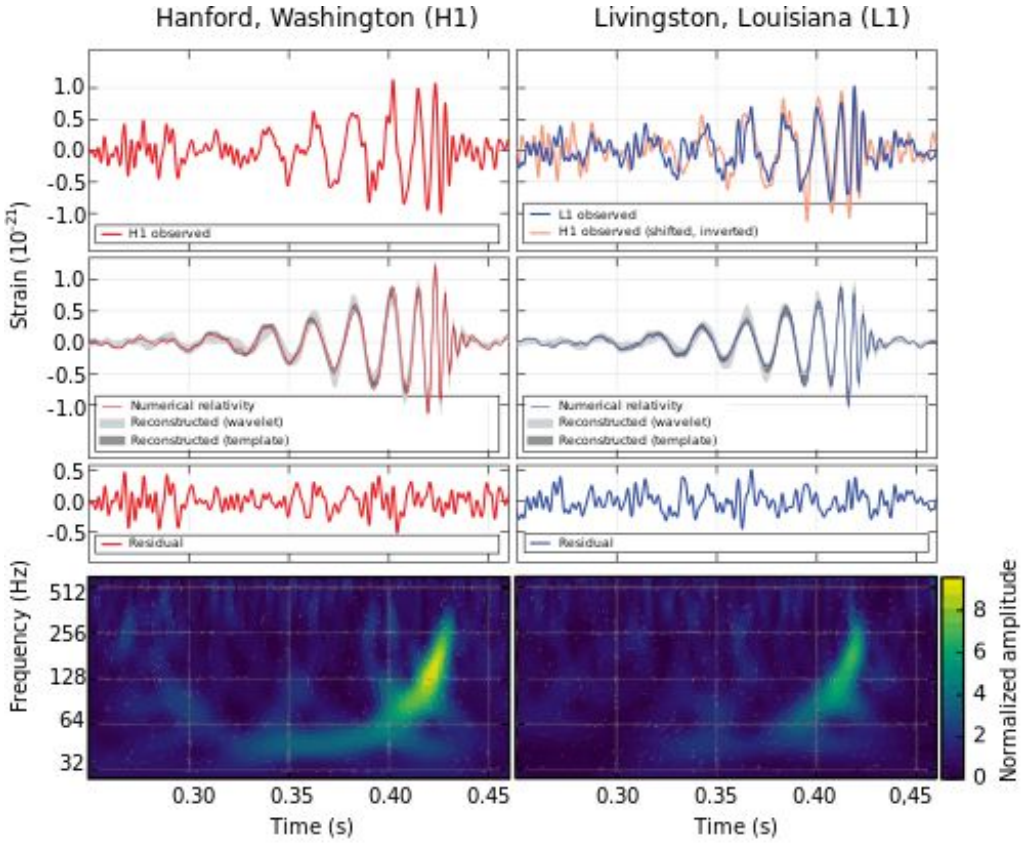

Figure 1.11: GW150914 observed by the Hanford (left column) and Livingston (right column) detectors. The top row shows the strain measured in each detector. The second row shows the GW strain projected onto each detector in the 35–350 Hz band (cutting out low and high frequencies) and a numerical relativity waveform (solid lines) for a system with parameters consistent with GW150914, and the 90% credible regions for two independent waveform reconstructions (gray). Third row shows residuals after subtracting the filtered numerical relativity waveform from the filtered detector time series. In the bottom row, a time-frequency representation of the strain data, showing the distinctive "chirp" of the signal frequency increasing over time.

and $M_1 = 29.8M_\odot$ respectively, and merged in a single black hole with a final mass of $M_{tot} = 62.2M_\odot$ and with around 3 $M_\odot$ radiated as GWs. During O1 other two signals have been detected, GW151226 and GW151012, always resulting from a BH-BH merger. After the end of the run, Advanced LIGO detectors started the installation of new upgrades in order to further improve their sensitivity. Then the second Advanced Detector Observing Run 'O2' started in November 30, 2016, first with the two LIGO detectors, then with both LIGO and Virgo instruments operating together since August 1, 2017. A fourth gravitational-wave signal coming from the merger of two stellar mass black holes located about 1.8 billion light-years away was detected on the 14 th of August 2017, at 10:30:43 UTC. GW170814 is the first event observed by the global 3-detector network, including not only the two twin Advanced LIGO detectors but the Advanced Virgo detector as well and it demonstrates the potential of a 3-detector network. During O2, a second important event

was observed on August 17, 2017, GW170817 [26]. The importance of this detection lies in the fact that it was a signal from the inspiral of two low-mass compact objects consistent with a binary neutron star (BNS) merger. So, for the first time it was possible to look at the electromagnetic counterpart of this NS-NS merger, and this detection marked the birth of the so-called multi-messenger astronomy. On April 1^{st} 2019, Virgo and LIGO twin detectors started the third Observing run, O3 [7, 8]. In particular Virgo improved the mechanism of suspension of the main mirrors with respect to those used in O2, and therefore increased the sensitivity in the low-medium frequency region, which had a deep impact in the capabilities to detect mergers of compact binary systems. A second major upgrade was the installation of a more powerful laser source, which improved the sensitivity at high frequencies. Last but not least, phase-squeezed vacuum states have been injected into Advanced Virgo, thanks to a collaboration with the Albert Einstein Institute in Hannover, Germany. This technique allowed to inject 3.2 dB of squeezing in the detector, improving the sensitivity at high frequencies (reducing shot noise). Results are shown in figure 1.12, where the improvements in sensitivity due to the use of the frequency independent squeezing (FIS) technique are highlighted.

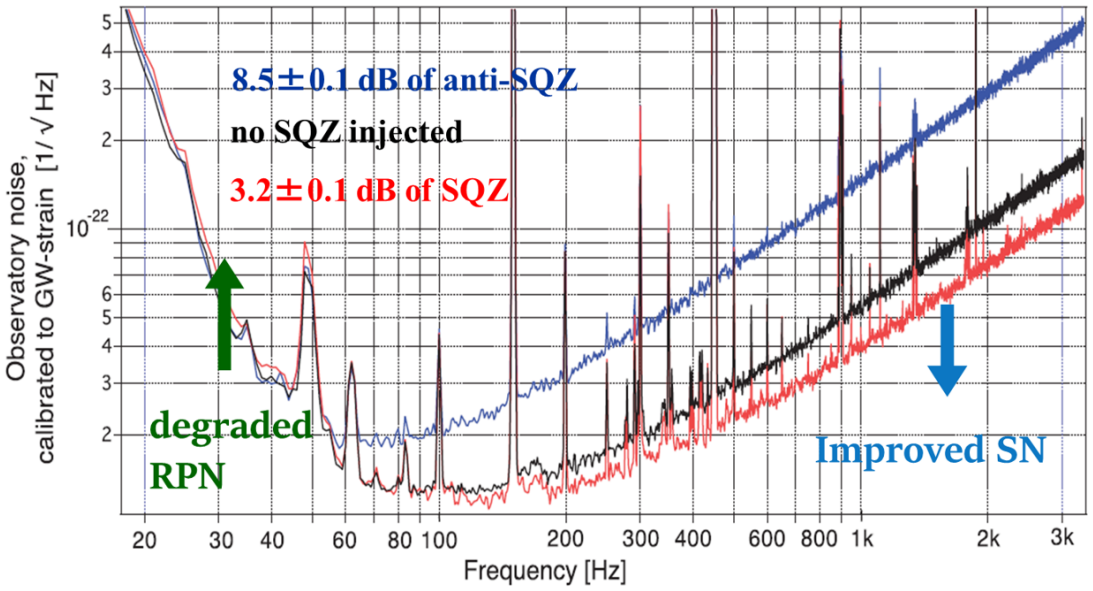

Figure 1.12: Advanced Virgo sensitivity curve in O3: 3.2 dB of frequency independent squeezing have been injected, improving the ITF sensitivity at high frequencies, while degrading it in the low frequency region [6].

Chapter 2

Quantum noise reduction in GW detectors

As introduced in the previous Chapter, quantum noise is one of the most important noise sources that limits the sensitivity of an interferometric gravitational wave detector. It is characterized by two contributions: *shot noise*, which arises from the statistical fluctuations in photons number, and *radiation pressure noise*, due to the statistical fluctuations of the photons that, impinging on the mirror, generate a stochastic force acting on the mirror itself, and causing a displacement noise. Both these noises originate from the zero-point fluctuations (vacuum noise) of the electromagnetic field entering the interferometer dark port and are manifestations of the fluctuations of the two vacuum field quadratures.

Considering a perfectly balanced Michelson interferometer (same arm length L and same mirror mass M), with an input power P_0, the quantum noise, or *optical readout noise*, can be written in terms of strain power spectral density as [27]:

$$S_{h_n h_n}(\Omega) = \frac{2\hbar}{ML^2\Omega^2}\left(K_{M_i} + \frac{1}{K_{M_i}}\right), \tag{2.1}$$

where

$$K_{M_i} = \frac{4\omega_0 P_0}{c^2 M\Omega^2}. \tag{2.2}$$

Minimizing the total quantum noise with respect to the input light power P_0 means that $K_{M_i} = 1$, so the resulting minimum noise is called the *Standard Quantum Limit* (SQL), and it is given by [27]

$$S^{\mathrm{SQL}}_{h_n h_n}(\Omega) = \frac{4\hbar}{ML^2\Omega^2} = h^2_{\mathrm{SQL}}. \tag{2.3}$$

In particular, the SQL can be described as the limit on the accuracy with which any position sensing device can determine the position of a free mass in the absence of correlations between shot noise (SN) and radiation pressure noise (RPN). Since Advanced Virgo had the aim of a gain of a factor 10 in the sensitivity of the instrument, it is necessary to increase the power of the input laser (>100W) in the Fabry- Perot cavities, this leads the detector to deal with the SQL (see figure 1.5).

For this reason it is necessary to develop methods to overcome this limit, which is one of the aim of the experiment presented in this PhD research work. Currently, the main technique used for the reduction of quantum noise, and therefore for the realization of a *Quantum Non-Demolition* (QND) interferometer, is the **squeezing** technique, that consists in the injection of squeezed states of light, which modifies the input field of the interferometer. Since vacuum fluctuations have not a classical analogous, a quantum mechanical description of the fields is necessary. This chapter briefly presents the essential theoretical models of quantum mechanics and the mathematical tools needed to describe the experiment presented in this thesis. In particular the radiation field in the context of the quantization of light and after this, the basics of quantum states of light, and finally the balanced homodyne method for the squeezed light detection will be described.

2.1 Quantum mechanical formalism

A treatment of the quantization of the electromagnetic field inside the interferometer is approached by exploiting the analogies between the electromagnetic field and the quantum mechanical harmonic oscillator. The starting point are the Maxwell equations in vacuum

$$\begin{aligned} \vec{\nabla}\cdot\vec{E} &= 0 & \vec{\nabla}\times\vec{E}+\frac{\partial B}{\partial t} &= 0 \\ \vec{\nabla}\cdot\vec{B} &= 0 & \vec{\nabla}\times\vec{B}-\mu_0\epsilon_0\frac{\partial E}{\partial t} &= 0 \end{aligned} \tag{2.4}$$

where $\vec{E}$ and $\vec{B}$ are respectively the magnetic and the electric field. From these equations it is easy to obtain the wave equation satisfied by any electric field

$$\nabla^2\vec{E}-\mu_0\epsilon_0\frac{\partial^2 E}{\partial t^2}=0. \tag{2.5}$$

If we consider a linear cavity of length L with perfectly reflective mirrors oriented along the field propagation axis z, a class of solutions of equation 2.5 are standing waves confined in the cavity. For simplicity, below, we will only deal with the electric field, considering the corresponding operator in a single mode and assume it as a monochromatic field to be polarized with a fixed linear polarization along the x-direction. With these assumptions, the solution of the equation 2.5 is

$$\vec{E}(r,t)=\hat{e}_x E_x(z,t)=\hat{e}_x\left(\frac{2\omega^2}{V\epsilon_0}\right)^{1/2} q(t)\sin kz \tag{2.6}$$

where k is the wavenumber related to the frequency, ω, of the mode with $k=\omega/c$, V is the effective volume of the cavity, $\hat{e}_x$ is the polarization vector and finally $q(t)$ is a time-dependent factor with the dimension of a length, acting as a canonical position. The expression for the magnetic field $\vec{B}$, y-polarized, inside the cavity is easily obtained using the second of the equations 2.4:

$$\vec{B}(r,t)=\hat{e}_y B_y(z,t)=\hat{e}_y\left(\frac{\mu_0\epsilon_0}{k}\right)\left(\frac{2\omega^2}{V\epsilon_0}\right)^{1/2}\dot{q}(t)\cos kz \tag{2.7}$$

where $\dot{q}(t)$ will play the role of a canonical momentum for a particle of unit mass, i.e. $p(t) = \dot{q}(t)$. The total energy of the fields, stored in the cavity is described by the Hamiltonian

$$H = \frac{1}{2}\int_V (\epsilon_0 E_x^2 + \frac{1}{\mu_0} B_y^2) dV \tag{2.8}$$

which can be written in terms of the canonical variables $q(t)$ and $p(t)$ as

$$H(q,p) = \frac{1}{2}(p^2 + \omega^2 q^2) \tag{2.9}$$

and it has the same form of the Hamiltonian of an harmonic oscillator. In quantum mechanics the Hamiltonian operator for a harmonic oscillator of mass m and angular frequency ω is

$$\hat{\mathcal{H}}(q,p) = \frac{\hat{p}}{2m} + \frac{1}{2}\omega^2 \hat{q}^2, \tag{2.10}$$

where $\hat{q}$ and $\hat{p}$ are the position and momentum quantum operator, respectively. These operators correspond to the classical canonical coordinates but, whereas in classical mechanics it is possible to measure $q(t)$ and $p(t)$ at the same time t with an arbitrary precision, in quantum mechanics this is limited by the Heisenberg Uncertainty Principle:

$$\Delta\hat{q}\Delta\hat{p} \geq \frac{i\hbar}{2}, \tag{2.11}$$

being $\hat{q}$ and $\hat{p}$ two non-commutative variables, that is

$$[\hat{q}, \hat{p}] = i\hbar. \tag{2.12}$$

A quantum harmonic oscillator is, in general, described in terms of the annihilation and creation operators, respectively

$$\hat{a} = \frac{1}{\sqrt{2m\hbar\omega}}(m\omega\hat{q} + i\hat{p}) \quad \text{and} \quad \hat{a}^\dagger = \frac{1}{\sqrt{2m\hbar\omega}}(m\omega\hat{q} - i\hat{p}). \tag{2.13}$$

These two dimensionless operators are non-Hermitian and therefore not associated with observable quantities, which means they do not have a physical meaning. Nevertheless they have the advantage to simplify the calculations. Indeed, we can write $\hat{q}$ and $\hat{p}$ as

$$\hat{q} = \sqrt{\frac{\hbar}{2m\omega}}(\hat{a}^\dagger + \hat{a}) \tag{2.14}$$

$$\hat{p} = \sqrt{i\frac{m\hbar\omega}{2}}(\hat{a}^\dagger - \hat{a}) \tag{2.15}$$

Considering the commutation relation satisfied by $\hat{a}$ and $\hat{a}^\dagger$

$$[\hat{a}, \hat{a}^\dagger] = \hat{a}\hat{a}^\dagger - \hat{a}^\dagger\hat{a} = 1 \tag{2.16}$$

we can write the Hamiltonian operator as

$$\hat{\mathcal{H}} = \hbar\omega\left(\hat{a}^\dagger\hat{a} + \frac{1}{2}\right). \tag{2.17}$$

Now introducing the number operator $\hat{n}$, defined as $\hat{n} = \hat{a}^\dagger \hat{a}$, it is possible to show how the creation and annihilation operators allow to find easily the eigenstates $|n\rangle$ of the harmonic oscillator with the energy eigenvalue E_n: they are the eigenstates of the Hamiltonian of the system, such that

$$\hat{\mathcal{H}}|n\rangle = \hbar\omega \left(\hat{a}^\dagger \hat{a} + \frac{1}{2}\right)|n\rangle = E_n|n\rangle. \tag{2.18}$$

Then, multiplying the left side by $\hat{a}^\dagger$ and using the commutation relations $[\hat{a}, \hat{a}^\dagger] = 1$ it is easy to find that

$$\hat{\mathcal{H}}\hat{a}^\dagger|n\rangle = (E_n + \hbar\omega)\hat{a}^\dagger|n\rangle. \tag{2.19}$$

In the same way, it is possible to show that

$$\hat{\mathcal{H}}\hat{a}|n\rangle = (E_n - \hbar\omega)\hat{a}|n\rangle. \tag{2.20}$$

Equations 2.19 and 2.20 are the eigenvalue problems for the eigenstates $\hat{a}^\dagger|n\rangle$ with energy $E_n + \hbar\omega$ and for the eigenstates $\hat{a}|n\rangle$ with energy $E_n - \hbar\omega$, respectively. From these equations one can understand why $\hat{a}^\dagger$ is called creation operator, while $\hat{a}$ is the annihilation or destruction operator, in fact the first generates a quantum of energy $\hbar\omega$, and the second destroys it. If the annihilation operator is iteratively applied to an eigenstate $|n\rangle$ it lowers each time the energy of the system. But the energy of the harmonic oscillator cannot be negative, therefore there has to be a lowest-energy state, that is the *ground state* (or *vacuum state*) $|0\rangle$, defined by

$$\hat{\mathcal{H}}\hat{a}|0\rangle = (E_n - \hbar\omega)\hat{a}|0\rangle = 0 \tag{2.21}$$

where the last equality is due to the fact that there are no eigenvalue with an energy less than E_0, so the equation 2.21 is satisfied only if $\hat{a}|0\rangle = 0$. The ground state eigenvalue can be found from its eigenvalues equation:

$$\hat{\mathcal{H}}|0\rangle = \hbar\omega \left(\hat{a}^\dagger \hat{a} + \frac{1}{2}\right)|0\rangle = \frac{1}{2}\hbar\omega|0\rangle = E_0|0\rangle, \tag{2.22}$$

where $E_0 = \frac{1}{2}\hbar\omega$ is the lowest energy eigenvalue, and represents the energy associated with the vacuum state, the so-called *zero-point energy*, which is not zero. Now, since $E_{n+1} = E_n + \hbar\omega$, the energy eigenvalues can be rewritten in the same way of the harmonic oscillator eigenvalues:

$$E_n = \hbar\omega \left(n + \frac{1}{2}\right), \qquad n = 0, 1, 2, ... \tag{2.23}$$

Thus, the role of $\hat{a}^\dagger$ and $\hat{a}$ is, respectively, to destroy or create a quantum $\hbar\omega$ in the excitation energy of the oscillator. If one compares the last equation with eq. 2.18 the number operator $\hat{n} = \hat{a}^\dagger \hat{a}$ can be defined as

$$\hat{n}|n\rangle = n|n\rangle \tag{2.24}$$

where $|n\rangle$ are the eigenstates of $\hat{n}$, defined as *Fock states*, and form an orthogonal and complete set such that:

$$\sum_{n=0}^{\infty} |n\rangle\langle n| = 1, \qquad \langle m|n\rangle = \delta_{m,n}. \tag{2.25}$$

Then, it is easy to show that for the state $\hat{a}|n\rangle$ and $\hat{a}^\dagger|n\rangle$ we have

$$\hat{a}|n\rangle = \sqrt{n}|n-1\rangle \tag{2.26}$$

$$\hat{a}^\dagger|n\rangle = \sqrt{n+1}|n+1\rangle. \tag{2.27}$$

Last results shows that by applying recoursively the creation operator to the ground state, any state $|n\rangle$ may be generated from the ground state as:

$$|n\rangle = \frac{(\hat{a}^\dagger)^n}{\sqrt{n!}}|0\rangle \tag{2.28}$$

where n is the number of photons contained in the state of the single mode field.

2.1.1 Quadrature Operators

Creation and annihilation operators are not associated with observable quantities because they are not Hermitian. Thus, in order to handle observable quantities, it is useful to work with dimensionless position and momentum operators, the so-called *quadrature operators*, in terms of which it is possible to describe the quantized electromagnetic field. These Hermitian operators are the *amplitude* and *phase quadrature operators*, defined as:

$$\hat{X} = \sqrt{\frac{m\omega}{2\hbar}}\hat{q} = \frac{1}{2}(\hat{a}^\dagger + \hat{a}) \tag{2.29}$$

$$\hat{Y} = \sqrt{\frac{1}{2m\omega\hbar}}\hat{p} = \frac{1}{2}i(\hat{a}^\dagger - \hat{a}). \tag{2.30}$$

The inverse relations gives

$$\hat{a} = \hat{X} + i\hat{Y} \tag{2.31}$$

$$\hat{a}^\dagger = \hat{X} - i\hat{Y} \tag{2.32}$$

and, from eq. 2.17, the Hamiltonian operator can be written as

$$\hat{\mathcal{H}} = \hbar\omega\left(\hat{X}^2 + \hat{Y}^2\right). \tag{2.33}$$

Since quadrature operators satisfy the commutation relation

$$[\hat{X}, \hat{Y}] = \frac{i}{2} \tag{2.34}$$

the dimensionless Heisenberg uncertainty relation can be easily derived

$$\langle(\Delta\hat{X})^2\rangle\langle(\Delta\hat{Y})^2\rangle \geq \frac{1}{16}. \tag{2.35}$$

Inded, the mean value of the quadrature operators on a Fock state $|n\rangle$ are

$$\langle n|\hat{X}|n\rangle = \langle n|\hat{Y}|n\rangle = 0, \tag{2.36}$$

then their fluctuations on a Fock state are

$$\begin{aligned}\langle n|\hat{X}^2|n\rangle &= \frac{1}{4}\langle n|\hat{a}^2 + \hat{a}^\dagger\hat{a}^\dagger + \hat{a}^\dagger\hat{a} + \hat{a}\hat{a}^\dagger|n\rangle \\ &= \frac{1}{4}\left(2n+1\right)\end{aligned} \tag{2.37}$$

and similarly for $\hat{Y}$

$$\begin{aligned}\langle n|\hat{Y}^2|n\rangle &= -\frac{1}{4}\langle n|\hat{a}^2 + \hat{a}^\dagger\hat{a}^\dagger - \hat{a}^\dagger\hat{a} - \hat{a}\hat{a}^\dagger|n\rangle \\ &= \frac{1}{4}\left(2n+1\right).\end{aligned} \tag{2.38}$$

Therefore, the uncertainties in both quadrature are the same and the vacuum state ($n = 0$), for which in equation 2.35 equality holds, are called *minimum uncertainty states*, that is

$$\langle(\Delta\hat{X})^2\rangle_{vac} = \langle(\Delta\hat{Y})^2\rangle_{vac} = \frac{1}{4}. \tag{2.39}$$

2.1.2 Electromagnetic field quantization

At this point, we are able write the quantized electric and magnetic field operators, respectively $\hat{E}_x(z,t)$ and $\hat{B}_y(z,t)$ in terms of the creation and annihilation operators as

$$\hat{E}_x(z,t) = E_0[\hat{a}(t) + \hat{a^\dagger}(t)]\sin kz \tag{2.40}$$

$$\hat{B}_y(z,t) = B_0[\hat{a}(t) - \hat{a^\dagger}(t)]\cos kz, \tag{2.41}$$

where $\hat{a}(t)$ and $\hat{a^\dagger}(t)$ are the time-depending creation and annihilation operators defined as

$$\hat{a}(t) = \hat{a}e^{-i\omega t} \tag{2.42}$$

$$\hat{a^\dagger}(t) = \hat{a}^\dagger e^{i\omega t}, \tag{2.43}$$

while E_0 and B_0 are defined as

$$E_0 = \sqrt{\frac{\hbar\omega}{\epsilon_0 V}} \quad \text{and} \quad B_0 = \frac{\mu_0}{k}\sqrt{\frac{\epsilon_0\hbar\omega^3}{V}}. \tag{2.44}$$

From this considerations, it is possible to write the quantized electric field inside the cavity in terms of quadrature operators:

$$\hat{E}_x(z,t) = E_0 \sin kz\left[\hat{X}\cos\omega t + \hat{Y}\sin\omega t\right]. \tag{2.45}$$

In this equation, $\hat{X}$ and $\hat{Y}$ can be associated with field amplitudes oscillating out of phase with each other of 90°: this is the reason why these two operators are called *quadrature operators*. If we evaluate the average over a state $|n\rangle$ of the electric field we get:

$$\langle n|\hat{E}_x(z,t)|n\rangle = E_0 \sin kz[\langle n|\hat{a}|n\rangle + \langle n|\hat{a}^\dagger|n\rangle] = 0 \tag{2.46}$$

which means that the electric field oscillations have a null average value, but the energy density (the square of this field) is not zero, but it is

$$\langle n|\hat{E}_x^2(z,t)|n\rangle = 2E_0^2 \sin kz^2 \left(n + \frac{1}{2}\right). \tag{2.47}$$

Then, the fluctuations in the electric field are characterized by the variance on the state $|n\rangle$

$$\Delta E_x^2 = \langle (\Delta \hat{E}_x(z,t))^2 \rangle = \langle \hat{E}_x^2(z,t) \rangle - \langle \hat{E}_x(z,t) \rangle^2 \tag{2.48}$$

and, for a number state $|n\rangle$ we have

$$\Delta E_x = \sqrt{2} E_0 \sin kz \left(n + \frac{1}{2}\right)^{1/2}. \tag{2.49}$$

Therefore for all the Fock states the fluctuations of the electromagnetic field are greater than zero. This means that even when $n = 0$, the field has fluctuations, the so-called *vacuum fluctuations*. Moreover, we have seen that the Heisenberg uncertainty principle in eq. 2.35 states that it is not possible to measure simultaneously the amplitude and phase quadrature, $\hat{Y}$ and $\hat{X}$, with arbitrary precision. This limit represents the quantum noise of electromagnetic field, and the standard quantum limit mentioned in the previous chapter is then a manifestation of the Heisenberg uncertainty principle.

2.1.3 Coherent states

In a GW interferometric detector we deal with a real field generated by a laser. Number states $|n\rangle$ are not the best choice to describe quantum optic experiment in which a laser beam with intensity of several Watts is used. In fact, when the number of photons becomes very large ($n \gg 1$) it is possible to approximate the number operator as a continuous variable. Then, in this classical limit the mean of the electric field over a generic state of the system, must be

$$\langle \psi|\hat{E}_x(z,t)|\psi\rangle = E_0 \cos(\omega t - \phi), \tag{2.50}$$

where ϕ is an arbitrary phase. But, as it is shown in 2.46, this means over a number state is zero, not depending on the value of n. This property is not in agreement with the classical description of light in which, chosen a fixed point in the space, the electric field oscillates sinusoidally in time. This condition is not satisfied for the expectation value of the field operator on a number state. Therefore, for a better description of a real field, as the one generated by a laser, a new set of states must be introduced. These states, called *coherent states* and denoted by $|\alpha\rangle$, are the eigenstates of the annihilation operator:

$$\hat{a}|\alpha\rangle = \alpha|\alpha\rangle \tag{2.51}$$

where the eigenvalues α are complex numbers, since operator $|\hat{a}\rangle$ is not Hermitian. It is useful to expand this state in the basis of Fock states

$$|\alpha\rangle = \sum_{n=0}^{\infty} C_n |n\rangle. \tag{2.52}$$

Then inserting this in equation 2.51, it is possible to find the coefficients C_n, and with an iterative process [17] it follows that

$$C_n = \frac{\alpha^n}{\sqrt{n!}} C_0 \tag{2.53}$$

where the coefficient C_0 can be found using the normalization $\langle\alpha|\alpha\rangle = 1$, which leads to

$$|\alpha\rangle = e^{-\frac{1}{2}|\alpha|^2} \sum_{n=0}^{\infty} \frac{\alpha^n}{\sqrt{n!}} |n\rangle. \tag{2.54}$$

This is the general form of a coherent state. It is possible to show that, in this basis the expectation value of the electric field operator does not vanish, but looks like a classical field with sinusoidal oscillation, such as:

$$\langle\alpha|\hat{E}_x(z,t)|\alpha\rangle = 2|\alpha|\sqrt{\frac{\hbar\omega}{2\epsilon_0 V}} \sin\left(\omega t - \vec{h}\cdot\vec{r} - \theta\right) \tag{2.55}$$

which resembles the classical description of a coherent monocromatic electromagnetic wave. Then, coherent state not only yields the correct form for the field expectation values but contains also the noise of the vacuum. In fact, the fluctuations are equal to that of the vacuum state

$$\langle\alpha|(\Delta\hat{E}_x(z,t))^2|\alpha\rangle = \frac{\hbar\omega}{2\epsilon_0 V}. \tag{2.56}$$

This can be shown by using the quadrature operators for coherent states

$$\langle(\Delta\hat{X})^2\rangle_\alpha = \langle(\Delta\hat{Y})^2\rangle_\alpha = \frac{1}{4}. \tag{2.57}$$

The above statement has an important implication: a coherent state is a state of minimum uncertainty, like the ground state of a harmonic oscillator. It is evident that $|\alpha|$ is related to the field amplitude and to the expectation value of the number state operator as

$$n = \langle\alpha|\hat{n}|\alpha\rangle = |\alpha|^2 \tag{2.58}$$

which represents the mean number of photons in a state $|\alpha\rangle$. Then, the expectation value is

$$\langle\alpha|\hat{n}^2|\alpha\rangle = \langle\alpha|\hat{a}^\dagger\hat{a}\hat{a}^\dagger\hat{a}|\alpha\rangle = |\alpha|^4 + |\alpha|^2 = n^2 + n \tag{2.59}$$

which gives the fluctuation of the photon number

$$\Delta^2 n = \langle\hat{n}^2\rangle - \langle\hat{n}\rangle^2 = \langle n\rangle. \tag{2.60}$$

From this equation it follows that the probability to detect a number n of photons in a coherent state is

$$P_n = |\langle n|\alpha\rangle|^2 = e^{-|\alpha|^2}\frac{|\alpha|^{2n}}{n!} = e^{-n}\frac{\bar{n}^n}{n!} \tag{2.61}$$

which is a Poisson distribution with a mean number of photons n. This shows the link between the quantization of light and the uncertainty in the measurement of power of a laser beam.

So far we have considered the coherent states as eigenstates of the annihilation operator, but if we consider equation 2.26, we can write

$$|n\rangle = \frac{(\hat{a}^\dagger)^n}{\sqrt{n!}}|0\rangle. \tag{2.62}$$

It is possible to obtain the coherent state using the so called *displacement operator*, $\hat{D}(\alpha)$

$$\hat{D}(\alpha) = e^{\alpha\hat{a}^\dagger - \alpha^*\hat{a}}, \tag{2.63}$$

which has the following properties

$$\hat{D}^\dagger(\alpha)\hat{D}(\alpha) = \hat{D}(\alpha)\hat{D}^\dagger(\alpha) = 1 \tag{2.64}$$

$$\hat{D}^\dagger(\alpha)\hat{a}\hat{D}(\alpha) = \hat{a} + \alpha \tag{2.65}$$

$$\hat{D}^\dagger(\alpha)\hat{a}^\dagger\hat{D}(\alpha) = \hat{a}^\dagger + \alpha^*. \tag{2.66}$$

Applying this to the vacuum state $|0\rangle$, it gives

$$|\alpha\rangle = \hat{D}(\alpha)|0\rangle. \tag{2.67}$$

This means that, with the application of the displacement operator $\hat{D}$, it can be obtained a coherent state by simply "displacing" the vacuum state, as

$$\hat{a}|\alpha\rangle = e^{-\frac{1}{2}|\alpha|^2}\sum_{n=0}^{\infty}\frac{(\alpha\hat{a}^\dagger)^n}{n!}|0\rangle. \tag{2.68}$$

2.1.4 Squeezed states

It has been shown that a coherent state has equal uncertainties in both quadratures, and the vacuum state ($n = 0$), a coherent state for which in equation (2.35) equality holds, are called *minimum uncertainty states* having

$$\langle(\Delta\hat{X})^2\rangle_{vac} = \langle(\Delta\hat{Y})^2\rangle_{vac} = \frac{1}{4}. \tag{2.69}$$

Then, for the Heisenberg uncertainty principle it is not possible to simultaneously measure the two quadratures (amplitude and phase) with arbitrary precision. This limit represents the quantum noise of the electromagnetic field. There is another class of minimum uncertainty states, called *squeezed states*. They are states of electromagnetic field with non-classic distribution of noise, for which one of the quadrature fluctuations are lower than vacuum state fluctuations. Hence, a state is said to be *squeezed* if either

$$\left\langle(\Delta\hat{X})^2\right\rangle < \frac{1}{4} \qquad \text{or} \qquad \left\langle(\Delta\hat{\mathrm{Y}})^2\right\rangle < \frac{1}{4}. \tag{2.70}$$

Then, if one of the two quadratures is squeezed, the orthogonal one is said to be *anti-squeezed*. A squeezed state is mathematically generated by applying the squeezing operator on either a vacuum or a coherent state, which is written as

$$\hat{S}(\zeta) = e^{(\frac{1}{2}\zeta^*\hat{a}\hat{a} - \frac{1}{2}\zeta\hat{a}^\dagger\hat{a}^\dagger)} \tag{2.71}$$

where $\zeta = re^{i\theta}$ is the *complex squeezing parameter*, r is the modulus, called *squeezing factor* ($0 \leq r \leq \infty$), and θ is the *squeezing angle* ($0 \leq \theta \leq 2\pi$). This operator $\hat{S}(\zeta)$ is a kind of two-photon generalization of the displacement operator used to define the usual coherent states of a single-mode field and, acting on the vacuum, it creates some sort of two-photon coherent state. Indeed, it is clear that photons are created and destroyed in pairs by the action of this operator [28]. It is possible to distinguish two kind of squeezed states, the *squeezed vacuum state* and the *coherent squeezed state* (or *bright squeezed state*). Consider first the action of this operator on a generic state $|\psi\rangle$

$$|\psi_{sqz}\rangle = \hat{S}|\psi\rangle. \tag{2.72}$$

In order to compute the quadrature fluctuations of a squeezed state we need the expectation values of the annihilation and creation operators over a squeezed state.

$$\begin{aligned} \hat{S}^\dagger \hat{a} \hat{S} &= \hat{a}\cosh r - \hat{a}^\dagger e^{i\theta}\sinh r, \\ \hat{S}^\dagger \hat{a}^\dagger \hat{S} &= \hat{a}^\dagger \cosh r - \hat{a} e^{-i\theta}\sinh r. \end{aligned} \tag{2.73}$$

From this, the variances of the two quadrature operators over a squeezed state are easily computed. Considering first a squeezed vacuum state, given by

$$|\zeta\rangle = \hat{S}(\zeta)|0\rangle, \tag{2.74}$$

then the variance of quadrature operator over this state is

$$\begin{aligned} \langle \Delta^2 \hat{X} \rangle &= \frac{1}{4}[\cosh^2 r + \sinh^2 r - 2\sinh r \cosh r \cos\theta] \\ \langle \Delta^2 \hat{Y} \rangle &= \frac{1}{4}[\cosh^2 r + \sinh^2 r + 2\sinh r \cosh r \cos\theta]. \end{aligned} \tag{2.75}$$

Substituting $\theta = 0$ in equations 2.75, one obtain

$$\begin{aligned} \langle \Delta^2 \hat{X} \rangle &= \frac{1}{4}e^{-2r} \\ \langle \Delta^2 \hat{Y} \rangle &= \frac{1}{4}e^{2r} \end{aligned} \tag{2.76}$$

that is a minimum uncertainty state whose amplitude quadrature operator fluctuations are "squeezed" by a factor e^{-r}, with respect to the coherent state fluctuations (while phase quadrature operator fluctuations "anti-squeezed" by a factor e^r, with respect to the coherent state). For $\theta = \pi$, the squeezing will appear in the $\hat{Y}$ quadrature. Squeezed or anti-squeezed noise not only appears along the amplitude and phase quadrature but also in any other orthogonal quadratures. In fact this result can be generalized for any value of the squeezing angle θ, by defining rotated quadrature operator, $\hat{X}'$ and $\hat{Y}'$, as:

$$\hat{X}' + i\hat{Y}' = (\hat{X} + i\hat{Y})e^{-i\frac{\theta}{2}} \tag{2.77}$$

and equation 2.76 can be rewritten as

$$\begin{aligned} \langle \Delta^2 \hat{X}' \rangle &= \frac{1}{4}e^{-2r} \\ \langle \Delta^2 \hat{Y}' \rangle &= \frac{1}{4}e^{2r}. \end{aligned} \tag{2.78}$$

A coherent squeezed state may be obtained by applying the displacement operator and then the squeezing operator over a vacuum state $|0\rangle$

$$|\alpha, \zeta\rangle = \hat{S}(\zeta)|\alpha\rangle = \hat{S}(\zeta)\hat{D}(\alpha)|0\rangle. \tag{2.79}$$

Since the sequence of applying the squeezing and displacement operator can be switched, as shown in [29], the mean value of the number operator over a bright squeezed state can be evaluated and it is:

$$\langle \alpha, \zeta|\hat{n}|\alpha, \zeta\rangle = |\alpha|^2 + \sinh^2 r, \tag{2.80}$$

which is slightly increased compared to the photon number of a coherent state.
This means that a squeezed vacuum state has a mean number of photons $\neq 0$ and

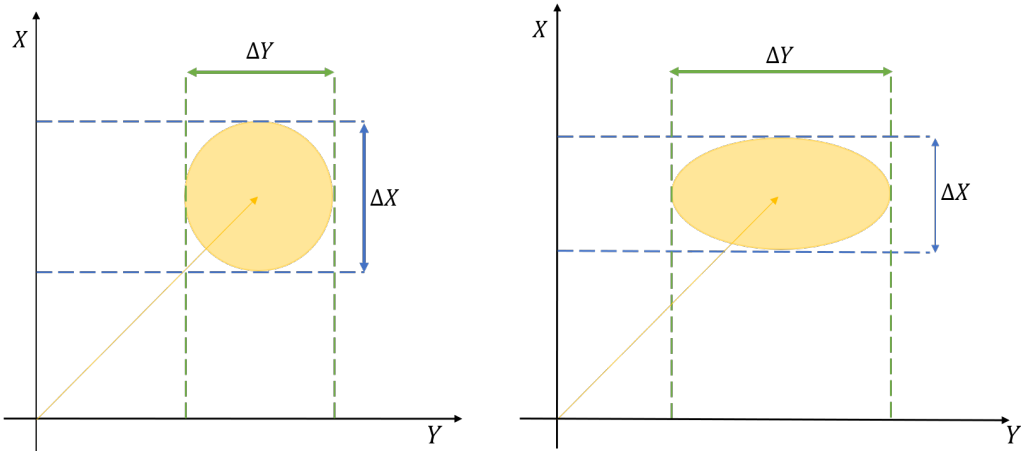

Figure 2.1: Representation of light states in quadratures space X, Y [30]. The uncertainty area for a coherent state is a circle, in which $\Delta X = \Delta Y$ (left). While a squeezed state is represented by an ellipse with the axis $\Delta X, \Delta Y$ squeezed by a factor $exp\mp\zeta$ [27].

has higher energy than the vacuum state, therefore during the squeezing process photons are generated and the energy of the state is increased. Moreover, the quantum noise characteristics are not affected by the coherent amplitude α. A simple way to graphically represent squeezing in the two-dimensional space of the quadrature operators is shown in figure 2.1. The expectation values of $\hat{X}$ and $\hat{Y}$ on a coherent state are the real and the imaginary part of the complex number α respectively. This means that the complex α-plane, up to scale factors, can be seen as a phase-space where the coherent state $|\alpha\rangle$ can be represented as in the left side of figure 2.1. In the case of a vacuum or coherent state, being the fluctuations equal in all direction, the Heisenberg uncertainty is represented by a circle around the mean value of $\hat{X}$ and $\hat{Y}$ operators, whose center is the complex number α, with modulus $|\alpha|$ and phase θ, while for a squeezed state the uncertainty area is represented by an ellipse, and then, the circle that represents the uncertainty area for a coherent state is squeezed into an ellipse (right side of figure 2.1) [30]. The squeezing level is usually expressed in dB with the following relationship:

$$V[dB] = 10 \log \left(\frac{\langle \Delta \hat{X} \rangle^2_{sqz}}{\langle \Delta \hat{X} \rangle^2_{vac}} \right) = 20 \log e^{-2r}. \tag{2.81}$$

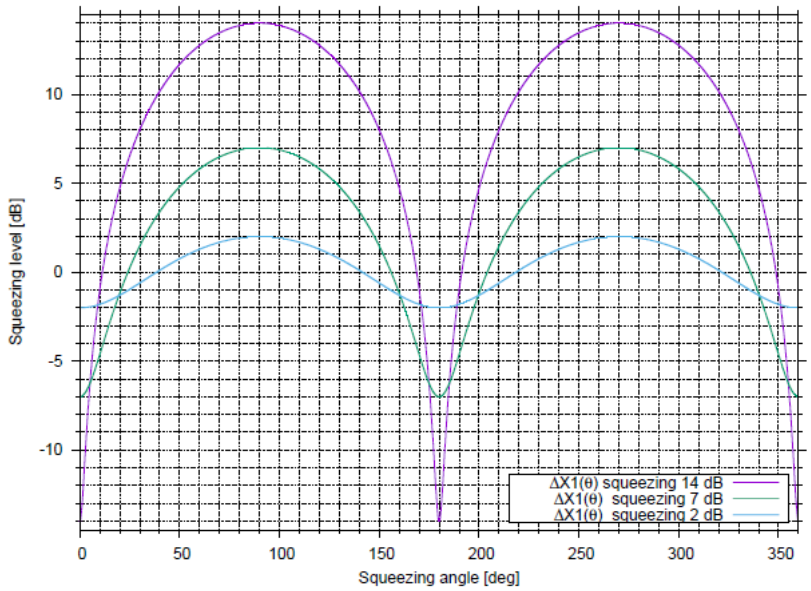

Figure 2.2: Quadrature noise variance as function of the quadrature angle θ. The violet line represents a squeezed state of 14dB, the green line is a squeezed state of 7dB and the blue line a squeezed state of 2dB [31].

Figure 2.2 shows the variance of the quadrature operator with respect to the variance of the coherent vacuum as a function of the quadrature angle for different values of the squeezing factor. The minimum and maximum value represent squeezing and anti-squeezing level respectively.

2.2 Squeezing detection

To properly detect squeezed states of light we need to obtain information about the quantum noise in different field quadratures. For this reason a single photodetector, able to detect only amplitude-quadrature, is not sufficient. A suitable device is a *balanced homodyne detector* [32], a device composed by two photodiodes (PDs) and a 50:50 BS. A conceptual scheme of an optical homodyne detector is shown in figure 2.3. The squeezed light beam, coming from the squeezing cavity, reaches the 50:50 BS where it interferes with a strong Local Oscillator (LO) field at the same frequency, same spatial mode and same polarization. Each output of the BS is detected by a photodiode. This technique exploits the interference phenomenon between the two input fields of the BS that are: the field under measurement, represented in the figure 2.3 with the operator $\hat{a}$ and a reference field, called local oscillator (LO), represented in the figure with the operator $\hat{b}$. The two output of the BS are respectively the reflected field, represented by the operator $\hat{c}$, and the transmitted field, represented by the operator $\hat{d}$. The BS input-output relation can be written as [31]

$$\begin{pmatrix} \hat{c} \\ \hat{d} \end{pmatrix} = \begin{pmatrix} r & t \\ t & -r \end{pmatrix} \begin{pmatrix} \hat{a} \\ \hat{b} \end{pmatrix} \tag{2.82}$$

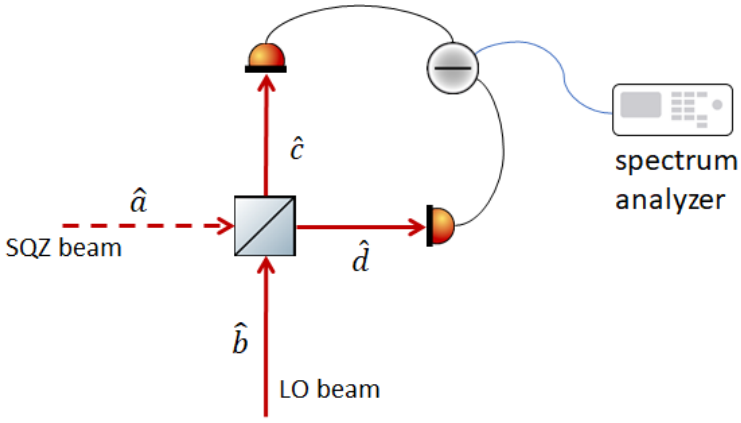

Figure 2.3: A balanced homodyne detector is essentially based on the interference between the squeezed vacuum beam (SQZ beam) and a strong local oscillator (LO) on a 50:50 beam splitter. The difference between the two generated photocurrents give us information about the squeezing level of the SQZ beam.[33]

where r and t are respectively its reflectance and transmittance. Since the squeezing detection is performed with the balance homodyne detector, the beam splitter has a 50/50 splitting ratio and the expressions of the currents can be simplified by inserting $r = t = 1/\sqrt{2}$. Moreover, if we assume that our system does not have losses, the signal (squeezed) field $\hat{a}$ and the LO field $\hat{b}$ can be linearized as

$$\hat{a} = \alpha + \delta\hat{a} \tag{2.83}$$

and

$$\hat{b} = (\beta + \delta\hat{b})e^{i\phi} \tag{2.84}$$

where ϕ is an arbitrary phase between the local oscillator field and the field under measurement, and can be controlled, for example, by a steering mirror mounted on a piezo-electric element, whereas α and β are real coefficients. At the output of the 50:50 BS we have the two fields:

$$\hat{c} = \frac{1}{\sqrt{2}}(\hat{a} + \hat{b}) \tag{2.85}$$

$$\hat{d} = \frac{1}{\sqrt{2}}(\hat{a} - \hat{b}). \tag{2.86}$$

The two BS outputs are detected by two different photodiodes, and the currents produced by the two photodiodes are proportional to the intensity of light that reaches the detectors, and then to the relative photon number. Considering that the two number operators associated to the two output beams are $\hat{c}^\dagger\hat{c}$ and $\hat{d}^\dagger\hat{d}$, we can calculate the two photocurrents, $\hat{i}_c$ and $\hat{i}_d$, detected at the two PDs. In particular we have

$$\hat{i}_c \propto \hat{c}^\dagger\hat{c} = \frac{1}{2}(\hat{a}^\dagger + \hat{b}^\dagger)(\hat{a} + \hat{b}) = \frac{1}{2}(\hat{a}^\dagger\hat{a} + \hat{a}^\dagger\hat{b} + \hat{b}^\dagger\hat{a} + \hat{b}^\dagger\hat{b}). \tag{2.87}$$

With some algebra [33] and neglecting the terms $O(\delta^2)$ it is possible to obtain the photocurrent generated by the the reflected field $\hat{c}$ as

$$\hat{i}_c = \frac{1}{2}\Big[\alpha^2 + \beta^2 + 2\alpha\beta\cos\phi + 2\alpha(\cos\phi\delta\hat{X}_b - \sin\phi\delta\hat{Y}_b + \delta\hat{X}_a) \tag{2.88}$$

$$+2\beta(\cos\phi\delta\hat{X}_a + \sin\phi\delta\hat{Y}_a + \delta\hat{X}_b)\Big] + O(\delta^2), \tag{2.89}$$

where

$$\delta\hat{X}_a = \frac{\delta\hat{a}^\dagger + \delta\hat{a}}{2} \qquad \delta\hat{Y}_a = i\frac{\delta\hat{a}^\dagger - \delta\hat{a}}{2} \tag{2.90}$$

$$\delta\hat{X}_b = \frac{\delta\hat{b}^\dagger + \delta\hat{b}}{2} \qquad \delta\hat{Y}_b = i\frac{\delta\hat{b}^\dagger - \delta\hat{b}}{2}. \tag{2.91}$$

In a similar way we obtain the photocurrent generated by the field $\hat{d}$

$$\hat{i}_d \propto \hat{d}^\dagger\hat{d} = \frac{1}{2}(\hat{a}^\dagger - \hat{b}^\dagger)(\hat{a} - \hat{b}) = \frac{1}{2}(\hat{a}^\dagger\hat{a} - \hat{a}^\dagger\hat{b} - \hat{b}^\dagger\hat{a} + \hat{b}^\dagger\hat{b}) \tag{2.92}$$

$$= \frac{1}{2}[\alpha^2 + \beta^2 - 2\alpha\beta\cos\phi - 2\alpha(\cos\phi\delta\hat{X}_b - \sin\phi\delta\hat{Y}_b - \delta\hat{X}_a) \tag{2.93}$$

$$- 2\beta(\cos\phi\delta\hat{X}_a + \sin\phi\delta\hat{Y}_a - \delta\hat{X}_b)] + O(\delta^2). \tag{2.94}$$

We have to consider that the two photodiodes are mounted on an electronic circuit that computes the sum ($\hat{i}_+$) and the difference ($\hat{i}_-$) of their output currents. Then if we consider that the LO is stronger than the squeezed beam

$$|\beta|^2 \gg |\alpha|^2 \tag{2.95}$$

and we compute the difference $\hat{i}_-$ between the two photocurrents generated by the output fields $\hat{c}$ and $\hat{d}$, we obtain

$$\hat{i}_- \propto \hat{i}_c - \hat{i}_d \propto \beta(\cos\phi\delta\hat{X}_a + \sin\phi\delta\hat{Y}_a) = \beta\left(\frac{e^{-i\phi}\hat{a} + e^{i\phi}\hat{a}^\dagger}{2}\right) \equiv \beta\delta\hat{X}_a^\phi. \tag{2.96}$$

This means that, the LO noise is completely suppressed and the uncertainty on the squeezed field quadrature $\hat{X}_a^\phi$ is amplified by the interference with the coherent LO. In order to obtain the information on the rotated quadrature, the power spectral density of the difference signal is acquired with a spectrum analyzer. The power spectrum of a stationary process is equal to the Fourier transform of its auto-correlation function (from Wiener Khinchin theorem [31]), so by measuring the difference signal with a spectrum analyzer, the information about an arbitrary quadrature uncertainty is extracted. The variance of the difference of the photocurrents, that can be measured, is proportional to the variance of the squeezed field quadrature, these to quantities scale as the intensity of the LO

$$V(\hat{i}_-) \propto V(\hat{X}_{sqz}^\phi), \tag{2.97}$$

the noise distribution can be measured by a spectrum analyzer. The degree of squeezing is expressed as reduction in variance with respect to that of a coherent vacuum state. The variance in dB is

$$V[dB] = -10\log_{10}\left(\frac{\left\langle\Delta^2\hat{X}_{sqz}\right\rangle}{\left\langle\Delta^2\hat{X}_{coh,vac}\right\rangle}\right), \tag{2.98}$$

then, assuming $\left\langle \Delta^2 \hat{X}_{coh,vac} \right\rangle = 1$ and considering that $\Delta^2 \hat{X} = e^{-2r}$ and $\Delta^2 \hat{Y} = e^{-2r}$, it gives

$$V[dB] = -10 \log_{10}(e^{-2r}), \tag{2.99}$$

from which we can obtain the squeezing factor

$$r = \frac{\ln 10^{\frac{V[dB]}{10}}}{2}. \tag{2.100}$$

As said above, the homodyne detection is performed by overlapping the signal and the local oscillator fields on a beam splitter. In a real experiment the interference phenomenon is not perfect. To obtain the maximum interference the two beams must have the same frequency, spatial modes, waist dimension, waist position and polarization. A mismatch of this quantities, between the two beams, causes a degradation of the interference phenomenon. The degradation of the interference between these two fields is quantified via the *fringe visibility*, that is measured by scanning the relative phase between them and measuring the intensity of the fringes with a photodetector. In particular the visibility is defined as

$$\mathcal{V} = \frac{V_{max} - V_{min}}{V_{max} + V_{min}} \tag{2.101}$$

where V_{max} and V_{min} are respectively the minimum and the maximum of the voltage on the two photodiodes. The mismatch is an optical loss in the squeezing measurement and it contributes quadratically to the detection efficiency that is equal to

$$\eta_{eff} = \eta_{prop} \eta_q \mathcal{V}^2, \tag{2.102}$$

where η_q is the quantum efficiency of the photodiode and η_{prop} are the losses due to propagation of the squeezing field from its generation to its detection.

2.3 Quantum noise in an interferometer

[31] In the present section, with the help of a quantum mechanical approach, it will be described how the Heisenberg uncertainty principle, which is at the origin of quantum noise, limits the sensitivity of advanced GW interferometric detectors (i.e a Michelson interferometer with Fabry-Perot arm cavities). Using these tools, we will describe how the standard quantum limit (SQL) can be overcome, and how the injection of squeezed vacuum in the dark port of the ITF can reduce the quantum noise. A simple scheme of a Michelson interferometer is shown in figure 2.4.

An ideal interferometer have identical arms, and it works locked on a dark fringe, so that fields entering from each port will return exactly to that port with opposite phase. The carrier light from the laser enters from the common (*bright*) port, goes through the 50:50 beam splitter (BS), is reflected by the two end mirrors and finally it recombines at the BS, while the differential port remains *dark*. The length of the two arms is identified with l and the displacement of the two test masses respect to their rest position is defined respectively with z_1 and z_2. The interference signal

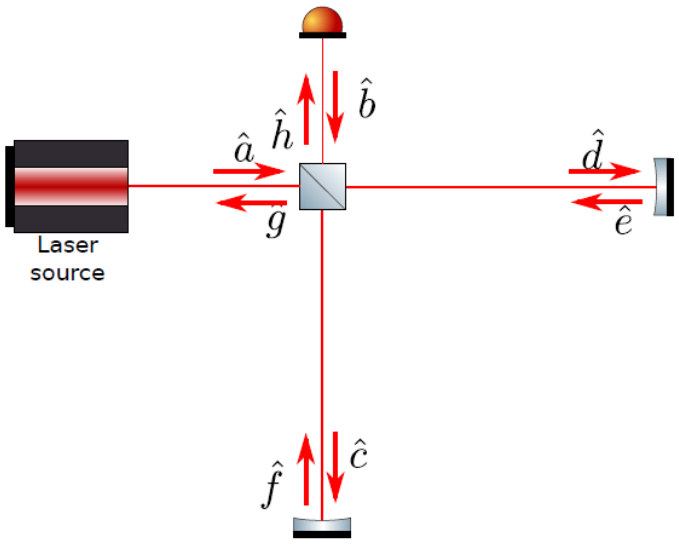

Figure 2.4: Scheme of the most simple configuration of a Michelson ITF, with a graphical representation of the quantum input and output fields.[31]

between the beams in the two arms is measured with a photodetector placed in front of the BS output dark port, and collects the information about the relative phase of the light in the two arms. When a GW passes through the interferometer plane, it induces a phase shift $\Delta\phi = 2kz$, where k is the wave vector. If we denote the mass of the two mirrors with m and the mass of the BS with M, it can be assumed that $m \ll M$ so that the BS is considered as at rest and the radiation pressure contribution acts only on the end mirror.

We can use the quantum mechanical formalism described in this chapter, to show how the precision of a measurement of z is limited by the Heisenberg uncertainity principle. In particular we will show that the two quantum mechanical noise sources are the fluctuations of the radiation pressure on the mirrors and the fluctuations of the number of photons at the BS output port [2]. Even if for a complete analysis they must be considered as a single contribution, they are separately analyzed in the next two sections and then the total error is obtained as the quadrature sum of these contributions.

2.3.1 Radiation pressure noise

In a Michelson interferometer, the contribution to the radiation pressure due to the light emitted by the laser is zero, but it is also possible to observe that its sensitivity at low frequency is limited by the radiation pressure noise. In 1980, Caves [2] first demonstrated that this contribution is due to the vacuum fluctuations of the field that enter in the interferometer from the unused BS port and interferes with the laser light. Their contribution is to transfer the momentum to the test masses m, that are assumed initially at rest. In order to find the perturbation of z due to radiation pressure, the transferred momentum is computed starting from the BS matrix defined in eq. 2.82. If the BS ratio is 50:50 the two output fields are defined

as in equations 2.85 Each photon, that reaches one of the two end mirrors, transfers to it a momentum equal to $|p| = 2\hbar\omega/c$. The difference between the momenta transferred to the end masses is proportional to the difference between the number of photons in the field $\hat{c}$ and $\hat{d}$, then the total transferred momentum is equal to

$$\mathcal{P} = \frac{2\hbar\omega}{c}(\hat{d}^\dagger\hat{d} - \hat{c}^\dagger\hat{c}) \tag{2.103}$$

which in term of the two input fields of the BS is

$$\mathcal{P} = \frac{2\hbar\omega}{c}(\hat{a}^\dagger\hat{b} - \hat{b}^\dagger\hat{a}). \tag{2.104}$$

In this analysis we assume that the incoming modes $\hat{a}$ and is a coherent state, while the mode $\hat{b}$ is treated as a squeezed vacuum state (since this leads to a more general result with respect to consider $\hat{b}$ as a simple vacuum state) [31]. The light mode in the interferometer is

$$|\psi\rangle = \hat{S}_b(\zeta)\hat{D}_a(\alpha)|0\rangle. \tag{2.105}$$

From the properties of coherent and squeezed states it follows that

$$\langle\psi|\mathcal{P}|\psi\rangle = 0. \tag{2.106}$$

and, if the quadrature of the squeezed state with reduced noise is in phase with respect to the coherent excitation of mode $\hat{a}$, we can write

$$\langle(\Delta\mathcal{P})^2\rangle_\psi = \left(\frac{2\hbar\omega}{c}\right)^2(\alpha^2e^{2r} + \sinh^2 r). \tag{2.107}$$

Therefore, in a measurement of duration τ, the fluctuation of the operator $\mathcal{P}$ due to the radiation pressure noise on the relative position of the test masses, $z = z_1 - z_2$ is given by [31]:

$$\Delta z|_{rp} = \frac{\sqrt{\langle(\Delta\mathcal{P})^2\rangle_\psi}}{2m}\tau = \frac{\hbar\omega\tau}{mc}\sqrt{\alpha^2e^{2r} + \sinh^2 r}. \tag{2.108}$$

This result describe the effect of the fluctuations of the vacuum field that enter the BS from the interfermeter output port and show how to suppress these fluctuations by replacing them with squeezed states [31]. By substituting $r = 0$ in eq. 2.108 the radiation pressure noise contribution is obtained. When $r \neq 0$, the term α^2e^{2r} represents the effect of the replacement of the vacuum state with a squeezed vacuum state: when the amplitude quadrature is squeezed the radiation pressure noise is canceled out, whereas if the phase quadrature is squeezed the radiation pressure fluctuations increase.

2.3.2 Shot noise

The other contribution is related to the photon counting error, due to the fluctuations of the number of photons that reach the photodetector, and is represented by a fluctuation in the number operator of the mode detected by the photodiode. As

for the radiation pressure, we have to express the output modes in terms of input modes. For doing this, we have to consider the effect of the propagation along the arms of the ITF, so that the two input fields are now the reflected beams by the end mirrors, and the two output fields can be written in term of the beam fields in its arms. Then, the relation between input and output operators is given by [34]

$$\begin{pmatrix} \hat{f} \\ \hat{e} \end{pmatrix} = e^{i\Phi} \begin{pmatrix} \cos(\Delta\phi/2) & i\sin(\Delta\phi/2) \\ i\sin(\Delta\phi/2) & \cos(\Delta\phi/2) \end{pmatrix} \begin{pmatrix} \hat{h} \\ \hat{g} \end{pmatrix} \tag{2.109}$$

where

$$\Delta\phi = \pi + 2\frac{\omega z}{c} \tag{2.110}$$

is the phase difference between the light from the two arms, with $z = z_1 - z_2$, and

$$\Phi = 2\frac{\omega}{c}(z_1 - z_2) + const. \tag{2.111}$$

is the average phase. When the two fields are detected with two different PDs, the difference of their photons number can be expressed as:

$$\hat{n} = [\hat{h}^\dagger\hat{h} - \hat{g}^\dagger\hat{g}] = [\hat{f}^\dagger\hat{f} - \hat{e}^\dagger\hat{e}]\cos(\Delta\phi) + i[\hat{f}^\dagger\hat{f} - \hat{e}^\dagger\hat{e}]\sin(\Delta\phi) \tag{2.112}$$

Then, given the field circulating inside the interferometer in eq. 2.105, the mean value and the variance of number operator of the output mode, $\hat{n}$, can be computed as [2]

$$\langle\hat{n}\rangle = [\alpha^2 - \sinh^2 r]\cos\Delta\Phi \tag{2.113}$$

and

$$\langle(\Delta\hat{n})^2\rangle = [\alpha^2 + 2\cosh^2 r\sinh^2 r]\cos^2\Delta\phi + [\alpha^2 e^{-2r} + \sinh^2 r]\sin^2\Delta\phi. \tag{2.114}$$

Therefore, we can see that a small variation of the relative position of the two test masses, δz, causes a small variation of the photon number, $\delta\hat{n}$, which is given by:

$$\delta\hat{n} \approx -\frac{2\omega}{c}\sin(\Delta\phi)\delta z, \tag{2.115}$$

obtained considering that $\alpha^2 \gg \sinh^2 r$ for the squeezed vacuum state injected in an GW interferometer. Thus, the effect of the photon number fluctuations can be rewritten as a fluctuation of the two mirrors relative position z:

$$\Delta z|_{sn} \approx \frac{c}{2\omega}\sqrt{\frac{\cot^2(\Delta\phi)}{\alpha^2} + \frac{2\cot^2(\Delta\phi)\cosh^2 r\sinh^2 r}{\alpha^4} + \frac{e^{-2r}}{\alpha^2} + \frac{\sinh^2 r}{\alpha^2}}. \tag{2.116}$$

Since $\Delta\phi$ depends on the relative position between the two photodiodes, its value is chosen such that $\cot\Delta\phi = 0$ and the previous equation becomes:

$$\Delta z|_{sn} \approx \frac{c}{2\omega\alpha^2}\sqrt{\alpha^2 e^{-2r} + \sinh^2 r}. \tag{2.117}$$

As in the radiation pressure case, if $r = 0$ is substituted in equation 2.114, it represents the effect of the fluctuations of a coherent vacuum state that enters in the

dark port of the interferometer. Moreover, for $r \neq 0$ the term $\alpha^2 e^{-2r}$ express the effect of the replacement of the vacuum state with a squeezed vacuum state. Then, if the amplitude quadrature is squeezed, the shot noise is enhanced, whereas if the phase quadrature is squeezed the shot noise is suppressed.

The total quantum noise on the measure of z is the quadrature sum of the two contributions [2]. Then, from equations 2.108 and 2.117 we can write

$$\Delta z|_{tot} = \sqrt{\Delta z|^2_{rp} + \Delta z|^2_{sn}} = \sqrt{\left(\frac{\hbar\omega\tau}{mc}\alpha e^r\right)^2 + \left(\frac{c}{2\omega}\frac{1}{\alpha e^r}\right)^2} \tag{2.118}$$

where is assumed that $\alpha^2 \gg \sinh^2 r$. With this quantum mechanical treatment it is understood why it is useful the injection of squeezed states in a GW interferometer. Indeed, the quantum noises, i.e. radiation pressure noise and shot noise, are induced by electromagnetic vacuum fluctuations that enter in the detector from its dark port. As we shown before, a first solution to limit shot noise is to increase the input power. But, a higher input power increases the radiation pressure noise that can become an important source of noise already for the advanced gravitational wave detectors. If a squeezed vacuum is injected into the dark port of an ITF, the power needed to reach the optimum sensitivity is reduced with respect to the case in which a coherent vacuum enters the ITF. Viceversa, with the same power of the laser it is possible to reduce one of the two contributions to the quantum noise by fixing the phase of the squeezed vacuum to the laser and choosing the appropriate squeezing angle. Then, the injection of squeezed vacuum allows GW interferometers to achieve a better sensitivity, without changing its input power.

2.4 Squeezing injection

In a suspended interferometer, the two uncertainties on phase and amplitude quadratures, ΔX and ΔY respectively, are related to the shot noise and the radiation pressure noise of the input vacuum field, as demonstrated in the previous sections. Since shot noise and radiation pressure noise together enforce the standard quantum limit (SQL) only if they are uncorrelated, in principle, by creating a correlation between phase and amplitude fluctuation, the SQL can be overcome [35]. This can be achieved in a Quantum Non Demolition (QND) interferometer, as proposed by Braginsky [36], that prevents its own quantum properties from demolishing the state of the system on which is performing the measurement. Since both types of quantum noise can be attributed to vacuum field fluctuations entering the interferometer from its antisymmetric port, injecting squeezed vacuum into this port can improve the sensitivity of the detector [2]. However, for different kinds of interferometers, the required squeezed vacuum may be very different [37]. As explained by Corbitt and Mavalvala [35], the Quantum Non Demolition (QND) interferometers can be realized in different ways

- the *injection of squeezed vacuum states* with the appropriate quadrature into the dark port can reduce the dominant optical noise. The squeeze angle de-

scribes the linear combination of input quadratures in which fluctuations are reduced, that translates into modifying the interferometer input fields;

- the *dynamical correlations*, in which the interferometer mirrors dynamics is modified. The radiation pressure force acts on the mirrors as a restoring force with a frequency dependent optical spring constant (i.e. *ponderomotive rigidity*), and the coupling between the optical field and the mechanical modes of the mirrors generates the dynamical correlation;

- the direct *measurement of a QND observable* which satisfies the commutation relations for the measurement probe;

- the *variational or frequency-dependent homodyne readout* technique applied on the output fields.

The Michelson interferometer operates in dark fringe condition to minimize the coupling of the technical laser noise to the antisymmetric (dark) port. Since most of the light returns towards the laser, a partially transmitting power-recycling mirror (PRM) is placed between the laser source and the beam splitter to recycle the light back into the interferometer [35]. The GW signal at a given frequency, due to asymmetric motion of the end mirrors, appears as a phase modulation on light. After mixing with a local oscillator field at the beam splitter, this phase modulation is converted into amplitude modulation that is detected by the photodetector, and the GW signal appears only in a single quadrature. As well as for a simple Michelson interferometer, in the power-recycled Michelson only the phase quadrature is detected. Therefore, the radiation pressure noise and the shot noise in these interferometers are uncorrelated. Vacuum fluctuations entering the antisymmetric port travel into each arm and return to the antisymmetric port without any important overall phase shift. Without injecting squeezing or a modified readout, there is no quantum non demolition at any operating power. Consequently, this configuration, called *conventional interferometer*, is a power-recycled interferometer with arm cavity half-linewidth of 100Hz and power input at the beam splitter that gives the standard quantum limit performance at 100Hz. Furthermore, as demonstrated by Corbitt [35], with a power-recycled interferometer, it is possible to create a dynamical correlation between the shot noise and radiation pressure noise, and the additional input (squeezing) and output (readout) methods can be used to fully exploit these correlations.

2.5 Squeezed light generation

Squeezed states of light can be generated in different ways. At present the most successful way, already adopted in the Advanced detectors in their third observation run (O3), is to use nonlinear crystals. It is interesting to note that for $\theta \sim 3\pi/4$ the correlations induced by squeezed light allows to break down the standard quantum limit by a factor $exp(-2\xi)$ [38]. However, a constant value of θ cannot produce a reduction of the quantum noise power spectral density over the whole observation

band. In order to reduce simultaneously both quantum noise components, a frequency dependent squeezing angle is required. This can be done by using a more complex squeezing source, obtained by reflecting the squeezed vacuum off a detuned Fabry-Perot cavity, known as *filter cavity*, as first demonstrated in 2020 in a suspended 300 meter long filter cavity by [10], able to induce a rotation of the squeezing ellipse below 100 Hz. This last approach for a frequency dependent squeezing (FDS) requires an additional long base-line, low-loss filter cavity in a vacuum system at the detector's site. As an innovative solution, in [12] it is shown that such a filter cavity is not needed, if EPR-entangled signal and idler beams are exploited for the generation of FDS. In the following, this different technique for both frequency independent and frequency dependent squeezing are discussed with more detail.

2.5.1 Squeezing vacuum source: OPO process

The squeezing vacuum source is characterized by a squeezing ellipse rotation angle θ constant over the whole frequency band. This method is based on the degenerate parametric down-conversion process inside a nonlinear optical device. These processes are nonlinear in the sense that the response of a system, such as nonlinear crystals, subjected to an external optical field depends in a nonlinear way on the amplitude of the applied field. Considering a nonlinear medium with no losses or dispersion, we can write the polarization vector, $\mathcal{P}$, which is the dipole moment per unit volume, as a response to an incident electrical field $E(t)$. In particular, for a second order nonlinear process, we can write $\mathcal{P}$ as [39]

$$\mathcal{P} = \epsilon_0 \chi^{(2)} E^2(t), \tag{2.119}$$

where ϵ_0 is the permittivity of the vacuum and $\chi^{(2)}$ is the second-order nonlinear optic susceptibility, which is assumed to be independent from the frequency of input field. Moreover, we can find the wave equation in a nonlinear optical medium as

$$\nabla^2 E - \frac{n^2}{c^2}\frac{\partial^2 E}{\partial t^2} = \frac{1}{\epsilon_0 c^2}\frac{\partial^2 \mathcal{P}^{NL}}{\partial t^2} \tag{2.120}$$

where n is the refractive index and is $n = \sqrt{\epsilon^{(1)}}$. The term $\partial^2 \mathcal{P}^{NL}/\partial t^2$ is a measure of the acceleration of the charges of the medium that, for the Larmor theorem, generates electromagnetic waves: it represents the non linear response of the medium. This equation is important because it tells us that the nonlinear response of a crystal to the radiation acts as a source term. In the linear case, the term $\mathcal{P}^{NL}$ becomes zero, and we have the classic equation of waves in a medium with refractive index n. In case of a polarization $\mathcal{P}^{(2)}$, instead, the answer of the non-linear crystal to a laser beam with frequency ω is the radiation of a beam at frequency 2ω. In this way it is possible to obtain an output laser beam. In particular, for an electric field with two frequency components, written as

$$E(t) = E_1 e^{-i\omega_1 t} + E_1^* e^{i\omega_1 t} + E_2 e^{-i\omega_2 t} + E_2^* e^{i\omega_2 t}, \tag{2.121}$$

the second-order nonlinear polarization vector is given by

$$\begin{aligned}\mathcal{P}^{(2)} &= 2\epsilon_0\chi^{(2)}[E_1E_1^* + E_2E_2^*] \\ &+ \epsilon_0\chi^{(2)}\left[E_1^2e^{-i2\omega_1 t} + E_1^{*2}e^{i2\omega_1 t}\right] \\ &+ \epsilon_0\chi^{(2)}\left[E_2^2e^{-i2\omega_2 t} + E_2^{*2}e^{-i2\omega_2 t}\right] \\ &+ 2\epsilon_0\chi^{(2)}[E_1E_2e^{-i(\omega_1+\omega_2)t} + E_1^*E_2^*e^{i(\omega_1+\omega_2)t}] \\ &+ 2\epsilon_0\chi^{(2)}[E_1^*E_2e^{-i(\omega_1-\omega_2)t} + E_1^*E_2e^{i(\omega_1-\omega_2)t}].\end{aligned} \tag{2.122}$$

The term in each line of this equation describes how the interaction of an electromagnetic field with a nonlinear crystal produces different physical process allowed by the energy conservation law: the first one represent a zero-frequency contribution, called optical rectification (OR), the second one is the second harmonic generation (SHG) term, the third line is the sum frequency generation (SFG) term, and the last term is the difference frequency generation (DFG). Therefore each second order nonlinear process should generate four components at difference frequency. However, in order to have a non negligible intensity of the output beam, phase-matching condition of the input and output beams must be ensured [39]. Furthermore, to select desired frequency, the polarization of the input radiation and the orientation of the nonlinear crystal must be suitably chosen. In particular, in an *up-conversion process*, photons at higher frequency are obtained starting from photons at lower frequency. This is the case of the SHG process, illustrated in figure 2.5, which is a particular SFG process, where the two input fields oscillate at the same fundamental frequency ω and the generated field oscillates at frequency 2ω. Moreover, the nonlinear crystal is placed in an optical resonator, resonant on the fundamental beam, in order to improve the conversion efficiency. The SHG process is used in

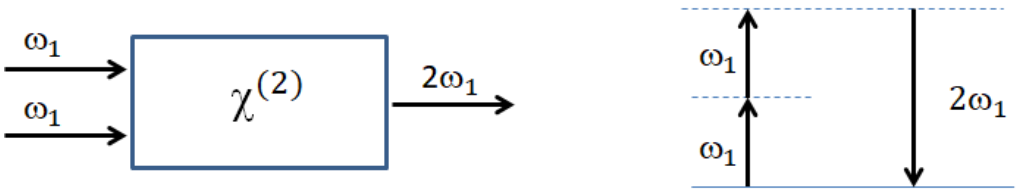

Figure 2.5: Representation of the SHG (left) and relative energy-level diagram (right). Photons at a fundamental frequency ω combine to produce photons at frequency 2ω.

the squeezing experiment in Virgo to obtain the green pump beam for the squeezing cavity [33]. To have a deeper picture of how these frequency components are generated let us refer to [39].
The reverse process is called down-conversion process and it is the method already employed to produce the squeezed vacuum states used as an improvement of gravitational wave detector sensitivity for the third observational run. In the parametric down-conversion process, the incident photons at higher frequency interact with a lossless nonlinear optical medium to produce an output wave at the difference frequency $\omega_3 = \omega_1 - \omega_2$. The incoming beam is called *pump*. Hence, two beams, a pump beam and a bright seed beam, hit on a nonlinear crystal, causing the field at frequency ω_2 to be amplified by this process that is also known as *optical parametric amplification* (OPA). This process is illustrated in figure 2.6.

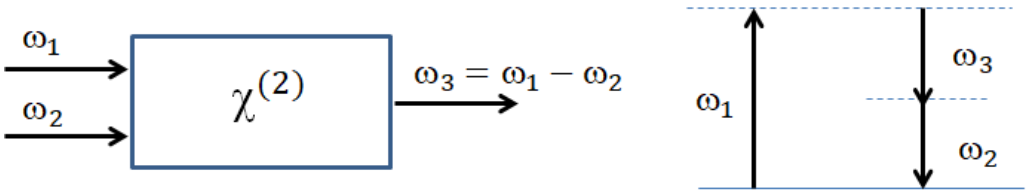

Figure 2.6: Difference frequency generation (DFG): geometry of the interaction (left) and relative energy-level diagram (right).

2.5.1.1 Optical Parametric Oscillator

An important point to remark is that the process of DFG leads to the amplification of the lower-frequency input field, that is the OPA process, where the nonlinear crystal is seeded by a bright beam and *bright squeezed states* are generated. Differently, when the seed is constituted by the vacuum fluctuations, *squeezed vacuum states* are produced. Now, the gain resulting from this process can be used to construct a device known as an optical parametric oscillator (OPO) [33]. The fluctuations which characterize the vacuum state consist into creation and annihilation of virtual photon-pairs at all frequencies and all spatial modes. This means that the frequency of the vacuum seed, that induces the down-conversion of the pump photon, constantly changes. Due to the random frequency separation between the pump beam and the vacuum seed, the produced photon-pair has a frequency separation from the carrier beam that also changes. This process leads to the coupling between the quantum noise of the two field quadratures, thus it can be used to generates squeezed states of light. The produced squeezed states have reduced noise in a certain quadrature, depending on the phase of the pump beam [40]. Figure 2.7 gives a schematic picture of this process. In an optical parametric oscillator conventionally

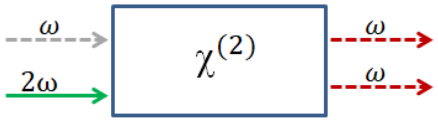

Figure 2.7: Representation of OPA process with an optical parametric oscillator (OPO).

the $\omega_1 = 2\omega$ field is called *pump* ω_p, the amplified field $\omega_2 = \omega$ is called *signal* ω_s and the difference frequency field $\omega_3 = \omega$ is called *idler* ω_i. In generating the difference frequency $\omega_i = \omega_p - \omega_s$, the lower-frequency input wave ω_s is amplified. The condition of energy conservation $\omega_s + \omega_i = \omega_p$ allows any frequency ω_s smaller than ω_p to be generated by an OPO. The output frequency ω_s can be controlled through the phase-matching condition $\Delta k = 0$, which invariably can be satisfied for at most one pair of frequencies ω_s and ω_i. The output frequency bandwidth can often be narrowed by placing wavelength-selective device (such as etalons) inside the OPO cavity. Without going into detail, from the second quantization formalism, considering the creation and annihilation of virtual photon-pairs at all frequencies and spatial modes, it is possible to find the wave equations as in [33], which in the

perfect phase matching condition can be written in term of quadrature operators

$$\frac{d\hat{X}}{dz} = -\gamma\hat{X} \Rightarrow \hat{X}(z) = \hat{X}(0)e^{-\gamma z} \tag{2.123}$$

$$\frac{d\hat{Y}}{dz} = \gamma\hat{Y} \Rightarrow \hat{Y}(z) = \hat{Y}(0)e^{\gamma z} \tag{2.124}$$

with $\gamma = gA_0$. Here, A_0 is a real number which represents the amplitude of the pump field, while g is the *amplitude gain coefficient* [33]. Equation 2.123 tells us that the quadrature with $\theta = 0$, $\hat{X}$, is exponentially de-amplified, whereas the quadrature with $\theta = \pi/2$, $\hat{Y}$, undergoes an exponential amplification. This result shows that the non linear process amplifies one of the two quadrature whereas the other is suppressed by the same factor. This means that the photon-pairs, that populate all frequencies, reduce quantum noise of the output field and then, they are source of squeezing. In this way, a degenerate optical parametric oscillator can be used for the squeezed light generation. In [6] the effects of squeezing vacuum field injection during the third observation run showed a quantum noise reduction in the phase quadrature of about 10 dB. As discussed in [40] the values of the squeezing and anti-squeezing measured take into account the degradation due to the optical losses and the residual quadrature fluctuations. Then, in the case of Advanced Virgo, the consequent shot noise reduction was of about 3.2 ± 0.1 dB. Instead, if the phase of the squeezed field is rotated by 90 degrees, the shot noise level increase of (8.5 ± 0.1) dB, that is the anti-squeezing level. The injection of frequency-independent squeezed vacuum states in Advanced Virgo allowed to achieve an improvement of $16\% - 28\%$ of detection rate for binary neutron stars [40].

2.5.2 Filter cavity

The phase-squeezed vacuum source used for the observation run O3 of advanced detectors could not reduce simultaneously both quantum noise components. Nevertheless, since radiation pressure noise is due to the amplitude fluctuations of the coherent vacuum, it can be reduced using amplitude-squeezed vacuum states. Indeed, a possible solution to reduce quantum noise in the whole detection band is the injection of frequency-dependent squeezed vacuum, where starting from phase-squeezed states, used for shot noise reduction, we can rotate the squeezing angle, which means rotating the squeezing ellipse, as a function of the frequency [40]. This technique has been demonstrated for the first time in [10], where it has been obtained a rotation of the squeeze ellipse at a frequency of about 90Hz. A similar experiment was carried out in the US for Advanced LIGO, where, using a 16 meters filter cavity they observed a squeezed quadrature rotation at a frequency of 30 Hz [11]. For this reasons, in the next observation run O4, this technique will be adopted as a solution to reduce quantum noise for the improvement of sensitivity of advanced GW detectors (both Virgo and LIGO). The experimental setup is composed by a source of frequency-independent squeezed vacuum, (for Advanced Virgo is the same OPO cavity used for O3) and a suspended detuned *filter cavity*, whose dispersion properties allow to have a rotation of the squeezing angle at a characteristic frequency, which corresponds to the minimum quantum noise achievable, depending

on the interferometer configuration [40]. The FIS beam generated by the OPO squeezer is injected inside the detuned filter cavity, which resonates at a frequency $\omega_{fc} = \omega_0 + \Delta\omega_{fc}$. Then, the reflected FIS field acquires a frequency dependent phase shift and the filter cavity induces a rotation of the squeezing angle θ_{fc}, at frequency Ω, given by [40]

$$\theta_{fc}(\Omega) = \arctan \frac{2\gamma_{fc}\Delta\omega_{fc}}{\gamma_{fc}^2 - \Delta\omega_{fc}^2 - \Omega^2} \tag{2.125}$$

where, γ_{fc} is the linewidth of the filter cavity, while $\Delta\omega_{fc}$ is the cavity detuning. The vacuum fluctuations which enter the interferometer output port interact with the suspended test masses. The input-output relation, obtained from a two-photons quantum formalism [41, 42], describes this opto-mechanical coupling and gives the condition to obtain the requirements for the detuning γ_{fc} for the filter cavity and on the spectral characteristics of the filter cavity mirrors. In the case of Advanced Virgo Plus (AdV+), the cavity linewidth must be of the order of few tens of Hertz [40]. In order to have a squeezing angle rotation at these frequencies, the filter cavity needs to be several hundred meters long. In particular, Virgo will use a 285 m long filter cavity, with a rotation angle at a frequency of $\sim 20 - 30$ Hz, for the next observational run O4. A description of the conceptual design can be found in [40]. The goal in Advanced Virgo Plus is to obtain $7 - 8$ dB of shot noise reduction without spoil the sensitivity at low frequency [40].

2.5.3 EPR squeezing

Squeezing based on the Einstein-Podolsky-Rosen (EPR) quantum entanglement [43], or EPR squeezing, is a novel strategy to achieve frequency-dependent squeezing for broadband quantum noise reduction, with the generation of EPR entangled squeezed beams and the use of the GW interferometer itself as the filter cavity, avoiding the need for external linear cavity.

In the Heisenberg approach of quantum mechanics, a sufficient criterion for occurence of entanglement is that correlations between conjugate observables of two sub-systems allow the statistical inference of either observable in one sub-system, upon a measurement in the other, to be smaller than the standard quantum limit, that is the presence of non-classical correlations [44]. This approach was originally proposed by Einstein, Podolsky and Rosen in 1935 [43] and, since then, it has been named the EPR paradox. Over the past years, entanglement has been studied in both discrete and continuous variable regimes [45, 46]. In particular, the most studied and generated form of entanglement in continuous variable quantum optics is indeed the Einstein-Podolsky-Rosen (EPR) entanglement [43]. A first experimental demonstration of the EPR paradox for a system of dynamical variables with a continuous spectrum was first proposed in [46]. This work follows the demonstration of the EPR paradox as quantified by Reid and Drummond [45]. The difference from the previous work with discrete variables, is that the continuous optical amplitudes of a *signal* beam are inferred in turn from those of a spatially separated but strongly correlated *idler* beam generated by non-degenerate parametric amplification in an optical parametric oscillator. The continuous variable EPR entanglement is thus

characterised by quantum correlations between conjugate quadrature amplitudes of two light beams, which can be the amplitude and the phase quadratures, thus called *quadrature entanglement* [44].

Following the approach used so far for the entanglement experiments mentioned before, Ma et al. [12] proposed for the first time in 2017 the realization of an optical setup for quantum noise suppression in GW interferometer by exploiting the EPR entanglement. The idea is to produce EPR entangled light beams by detuning an Optical Parametric Amplificator (OPA) and inject these beams into the intererometer through its dark port. The optical configuration is shown in figure 2.8. The

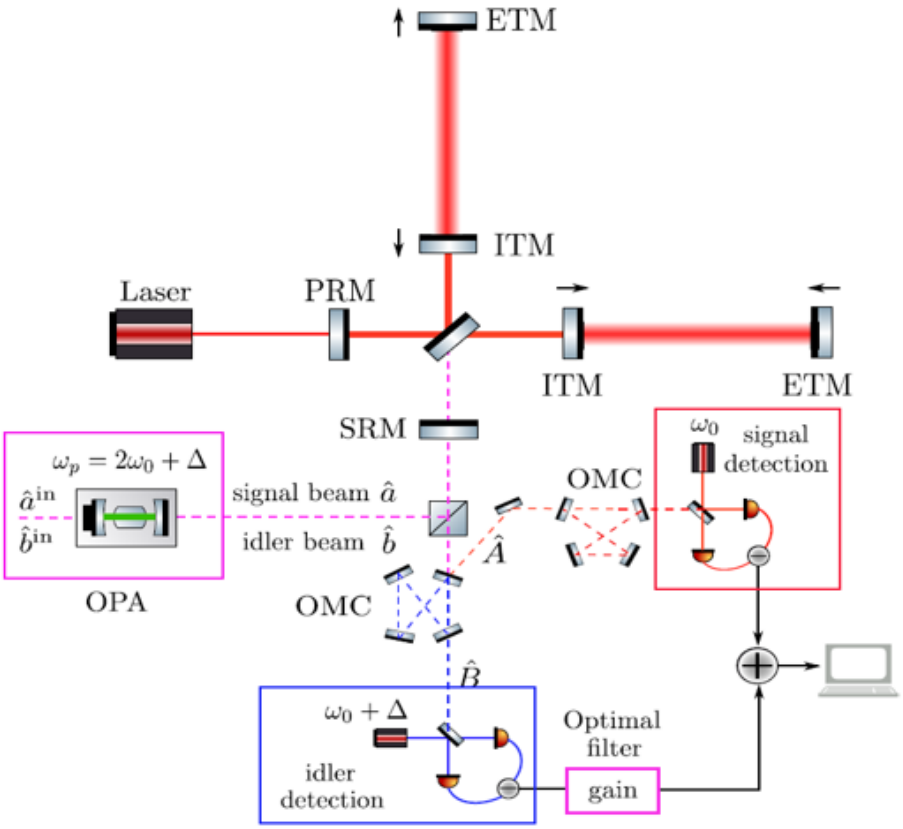

Figure 2.8: Optical configuration for noise suppression via EPR entanglement, for an ITF configuration with a power recycling mirror (PRM), and signal recycling mirror (SRM) [12].

strategy proposed here is explained in the following. The pumping frequency of an OPO cavity is detuned as $\omega_p = 2\omega_0 + \Delta$ (with ω_0 being the carrier frequency of the interferometer). For an OPA pumped at ω_p, they studied the quadrature fields around $\omega_p/2$, which are linear combinations of upper and lower sideband fields at $\omega_p/2 \pm \Omega$. Then, the optical nonlinearity inside OPA generate the entanglement between the upper and lower sidebands, $\omega_p/2 \pm \Omega$. In general, any pair of sideband fields with frequencies ω_1 and ω_1 within the squeeze bandwidth (usually >MHz) from $\omega_p/2$, and satisfying $\omega_1 + \omega_2 = \omega_p$, are entangled; in particular, for the proposed OPA two entangled beams are created, the *signal* beam with a frequency around the carrier, ω_0, and the *idler* beam around $\omega_0 + \Delta$. This entanglement is equivalent

to an EPR-type entanglement [47] between quadratures around ω_0. Then, the two produced beams are both injected into the ITF from its dark port and, since the idler beam is detuned from the carrier, the ITF will act as a filter cavity for this beam, causing a frequency-dependent quadrature rotation, which can be optimised by adjusting Δ with respect to the length of ITF cavities. Inside the ITF, the two beams are then separated and, after beating with local oscillators at frequencies ω_0 for the carrier and $\omega_0 + \Delta$ for the idler, are detected at two different homodyne detectors (see section 2.2). In this way, a fixed quadrature of the out-going idler beam is measured at the homodyne detector, and then the input signal beam will be conditionally squeezed by this measurement, in a frequency dependent way. Moreover, as suggested in [38], if we subtract the idler output, which contains only noise, from the signal output, which contains the gravitational signal plus noise correlated to the idler channel, we have a process in which the squeezing angle coincides with that of the idler's homodyne detector. This strategy allows to achieve the broadband reduction of quantum noise. In particular, with the strategy, proposed in [12], $\sim 11 - 12$ dB of sensitivity improvement are expected over the entire frequency band. This technique has also some disadvantage: first, it requires two squeezed beam instead of a single one (named as signal and idler) and, second, it is possible to demonstrate that the use of this technique leads to an intrinsic loss of 3 dB in the squeezing level [12], with respect to the filter cavity set up. Nevertheless, the advantages of EPR squeezing are greater then its limits. Indeed, an EPR squeezing setup can be hosted on smaller benches, thus avoiding the use of the long-scale filter cavity, which instead requires a huge infrastructure for hosting its setup. Another advantage of EPR setup concerns optical losses: while in a filter cavity the optical losses scales as 1 ppm/m, which means that the longer is the filter cavity, the higher are the losses, an EPR more compact setup allows to avoids this optical losses. Moreover, EPR setup requires a number of optical interfaces much smaller with respect to the filter cavity system, i.e. OPO-ITF versus OPO-FC plus FC-ITF, thus allowing a lower loss of mode mismatching. An R&D program is ongoing at the EGO laboratories in Cascina to demonstrate this method. At present, this technique has never been experimentally demonstrated into a Fabry-Perot ITF: such demonstration is one of the important goal of the experiment SIPS, discussed in this thesis (see section 3.3 for the discussion on the integration between the two setups).

2.5.4 Ponderomotive squeezing

An alternative method for frequency-dependent squeezing production is the generation of squeezed vacuum states via the *ponderomotive technique*, which exploits the effect of the radiation pressure on a suspended mirror. In fact, whenever a carrier light with sidebands reflects off a suspended mirror, the reflection ponderomotive-squeezes the light's sidebands, creating correlations between their radiation pressure noise in one quadrature and shot noise in the other [48]. These correlations were firstly presented implicitly by Braginsky in his earlier identification of the phenomenon of ponderomotive squeezing [49]. Then, with conceptually simple modifications of the interferometer input and/or output optics, it is possible to measure this correlation and to realize in this way a QND device [35]. The generation of

squeezed vacuum states via *ponderomotive technique* is one of the main goal of the experiment described in this thesis, for this reason it will be described in more details in the next chapter.

Chapter 3

SIPS experiment

The main goal of the work of this thesis is to study the realization of an optimal control system and finalize a table-top setup able to generate ponderomotive squeezed (PS) light in a radiation pressure noise-limited interferometer with suspended mirrors, in order to have the proper pendulum resonance below the GW detectors frequency band. With this squeezing technique, the effect of radiation pressure in opto-mechanical cavities can be exploited to generate a quantum correlation between phase and amplitude fluctuations which translates into a correlation between shot noise and radiation pressure noise [50, 51]. The idea of a suspended interferometer working in radiation pressure regime has been studied in [35] and [52]. In [52] it is demonstrated that such kind of interferometer design is, in principle, able to observe the radiation pressure noise, if some fundamental requirements are considered in the suspension design to keep the suspension thermal noise well below the level of the radiation pressure noise of the system. Furthermore, the realization of an opto-mechanical quantum-correlated system, such as the optical spring, has been demonstrated in the past years with small membrane resonators in the MHz region [53] and more recently (2020) [54] at lower frequencies.

In [37], Corbitt et al. proposed an experiment to extract ponderomotive squeezing from an interferometer with high circulating power and low mass mirrors, suspended as pendulums, in order to enhance the radiation pressure forces. Moreover, they proposed the use of detuned Fabry-Perot arm cavities: the change in the optical resonance induces an optomechanical rigidity, or *optical spring*, which suppresses the displacement noise linked to radiation pressure. The optomechanical dynamics induced by radiation pressure in a suspended Favry-Perot cavity has been measured by Corbitt et al in 2006 [55]. Nevertheless, this effect has never been observed in a Michelson ITF with Fabry-Perot cavities working in the same frequency range of GW detectors. This effect has an important role in the realization of a quantum non demolition (QND) ITF, for the reduction of quantum noise in the next generation of GW detectors, and for this reason we are actively working in the realization of a small scale interferometer which aims to exploit the optical spring effect to generate ponderomotive squeezing. Even if this is an extremely promising idea, a deep preliminary study and systematics R&D experimental work should be done to overcome all the possible factors which can prevent from the observation of the

ponderomotive effect.
The main limiting causes are listed in the following: (i) the weakness of the radiation pressure force exerted on the suspended mirrors and, in particular, of its quantum fluctuations with respect to the inertia of these macroscopic masses; (ii) the fluctuations of the laser frequency; (iii) the several "technical" noise sources dominating in the low frequency range, such as seismic noise, thermal fluctuation, Brownian noise, photo-thermal and thermoelastic noises; (iv) the dynamic instabilities originating in a highly non-linear system like an optical cavity, in presence of intense radiation forces, which can be due to both radiation pressure itself and to photo-thermal effects.

Considering that the present technology ensures the possibility to efficiently filter out seismic noise with the use of a superattenuator (see sec. 1.3.5 and fig. 1.10) [56, 24], it has been possible to design a macroscopic opto-mechanical cavity, with suspended mirror, dominated by the quantum radiation pressure noise. Based on the statement discussed in [37, 55], a first detailed analysis done in [57] shows that this can be achieved with a mirror suspension system tailored in such a way to keep the thermal noise associated to the suspensions and coatings low enough to observe radiation pressure fluctuations, by making an adequate choice of mirror suspension and coating parameters. In order to observe the effect of a temporal correlation between fluctuations of the radiation force and of the position of the resonator, in the audio frequency band, we need a mass of a few grams scale weight suspended as a pendulum in the two Fabry-Perot arms of a Michelson interferometer. With this choice, it is possible to cancel out the frequency noises common to the two FP cavities. The proposal to combine the two optical cavities modeled [57], to obtain a table-top radiation pressure-limited ITF, is the starting point of the research work discussed in this thesis, including both experimental work and theoretical study. Here, the ponderomotive squeezing will be generated by exploiting the optical spring effect in the Fabry-Perot cavities of the interferometer, which are properly detuned, according to the requirements derived and described in the next sections. In particular, SIPS experiment aims at generating tunable ponderomotive squeezing in a frequency range below 2 kHz.

3.1 Optical spring effect in a detuned cavity

The proposal to take advantage of the optical spring effect to obtain ponderomotive squeezed light from a detuned optical cavity was first made by [37]. Later, the use of an optical cavity with suspended mirrors of different low-masses has been studied in order to find the optimal configuration which allows to keep thermal noise low enough to observe the radiation pressure effect in the frequency range between 10 Hz and 10 kHz [57]. In a Fabry-Perot cavity the optical spring effect occurs when the optical restoring force (*optical rigidity*) on the cavity mirrors is comparable to, or greater than, the mechanical restoring force (*mechanical rigidity*), thus producing a phase shift of the cavity resonant frequency [55].
Let us consider a Fabry-Perot linear cavity composed by a suspended and perfectly reflective end mirror with mass m and a fixed and high reflective input mirror with

mass M [57]. The laser beam is characterized by a frequency ω_0 and an input power I_0. Assuming that the cavity is tuned close to its resonant frequency ω_r, the power circulating inside the cavity is

$$W(I_0, \delta_\gamma) = I_0 G \frac{1}{1+\delta_\gamma^2} \tag{3.1}$$

where

$$G = \frac{2\mathcal{F}}{\pi}, \tag{3.2}$$

is the gain of the optical cavity and

$$\delta_\gamma \equiv \frac{\delta\omega}{\gamma} = \frac{\omega_r - \omega_0}{\gamma} \tag{3.3}$$

is the ratio between the frequency shift with respect to the resonance and the cavity *pole*, or *half width at half maximum*, defined as

$$\gamma = \frac{c}{2L}\frac{(1-\rho_1\rho_2)}{\pi\sqrt{\rho_1\rho_2}}, \tag{3.4}$$

where L is the round-trip length, ρ_1 and ρ_2 are the reflection coefficient of input and end mirror and [13].

$$\mathcal{F} = \frac{\Delta\nu_{\mathrm{FSR}}}{\gamma} = \frac{\pi\sqrt{\rho_1\rho_2}}{1-\rho_1\rho_2} \tag{3.5}$$

is the *finesse* of the Fabry-Pérot cavity. In the case we are analyzing, being ρ_1 close to one, we can write $\tau_1^2 = 1-\rho_1^2 = (1-\rho_1)(1+\rho_1) \simeq 2(1-\rho_1)$, where τ_1^2 is the input mirror transmission coefficient. Moreover, since we are considering a perfectly reflective end mirror, which means $\rho_2 = 1$, the *finesse* can be rewritten as

$$\mathcal{F} = \frac{\pi}{1-\rho_1} = \frac{\pi}{2}\frac{\tau_1^2}{(1-\rho_1)^2}, \tag{3.6}$$

and the gain of the cavity becomes

$$G = \frac{\tau_1^2}{(1-\rho_1)^2}. \tag{3.7}$$

The linewidth can be also written as [37]:

$$\gamma = \frac{c}{2L}\frac{(1-\rho_1)}{\pi} = \frac{cT_{\mathrm{in}}}{4\pi L}, \tag{3.8}$$

being $T_{\mathrm{in}} = \tau_1^2$. Then, the detuning parameter δ_γ becomes

$$\delta_\gamma \equiv \frac{\delta\omega}{\gamma} = \frac{4\pi L(\omega_r - \omega_0)}{cT_{\mathrm{in}}}. \tag{3.9}$$

In this opto-mechanical system, the radiation pressure force, or *ponderomotive force*, acting on the end mirror is proportional to the power circulating inside the cavity

$$F_p = \frac{2W}{c}. \tag{3.10}$$

For a defined detuning parameter δ_γ, the ponderomotive force is balanced by the gravitational force acting as a restoring force on the end mirror and keeping the mirror in a mechanical equilibrium, such as a classical pendulum [37]. If we consider a displacement dx of the end mirror, the detuning parameter will also change, causing an additional restoring force acting on the mirror. The total restoring force, due to this displacement will be [37]

$$dF_x = -m\omega_p^2 dx + \frac{2}{c}\frac{\partial W}{\partial \delta_\gamma}\frac{d\delta_\gamma}{dx}dx = -(m\omega_p^2 + k_{\text{opt}})dx, \tag{3.11}$$

where ω_p is the pendulum frequency, and k_{opt} is the optical rigidity, or spring constant, due to the radiation pressure force. Equation 3.11 is also valid in the *quasi-static* regime, in which the cavity linewidth γ is much larger than the frequency ω_r [37]. Then, considering that $\omega_r = \pi c/L$ [57], we can write

$$\frac{d\delta_\gamma}{dx} = -\frac{4\omega_0}{cT_{\text{in}}}, \tag{3.12}$$

and the optical spring constant can be derived

$$k_{\text{opt}} = \frac{2}{c}\frac{\partial W}{\partial \delta_\gamma}\frac{d\delta_\gamma}{dx} = -\frac{4\omega_0 W}{\gamma L c}\frac{\delta_\gamma}{1+\delta_\gamma^2}. \tag{3.13}$$

Then, the equation of motion of the end mirror can be written in the form [57]

$$-m\omega^2 x = -(m\omega_p^2 + k_{\text{opt}})x + \frac{2}{c}\frac{\partial W}{\partial I_0}\overline{I}_0 x + F_{\text{ext}}, \tag{3.14}$$

where also the force due to the input power fluctuation, $\overline{I}_0$, and external force F_{ext} are considered. In the two-photon formalism, where the input and output field are written in terms of quantum amplitude and phase fluctuations, $a_{A,P}$, we define the characteristic optical spring frequency as [37]:

$$\Theta^2 \equiv \frac{k_{\text{opt}}}{m} = -\frac{4\omega_0 W}{\gamma m L c}\frac{\delta_\gamma}{1+\delta_\gamma^2} = -\frac{4\omega_0 I_0 \delta_\gamma}{mc^2}\left(\frac{4}{T_{\text{in}}}\frac{1}{1+\delta_\gamma^2}\right)^2. \tag{3.15}$$

Note that Θ can either be real, when $\delta_\gamma < 0$, or purely imaginary when $\delta_\gamma > 0$. On the other hand, the power fluctuation of the light incident on the cavity induces a fluctuating force on the mirror, as expressed in eq. 3.14 Then it is possible to express equation 3.14 in the two-photon formalism, as [37]

$$m(\Theta^2 + \omega_p^2 - \omega^2)x = \left(\frac{4}{T_{\text{in}}}\frac{1}{1+\delta_\gamma^2}\right)\frac{2\hbar\omega_0 A}{c}a_A + F_{\text{ext}}, \tag{3.16}$$

where A is the mean amplitude of the input field in the two photon formalism [37]. This equation shows that, if we are in the quasi-static regime, the mirror's (complex) mechanical resonant frequency is shifted from $\pm\omega_p$ to $\pm\sqrt{\omega_p^2 + \Theta^2}$. Supposing also that $\omega_p \ll |\Theta|$, then $\pm|\Theta|$ gives the mirror mechanical resonant frequencies, which correspond to a resonance when Θ is real, or to a pure instability when it is purely

imaginary. Assuming no external forces acting on the mirrors, we can define the the frequency-domain input-output relation as

$$\begin{pmatrix} b_A \\ b_P \end{pmatrix} = \begin{pmatrix} 1 & 0 \\ -2\mathcal{K}(\omega) & 1 \end{pmatrix} \begin{pmatrix} a_A \\ a_P \end{pmatrix} \tag{3.17}$$

where a and b are the input and output fields, the indices A and P refer to the amplitude and phase of the field and the term

$$\mathcal{K}(\omega) = \left(\frac{1}{1 - (\omega^2 - \omega_p^2)/\Theta^2} \right) \frac{1}{\delta_\gamma} \tag{3.18}$$

is the coupling factor, which describes the correlation between the output amplitude and phase quadrature and creates the squeezing in the output field.
In order to quantify squeezing, the quadrature field is measured by an homodyne detector, and the spectral density of the fluctuation of the output quadrature can be written as

$$S_\zeta(\omega) = 1 + 2\mathcal{K}^2 - 2\mathcal{K}(\sin 2\zeta + \mathcal{K} \cos 2\zeta) \equiv \xi_\zeta^2(\omega), \tag{3.19}$$

where ζ is the homodyne angle, with a convention in which $\zeta = 0$ corresponds to the simple amplitude detection of the output field. Taking the minimum over the quadrature of $\xi_\zeta(\omega)$, the ponderomotive squeezing factor can be written as [37]

$$\xi_{\min}(\omega) = \frac{1}{|\mathcal{K}(\omega)| + \sqrt{1 + \mathcal{K}^2(\omega)}}, \tag{3.20}$$

obtained at

$$\zeta_{min}(\omega) = \frac{1}{2} \arctan \frac{1}{\mathcal{K}(\omega)}. \tag{3.21}$$

If Θ lies within the quasi-static regime, we can consider three regimes for the working frequency ω:

1. when $\omega \gg \Theta$, the coupling constant $\mathcal{K}$ tends to zero, then obtaining a vacuum output state (not squeezed);

2. for $\omega \ll |\Theta|$, we obtain a constant $\mathcal{K} = 1/\delta_\gamma$, which means to have a frequency independent squeezed state;

3. when $\omega \sim |\Theta|$ the system experiences a resonance, if Θ is real, with a strong squeezing and highly frequency-dependent squeeze angle, or smooth transition occurs if Θ is purely imaginary.

Therefore, we can obtain a frequency-independent ponderomotive squeezing source with squeezing factor which depends only on the detuning parameter δ_γ, and bandwidth Θ. This squeezing factor ξ_{min} can be lowered indefinitely by taking $\delta_\gamma \to 0$, but according to eq. 3.15 the bandwidth Θ will also decrease in this process, unless input power and/or cavity finesse are increased. Nevertheless, as discussed in [37], such a squeezed state can be transformed into frequency-dependent squeezed states by optical filters.

Therefore, once $|\Theta|$ has been fixed, it is possible to design the opto-mecanical system in order to keep the system in a regime in which ω_p is much lower than $|\Theta|$, allowing us to use the model described above. From the equation 3.14 it is possible to explain the opto-mechanical coupling in a detuned cavity, as an optical spring which works around a detuned point. Indeed, the radiation pressure force arises from the time delay in the cavity response and is proportional to the velocity of the cavity mirrors, with a linear dependence on the cavity length [55]. Then, if the detuning increases (blueshift), this time delay leads to a force in the same direction as the instantaneous mirror velocity, the cavity becomes longer, and the power decreases causing a restoring force, while if the detuning decreases (redshift), the cavity becomes shorter and the decrease of the power results in an anti-restoring force [57].

3.1.1 Towards quantum non-demolition

As already mentioned in section 2.4, quantum non-demolition (QND) interferometers are achieved by creating correlations between the radiation pressure and shot noise. In [35] different ways in which this can be realized are described. In particular, both input squeezing and ponderomotive squeezing are considered as a way to improve the sensitivity of the GW detectors. Therefore, we take inspiration from [35] in order to exploit our optical-spring squeezer (SIPS) to achieve a broadband reduction of quantum noise in Virgo intererometer.
We have seen that ponderomotive squeezing arises from the naturally occurring correlation of light intensity fluctuations (radiation-pressure noise) to mirror position fluctuations (shot noise) upon reflection of light from a mirror. This process can be qualitatively describes as follows: when light (or vacuum) with fluctuations in the amplitude (radiation pressure) quadrature ΔA, and with fluctuations in phase quadrature $\Delta\phi$, is incident on a mirror, the back-action force of the light on the mirror causes a displacement of the mirror proportional to ΔA. If the position signal is measured in the phase quadrature, then the noise on that measurement is given by $\Delta\phi - \mathcal{K}(\omega)$, where $\mathcal{K}(\omega)$ is a measure of the backaction coupling and depends on the frequency of oscillation of the mirror, ω. If a single quadrature is measured at the output of the interferometer, the noise on that measurement will depend on $\mathcal{K}(\omega)$ at each frequency ω. If, however, one could measure an admixture of quadratures with a frequency dependent homodyne angle, $\zeta(\omega)$, which is a function of $\mathcal{K}(\omega)$, it would be possible to eliminate ΔA from the measurement, at all frequencies [48]. Since, with this approach, the measured quadrature varies with frequency, this technique is called **variational** or **frequency-dependent homodyne readout**.
Another way to realize QND in an interferometer is through the **dinamical correlation**. It consists in modify the interferometer mirror dynamics by coupling to the light. This coupling is generated by the fact that the radiation pressure force not only imposes random fluctuations on the positions of the interferometer mirrors, but also exerts a restoring force with a deterministic frequency-dependent spring constant, i.e *ponderomotive rigidity* [58]. The resulting dynamical correlation of the shot noise and radiation pressure noise [59] are manifestations of quantum nondemolition (QND), in which the correlations lead to below-SQL noise limits.

The discussion described so far in this section, allows us to highlight the fundamental constraints on the parameters to choose for the opto-mechanical design of the experiment. In [57], it is discussed and analysed that, given a suitable seismic pre-isolation system (see sec. 1.3.5 and fig. 1.10), by tailoring the design of the mirror suspension system (i.e. double pendulum with monolithic suspension), it is possible to realise a table-top setup where a Fabry-Perot cavity, then doubled in an interferometric configuration, employs suspended mirrors of inch-size-scale with the end mirror lighter than the input one and dominated by radiation pressure noise. This is the case of the experiment SIPS presented in this thesis work. The optical and mechanical designs, together with the study for the choice of the fundamental parameters of the experimental setup and the expected noise budget are discussed in the following sections.

3.2 Experimental setup

The idea of a suspended interferometer working in radiation pressure regime for the generation of ponderomotive squeezing, discussed in this thesis, has been preliminary studied in the past years, starting from the study done in [52]. The preliminary R&D work started around 2012 and involved many Italian research institutions, among which we can list: the University of Naples Federico II and the INFN-Napoli branch together with the University of Rome Tor Vergata and the INFN-Roma2 branch for the work on general optical design; the University of Pisa and the INFN-Pisa branch which designed and realised the main optical bench where the experiment will be installed; the University of Urbino for the monolithic suspension production; and, last but not least, the University of Rome La Sapienza and the INFN-Roma branch, which has been and is still actively working on the opto-mechanical design and realization of the experiment setup. Later, in 2017, the experiment also received new funding for the R&D by INFN-CSN5, under the name of SIPS (Suspended Interferometer for Ponderomotive Squeezing) with also the collaboration of the INFN Perugia branch for the design and realization of the monolithic suspensions. From the study done in [52], the fundamental design requirements are chosen in order to reduce the thermal noise well below the level of the radiation pressure noise of the system, as will be discussed in more details in section 3.2.1. In this section the optical and mechanical design of the experimental setup for the ponderomotive squeezer is described. It is an interferometer similar to that used for GW detection: a Michelson interferometer with Fabry-Perot cavities in each arm, with all the mirrors suspended as pendulums. While squeezed light could be produced with the use of a single cavity and suspended mirror, the use of interferometry is necessary to introduce common mode rejection of the laser noise, which would otherwise mask the squeezed light [37]. For this purpose, the experimental design of SIPS has been developed starting from the analysis already done in [57] for a single optical cavity, where it is also proposed to combine the two optical cavities, to obtain a radiation pressure limited interferometer.

In order to achieve the goal of measure squeezing levels, we set the most critical

features of the optical design, described in section 3.2.2, which includes:

- a powerful input laser beam;
- Fabry-Perot cavities with high finesse to have a large optical power incident on the suspended mirror to have high sensitivity to radiation pressure,
- substantial detuning of the two cavities (comparable to the cavity linewidth) which would allows to create the optical spring.

3.2.1 Noise budget of SIPS

In order to produce ponderomotive squeezing, the suspended interferometer SIPS must be dominated by radiation pressure noise. Such kind of instruments are affected by several noise sources. Nevertheless, in a Michelson interferometer, the common mode rejection can be exploited to attenuate the effect of the many limiting noise sources, such as laser frequency fluctuations, equal in the two arm-cavities. The idea itself of working in the low frequency regime implies the need to consider two important limiting noises of the interferometer sensitivity: the seismic noise and the thermal noise. The long experience of work on the Virgo Superattenuators for the attenuation of the seismic noise has been considered to control this source of noise. Thus, beating the thermal noise at low frequency is the priority in an experiment such as SIPS primarily devoted to demonstrate the ponderomotive effect. The sensitivity curve of a ground based gravitational wave detector in the frequency band between 10 and 200 Hz is dominated by the thermal noise of the mirror suspension fibers (at lower frequencies) and by the thermal noise of the mirrors bulk and coating layers, which are the most likely to hide the radiation pressure effect. From the expected sensitivity curve of Advanced Virgo (see fig. 1.4), we can see that the suspension thermal noise limits the sensitivity in the frequency band around 10 Hz. Therefore, the realization of an interferometer which is radiation pressure dominated in the frequency range between 1 Hz and few kHz, strongly depends on the capability to optimize the thermal noise linked to the suspension system of the mirrors and to the coatings of the main optics. Finite element simulations have been carried out in order to define the main characteristics of the mirror suspensions and coatings, to reduce thermal noise and make the radiation pressure noise dominant in the desired frequency range [57]. This detailed analysis led to the choice of a double stage suspension system, which has the advantage to further attenuate the seismic noise at the level of the mirror and to reduce, at the same time, the suspension thermal noise [57].

This has been modelled using the fluctuation dissipation theorem [18], as

$$X_{\mathrm{therm}}(\omega) = \sqrt{\frac{4k_{\mathrm{B}}T}{\omega^2}\Re\left\{[Z^{-1}(\omega)]_{22}\right\}}, \tag{3.22}$$

where k_{B} is the Boltzmann constant, T the temperature, and $[Z^{-1}(\omega)]_{22}$ the element of the inverse of impedance matrix that corresponds to the suspended mirror. Note that the impedance matrix takes into account all the dissipating processes that

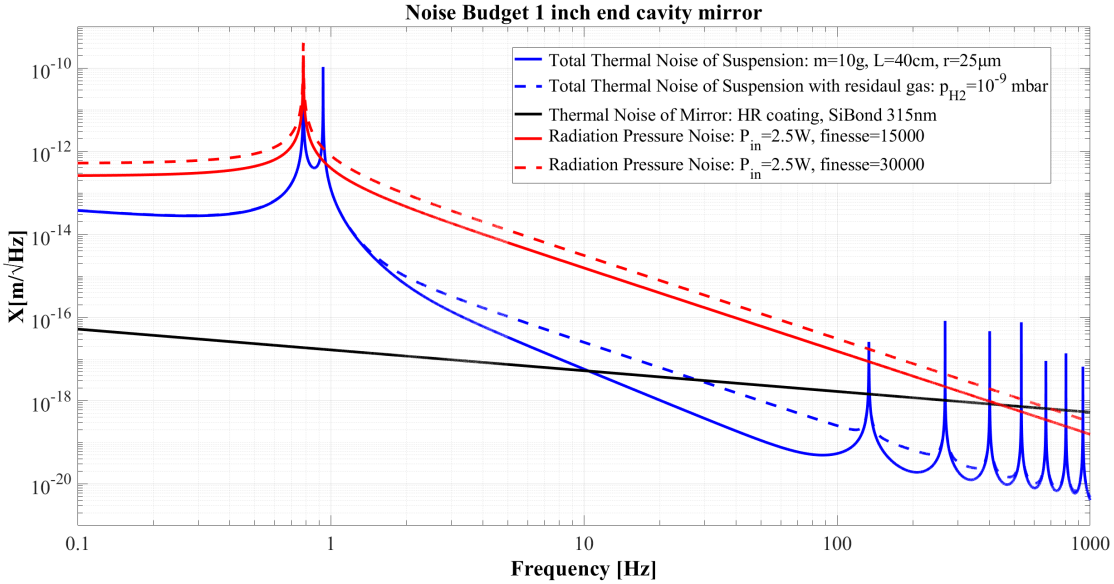

Figure 3.1: Expected noise budget for 1 inch diameter end mirror of 10 g of mass, in a double suspension configuration. Blue curve is the total suspension thermal noise, computed considering also noise related to violin modes of the wires. The blue-dashed curve represents total suspension thermal noise when considering the effect of residual gas damping due to a pressure p=10^{-9} mbar of molecular hydrogen. Black curve represents the mirror thermal noise estimated with finite element analysis [57].

contribute to the mechanical dissipation determining the suspension thermal noise. A similar approach was used to estimate the transverse vibration modes of the suspension wire, called violin modes, which also behaves as a vibrating string [57], and can be modelled as [60]

$$X_{\mathrm{vio}}(\omega) = \sqrt{\frac{4k_{\mathrm{B}}T}{\omega}\frac{2\rho r^2 l}{\pi m^2}\sum_n \frac{1}{n}\frac{\omega_n^2\phi_n}{(\omega_n^2-\omega^2)^2+(\omega_n^2\phi_n)^2}}, \tag{3.23}$$

where r and l are the fiber radius and length and ω_n, ϕ_n represent the frequency and the total loss angle [57]. The overall pendulum loss angle ϕ_p includes all the dissipation processes in the system, and thus is given by the sum of all these contributions

$$\phi_p(\omega) = D_{ilF}\left(\phi_{\mathrm{SiO2}} + \phi_{te}(\omega) + \phi_e\right), \tag{3.24}$$

where D_{ilF} is the dilution factor, as defined in [57], and ϕ_{SiO2}, ϕ_{te}, ϕ_e are respectively the structural, thermoelastic, and surface loss angles. Therefore, the total thermal noise of the double suspension system is given by the square of the quadratic sum of the two components 3.22 and 3.23 as

$$X_{\mathrm{ThNS}}(\omega) = \sqrt{X^2_{\mathrm{therm}}(\omega) + X^2_{\mathrm{vio}}(\omega)}. \tag{3.25}$$

The mirror thermal noise has been estimated via a Finite Element Analysis with ANSYS® software [57], using Levin's approach [61], and is given by

$$X_{\mathrm{ThNM}}(\omega) = \sqrt{\frac{8k_{\mathrm{B}}T}{\omega F_0^2}U_{\mathrm{mir}}\phi_{\mathrm{tot}}}, \tag{3.26}$$

where $U_{\rm mir}$ is the total strain energy of the suspended mirror under an impinging Gaussian pressure, and $\phi_{\rm tot}$ is the overall loss angle, given by the sum of all dissipating contributions [57]

$$\phi_{\rm tot} = \phi_B + \sum_{\rm lay} \frac{U_{\rm lay}}{U_{\rm tot}} \phi_{\rm mat}^{\rm lay} = \phi_B + \frac{U_{\rm coat}^{HR}}{U_{\rm tot}} \phi_{\rm mat}^{HR} + \frac{U_{\rm coat}^{LR}}{U_{\rm tot}} \phi_{\rm mat}^{LR} + \frac{U_{SB}}{U_{\rm tot}} \phi_{SB}. \tag{3.27}$$

In this equation, ϕ_B is the loss angle related to the bulk, and $\phi_{\rm mat}^{lay}$ is the loss angle of the material composing the layer, while U_{lay} and $U_{\rm tot}$ are the layer strain energy and the total strain energy, respectively. As a result of this analysis, the geometry of the suspensions and the dimensions of the suspended mirrors was chosen. As shown in figure 3.1, the choice to use high reflective mirrors with Advanced Virgo-like coatings and 10 g mass suspended with monolithic Virgo-like suspension system optimises both mirror and suspension thermal noise below the radiation pressure fluctuations, a fundamental condition to have the optical spring effect observable and exploitable [62]. Another noise source to be considered is the one coming from the seismic background, which causes fluctuations of the mirror position, represented by a power spectral density proportional to ω^{-2}. Among other noise sources, the effect of the residual gas damping must be also considered, as detailed described in [57], and as also considered in the figure 3.1.
All the noise sources, should be compared to the expected radiation pressure noise, which, for a pendulum suspension in a Fabry-Perot cavity, can be modeled as [52]

$$X_{\rm RP}(\omega) = \frac{2\mathcal{F}}{\pi m} \sqrt{\frac{8hP_{\rm in}/(\lambda c)}{(\omega_p^2 - \omega^2)^2 + (\omega_p^2 \phi_p(\omega))^2}}. \tag{3.28}$$

This analysis leads to the estimation of a radiation pressure noise $X_{\rm RP}$ at 10 Hz of about 3×10^{-15} m/$\sqrt{\rm Hz}$, which means that the radiation pressure noise will be approximately 600 times higher than the thermal noise at 10 Hz (see figure 3.1) [57, 62]. From this analysis, it was possible to choose the parameters for the design of the main optics, which ensure a theoretical ponderomotive squeezing factor of $\xi_\zeta(\omega)$=18 dB. From the experimental point of view, all the possible losses in this opto-mechanical system should be considered, allowing to obtain a more realistic ponderomotive squeezing factor of about 7 dB.
SIPS will be first used as a table-top demonstrator of the EPR experiment and for this reason placed in a vacuum tank in the R&D squeezing laboratory at EGO (Virgo site) where the EPR setup is under construction [62, 12]. Indeed, for this first phase of the experiment, the noise budget must take into account the seismic noise level in that location and, if required, new seismic noise measurement must be realised. From some preliminary measurements, it has been found that the seismic noise at EGO site is lower than radiation pressure noise in a wide range of frequencies above 40 Hz. Moreover, the preliminary analysis done in [62] show that a suitable monolithic suspension of the main optics and high-quality coatings allow to keep the thermal noise well below radiation pressure noise. Given these considerations, it seems that no further modifications are required in the design of SIPS before its integration with the EPR experiment. Then we can state that SIPS is exploitable as demonstrator of the EPR squeezing in a frequency band between 40 Hz and 700 Hz.

3.2.2 Optical bench design

The analysis illustrated in sections 3.1 and 3.2.1, explains the choice of the different features of the experiment setup and is a guide for the choice of optical and mechanical parameters used to design and build the interferometer SIPS. The material chosen for both mirrors and suspension fiber is the fused silica, SiO_2, due to the fact that it combines the characteristics of robustness, necessary to suspend the mass of mirrors, to those of a loss angle extremely reduced [63]. The use of suspensions of the same material of the mirrors allows the realization of a monolithic structure, thus minimizing the losses which originate at the contact points between different material [64]. The small-scale suspended interferometer (SIPS) design is shown in

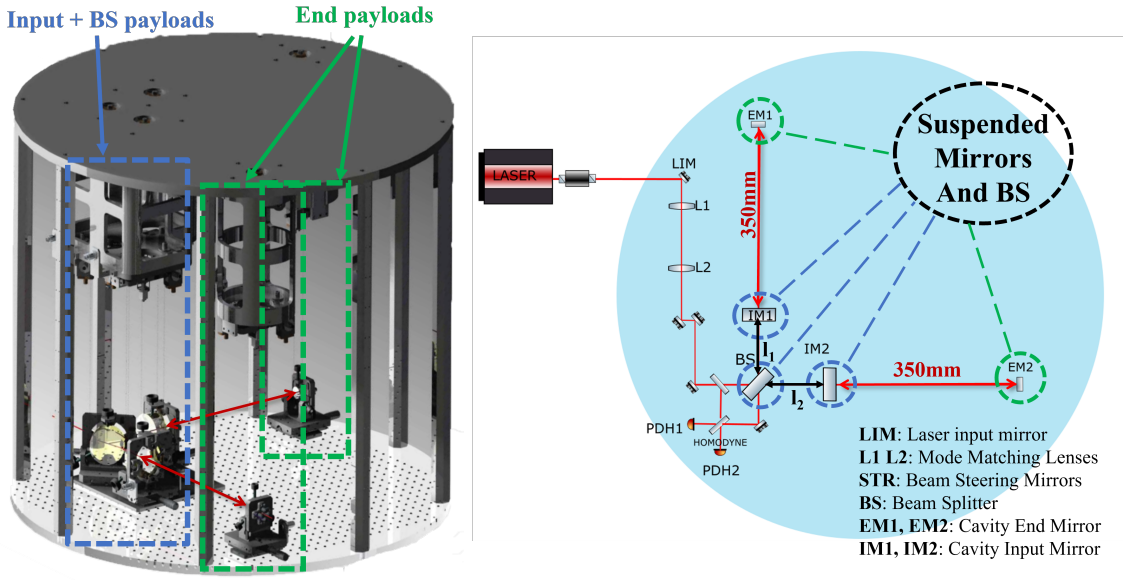

Figure 3.2: Main mechanical design with suspended optics (left) and a simplified main optical bench design (right) of the double suspended bench setup for SIPS.

figure 3.2. It is a Michelson interferometer, which includes two high finesse Fabry-Perot (FP) cavities and a fused silica beamsplitter (BS) of 3 inches diameter. Each FP cavity is composed by two concave fused silica mirrors: a 1 inch fused silica end mirror (EM), 10 mm thick with a mass $m = 10$ g and a 3 inch fused silica input mirror (IM), 30 mm thick with mass of 300 g. This is the best combination of parameters chosen for the main optics, which follows from the suspension thermal noise analysis done in [62], and they are summarized in table 3.1. As explained in section 3.1, the optical spring is the predominant feature of the detuned arm cavity. In particular, when a cavity is detuned, the optical spring modifies the response function of the differential mode from a free mass (ignoring the pendulum frequency) to a harmonic oscillator with resonant frequency Θ (see eq. 3.15). Following the work done by Corbitt et al [37], we can consider the frequency regime $\omega \ll |\Theta|$, in which the response of cavity lengths to external disturbances (due to seismic or thermal noise) is suppressed by Θ^2/ω^2 and the ideal output state is a frequency independent squeezed vacuum with squeeze factor as a function $\delta_\gamma = \delta/\gamma$. Based on this qualitative consideration, in order to obtain a substantial squeeze factor, we need to choose

an optical configuration such that δ is of the same order of magnitude as the cavity linewidth γ. We have considered a target squeeze factor of 18 dB, which is the ideal value obtained in absence of optical losses and technical noises (allowing to keep the contribution of the vacuum fluctuations from the anti-symmetric port to the total noise small enough). This determines the value of the detuning parameter, which it has been chosen to be $\delta_\gamma = 0.3$. The low mass values for the end mirrors has been chosen to allow a high optical spring resonance. Moreover, the mirror coatings are realised in order to have very high finesse Fabry-Perot cavities, thus increasing the effect of radiation pressure noise, for the aim of generating of ponderomotive squeezed light. Indeed, a large finesse values of the arm cavity is needed to have the optical spring frequency, Θ, as high as possible, for a better noise suppression and to reduce intra-cavity losses.
At present, the substrates and coatings of the main optics have been procured by INFN-Roma group at the Physics department of La Sapienza University of Rome, as shown in figure 3.3.

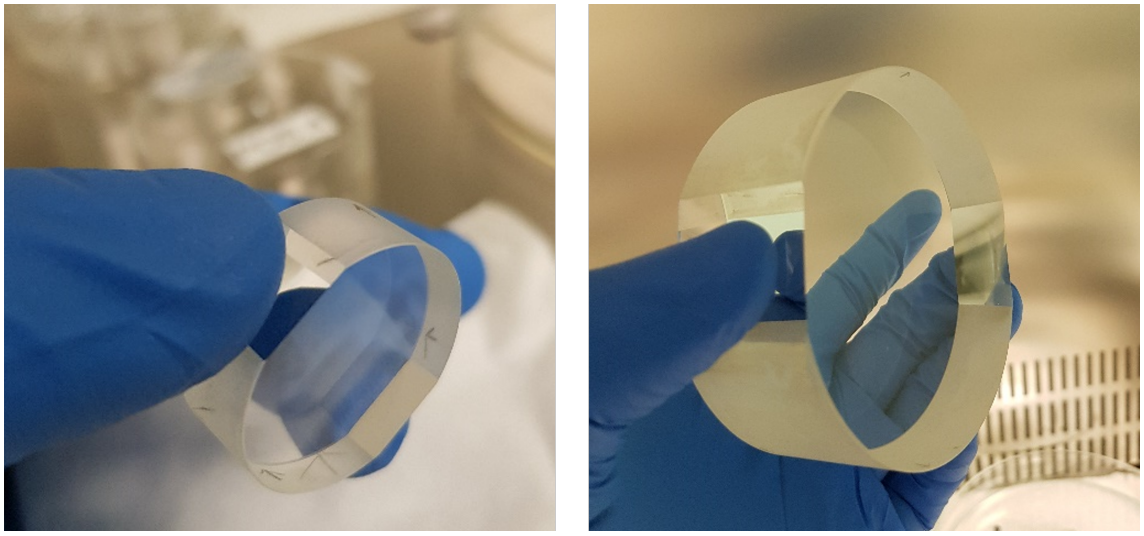

Figure 3.3: Main optical elements realized with a cylindrical bulk made of fused silica, with a suprasil substrates: 1 inch end mirror (left); 3 inches input mirror and BS (right).

In particular, finite element analysis described in [62] gave the requirement on mirror (and BS) coatings, (also shown in table 3.1). Moreover, given the very high laser

Main Optics	Diameter	Weight	Thickness	RoC	T Coatings
IM	3”	300g	30mm	250mm	260ppm @0°
EM	1”	10g	10mm	250mm	1ppm @0°
BS	3”	300g	30mm	0	50%±0.05% @45°

Table 3.1: Parameters chosen from finite element analysis on mirror thermal noise [57] for the main optical elements: they are all realized with a fused silica (SiO_2) bulk and Suprasil substrates. The required coating transmissivity, T, are computed at the main laser frequency of 1064 nm.

intensity value, suited coatings are required: they must have a high reflectivity on

intra-cavity surfaces, with a transmissivity, or a power loss of T = 1 ppm at 1064 nm, in order to reach the suitable high value for the *finesse* of FP cavities. These coatings have been realized by the Laboratoire des Matériaux Avancés (LMA), located in Lyon, France, which is the same laboratory which manufactures the coatings of Virgo and LIGO test mass mirrors [23, 25]. With this requirements the FP cavities has a *finesse* of $\mathcal{F} = 23000$. Although a high finesse value increases the effect of radiation pressure noise, it also limits the optical spring stability. Then, to ensure the stability condition for the optical cavity, this has been designed and realized to have a length of $L = 350$ mm and mirrors with a radius of curvature (RoC) of 250 m, which gives a g factor of about 0.16. Moreover, the distance between BS and the two input mirrors are slightly different in order to compensate for the optical path inside the BS and for allowed space constraints: they are $l_1 = 73$ mm and $l_2 = 105$ mm respectively for the north and east arm, as shown in figure 3.2. The input laser power required at the SIPS bright port is $P_{in} = 2.5$ W, which means that the power received in each arm will be $P_{in}/2 = 1.25$ W, corresponding to $P_{st} = 18.1$ kW of circulating power inside each cavity. This has been chosen considering that a larger value increases the optical spring frequency Θ, and with a stored power $P_{st} > 0.2$ MW thermal effects would appear, leading to the degradation of the cavity behaviour [62].

3.2.3 Mechanical design

The mechanical design of the mirror oscillator, crucial to the performance of the interferometer, is here described, starting from the model analysed in [57]. A scheme of this system is shown in figure 3.4. All the principal optical elements will be mono-

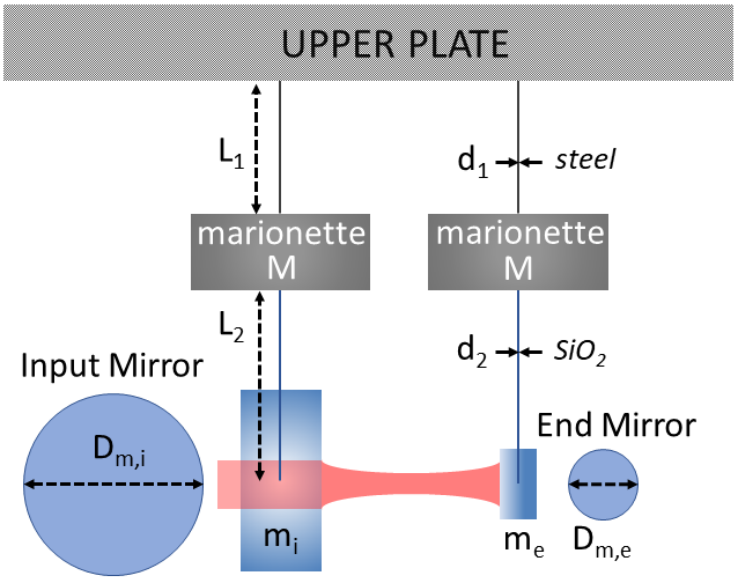

Figure 3.4: Scheme of the suspended optical cavity modeled in [57]. Each mirror are suspended from an intermediate stage called *marionette*, thus i can be described as a double stage pendulum.

lithically suspended to an intermediate stage, called marionette, through thin fused

silica fibers (SiO_2). The monolithic suspensions are made by pulling bar of bigger diameter of few mm of highly pure fused silica with a particular technique which uses CO_2 lasers machine, which is the technique developed and currently used by Virgo and LIGO collaborations (see fig. 3.6). For the requirements of this experiments

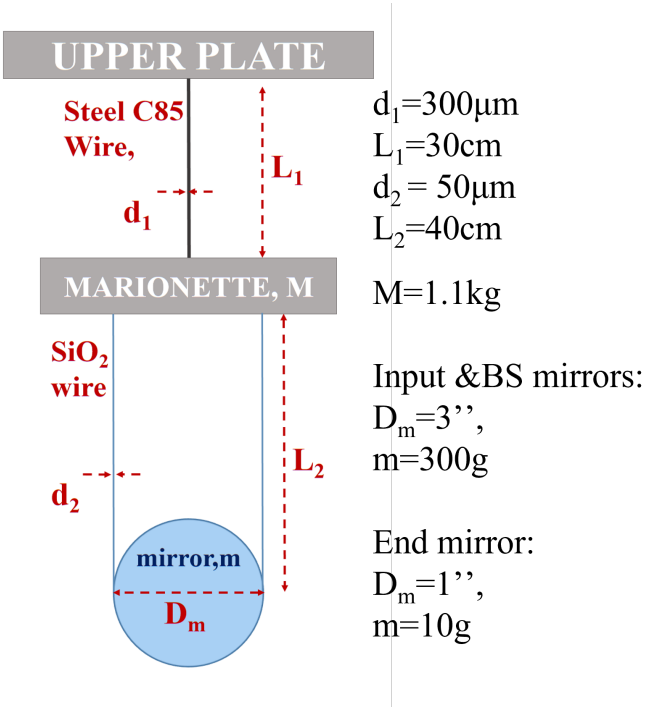

Figure 3.5: Scheme of a SIPS *mini-payload* with a detailed view on the monolithic suspension of the main optics, designed with a Virgo-like technique for thermal noise reduction.

demonstrated in the study [57], it turned out that, in order to reduce the associated thermal noise, silica fibers must have a diameter of 50 μm with a length $L_2 = 40$ cm, as shown in figures 3.6 and 3.5. With this suspension system, the mirrors (and BS) with the marionettes form the so-called *mini-payloads*, in analogy with those of the main suspended optics of Virgo (see figure 3.5).

All the main optical and mechanical components (the main optical bench) are held to an upper plate. Indeed the suspension of the main optical elements allow not only the mirrors to behave as free masses in the experimental frequency band, but it also have the advantage of isolation from seismic noise. To improve the seismic isolation, the parameter for the design has been chosen to have a pendulum resonant frequency of $\sim$0.8 Hz. Moreover, the entire interferometer will be in turn suspended through a complex chain of mechanical filter inspired to that of Virgo Superattenuators [56, 24]. Indeed, GW detectors such as Virgo and LIGO, demonstrated that it is possible to filter out the natural seismic vibrations: in Advanced Virgo the mirrors are suspended from a vibration isolator that filters this noise at frequencies larger than those of the normal modes of the suspension itself [65]. In particular, in Virgo the Superattenuator (SA) is capable of 180 dB of attenuation at 10Hz [66, 24]. Its working principle is based on a multistage pendulum acting on seismic vibrations as a chain of second order mechanical low-pass filters [67] and it is characterized by

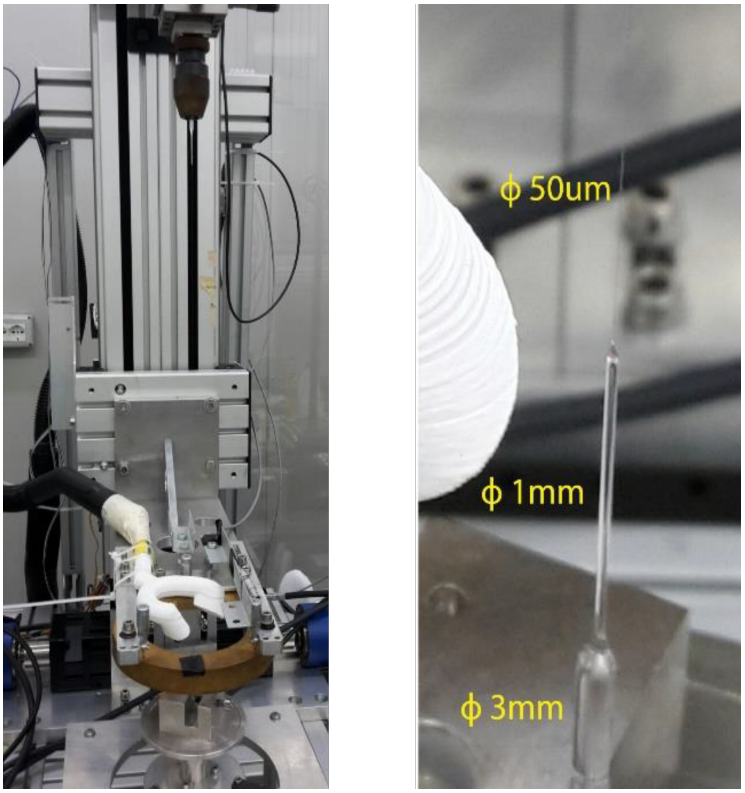

Figure 3.6: Picture of the $50\mu m$ diameter fused silica fibers produced with the same technique used for Virgo fibers (right), using the CO_2 laser machine at EGO laboratories (left). This is a first successful production test.

very low frequency normal modes, in the range of 0.04-3 Hz [65]. It is foreseen to implement such a system to exploit the seismic attenuation for SIPS, for its use as a ponderomotive squeezer. For this reason, SIPS has been initially designed to be suspended from the last steering filter of the SA chain. Indeed, a full scale prototype of a Superattenuator is currently available for test in the facility located at EGO (Virgo site) and it is planned to use it for the SIPS experiment [62]. This original idea to suspend SIPS bench through the Superattenuator Facility (SAFE, see fig. 3.7), gives the requirement for SIPS bench to be compliant with allowed size and weight to be suspended with this system. In particular, the suspended bench has been realized with a height of 800 mm, diameter of 960 mm and its weight is of about 150 kg. Moreover, it is necessary to find a trade-off between the experimental constraints given by the allowed space in SAFE and the suspension system. In figure 3.7 is shown a rough sketch of the original idea of suspending SIPS to the SAFE facility.

Nevertheless, as already mentioned in section 3.2.1, in the first application of SIPS to replace GW interferometer for test of EPR squeezing technique, the implementation of the superattenuator SAFE is not required. Moreover, the SA research facility at EGO cannot be ready before the planned integration with EPR setup. Hence, in the noise budget of SIPS computed in [62] a conservative approach as been adopted considering the seismic noise measured at Virgo site [68]. The plot in figure 3.8 (red curve), show the noise for the double-stage suspended mirror. In particular, it is

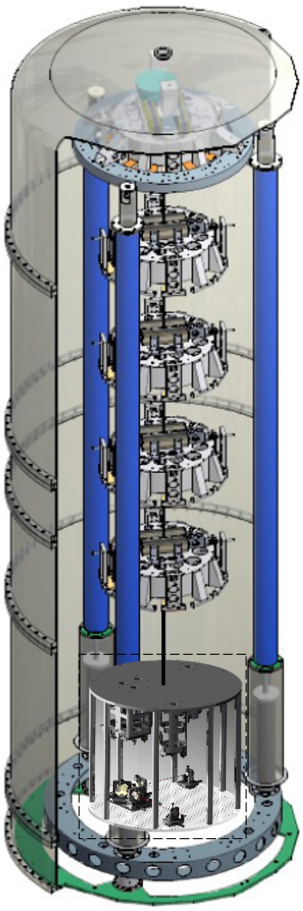

Figure 3.7: SuperAttenuator Facility (SAFE) at EGO-Virgo site, with a rough sketch of the implementation of SIPS suspended bench.

found that seismic noise is lower than radiation pressure noise in a wide range of frequencies above 40 Hz, assuring a quantum radiation pressure limited bandwidth of (40-700)Hz [62]. This tells us that, even without the use of a superattenuator, SIPS interferometer can be used as a test bench for the EPR experiment.
The main optical elements of the interferometer and their intermediate suspension stage (marionette) are controlled with magnet-coil actuators on both mirror and marionette, and it must be locked by a closed loop feedback control system. The study of the opto-mechanical interaction inside SIPS FP cavities is one of the main topics of this thesis and it represents a fundamental preliminary step to achieve the important goal of the development of an optimal control system for the interferomer (see Chapter 5). The mechanical prototype of SIPS is under development and test for the suspension and control systems. In the near future, the fused silica (SiO_2) fibers for suspension of the main optics will be produced using the CO_2 laser machine at Virgo site and the monolithic suspension system of the SIPS interferometer main optics will be implemented. This kind of monolithic suspension is already implemented in GEO600 and in the GW ITFs Virgo and LIGO, but its realization at small scale implies a different design respect to that used for the bigger mirrors of GW ITFs, and some R&D for the integration with the suspended interferometer. A first production test have been succefully realized as shown in figure 3.6.

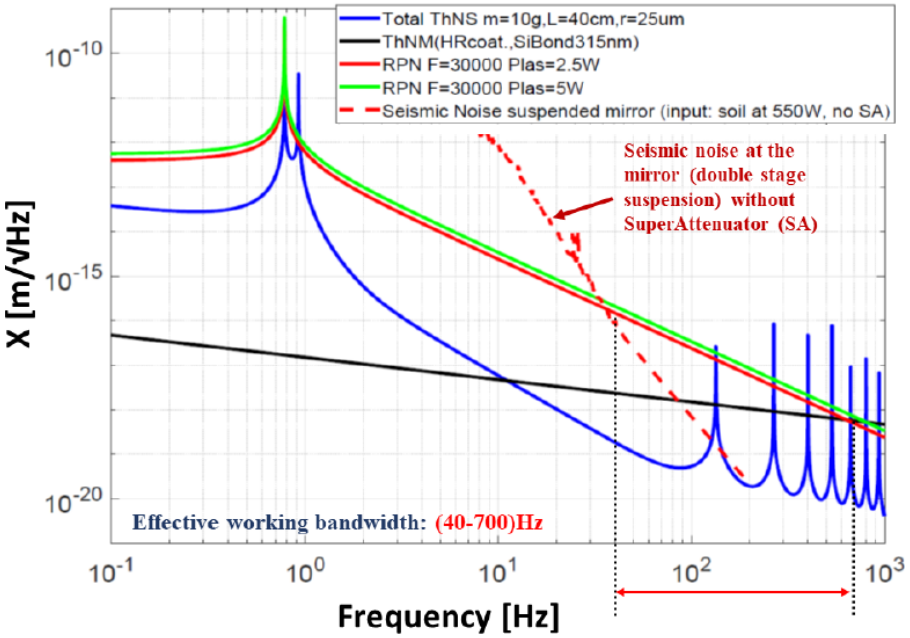

Figure 3.8: Expected noise budget of SIPS compared with the seismic noise at Virgo site (red dashed curve). For more detail see [62].

At present, dummy elements that reproduces the main optics of the interferometer are used in a preliminary phase to develop, test and validate the local control system. This activity represent the core of the experimental work I have done during my PhD thesis and is discussed in detail in Chapter 4. In particular, the test of local control are carried out on a prototype dummy end mirror, which has the same dimensions of the fused silica end mirror designed for SIPS and is made of aluminium in order to have a mass close to that of the fused silica one. This dummy mirror is then suspended to the marionette through niobium wires having a diameter of about 56 μm, similar to that of the final SiO_2 monolithic suspension fibers, and the marionette is in turn suspended to the upper plate through one steel wire with a diameter of 300 μm, that is likely to be the same kind of wire (material and geometry) that will be used in the final suspension design, as described in [57].

3.2.4 SIPS FP arm cavities

Some work was carried out on the design of SIPS laser injection line, as reported in [69], with the goal to provide the proper beam shape and optical power of the main laser, to be mode-matched to the arms of SIPS interferometer. This work involved some optical simulations carried out on SIPS arm cavities, performed with the software FINESSE, in order to compute the eigenmode of the interferometer arms and to analyze their power budget and spectrum. In figure 3.9 is shown the optical scheme of one Fabry-Perot arm cavity of SIPS and the main optical characteristics are highlighted [69].

As reported in eq. 1.65 of section 1.2.3, the half of the FP cavity linewidth is the cut-off pole frequency, f_p. From the choice of parameters for SIPS optical bench

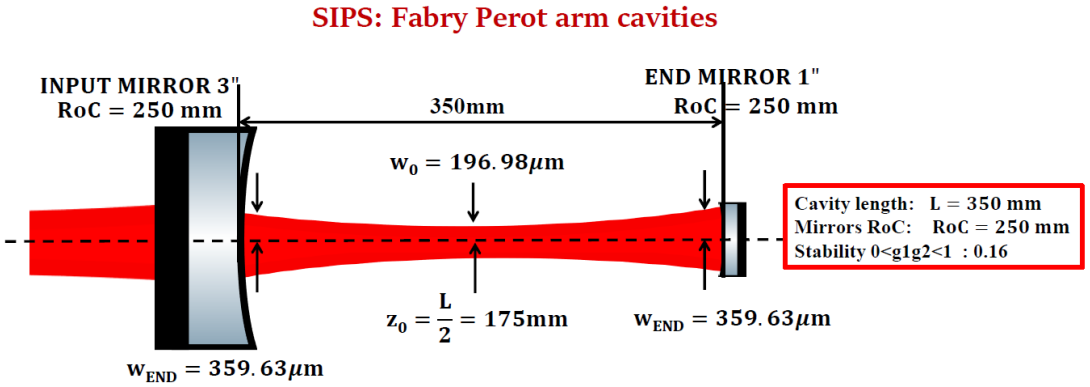

Figure 3.9: Optical scheme and main optical characteristics of one Fabry-Perot arm cavity of SIPS [69].

design, discussed in the previous section, SIPS FP cavities have a pole frequency f_p=9.31 kHz, which means that the FP response at input signals with $f \gg 9.31$ kHz will be damped. SIPS FP arm eigenmode shape is computed by assuming a pure Gaussian beam (the main laser) incoming into SIPS, thanks to the presence of the so-called Input Mode Cleaner (IMC) cavity. The physical goal of a MC cavity is filtering out the spurious transverse higher order modes (HOM) eventually present in the incoming beam (in our case is SIPS main laser) in order to provide a (nearly) purely Gaussian TEM_{00} beam in output. The design project of the IMC for SIPS was carried out, as reported in [69], taking into account several requirements, among which HOM filtering and the IMC transmitted power are the most relevant for our discussion. The basic condition for which the produced transmission spectrum is not contaminated with power coming from the HOMs, when the cavity is locked on the TEM_{00} mode, has been first checked by simply observing at the distance between lines in the transmitted spectrum, i.e. the Transverse Mode Spacing (TMS), comparing the TMS with the FWHM. The condition is satisfied when TMS$\gg$FWHM. Therefore, the distance between lines of adjacent orders should be greater than the cavity linewidth, in order to avoid superposition between Gaussian and HOM modes. Although every tested configuration satisfy this condition, this is not sufficient for ensuring that no overlaps between lines occur. More accurate tests have been done, searching for a too large contamination coming from the HOMs, by inspecting the transmission spectrum in search of overlaps between generic TEM_{nm} modes and the TEM_{00} [69]. All the possible configurations have been simulated, by examining the spectrum and the power budget, providing the ranges for the physical parameters of the IMC resonator and leading to the choice of the best IMC candidate. Then, thanks to the presence of the IMC cavity, we can have a nearly pure Gaussian beam injected into SIPS bright port. Moreover, the requirements of an input power of 2.5 W for SIPS, gives the constraint on the IMC transmitted power, which clearly must be higher than this value. On the 10th of January 2023, we received the mechanics of the IMC, but we should wait the end of March for the optics with custom made coatings. Then, we will be able to test the IMC performances and compare them

to the design. Another analysis performed on SIPS is about the spectrum shown by

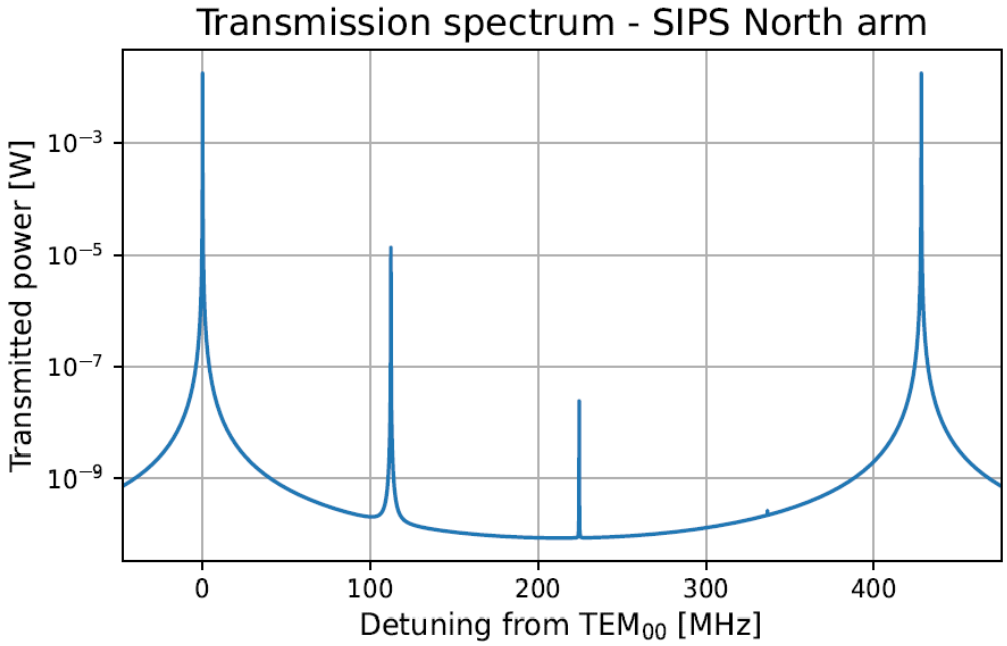

Figure 3.10: SIPS arm transmission spectrum simulated in [69], with the highest HOM peak more than 100 times weaker than the main resonances.

each arm, considering a pure Gaussian beam injected into the interferometer. This study was necessary to evaluate the possibility that some HOMs are created into SIPS itself: this can happen in case of misalignment of the beam into the cavities, and if there is a mismatch between the beam and the eigenmode of the cavities. It has been found that, due to the high *finesse* of the arms the suppression factor is greater than 65 dB, which is high enough to suppress very efficiently the non-Gaussian modes eventually created inside SIPS arms [69]. Moreover, the injection line from the IMC cavity into SIPS is not direct. This is due to a difference between the height of the main EPR optical bench and the viewport of the vacuum chamber that will host SIPS alone (without SAFE) centered on the main optics of SIPS. This height difference between the beams on the EPR optical bench and SIPS main optics is about 60 cm. This requires the design of a periscope and of an auxiliary bench, in order to first ensure that the beam coming from the IMC will reach the central beam-splitter of SIPS and, most important, to be mode matched with SIPS cavities. Considering the input power of 2.5 W given by design for SIPS, the mode-matching of IMC beam to a SIPS cavity eigenmode has been calculated and the results give an amounts for both SIPS arms of $\sim 99.9\%$. Figure 3.10 shows how the quite low degree of asymmetry in the small-scale ITF layout, determines a little power lost into HOMs. Indeed, even if the beam entering the interferometer is a nearly pure Gaussian beam and perfectly aligned, some HOMs can be created in the cavity for mismatches. Nevertheless, it was found that they are very well suppressed, with a suppression factor $\gtrsim 65$ dB [69]. Then, thanks to a large power gain due to the high *finesse* of SIPS FP cavities, which is found to be $G = 2\mathcal{F}/\pi = 1.5 \cdot 10^4$, we can assure a circulating power of 18.1 kW inside SIPS arms, when they are put in resonance: the results of this analysis is shown in figure 3.11.

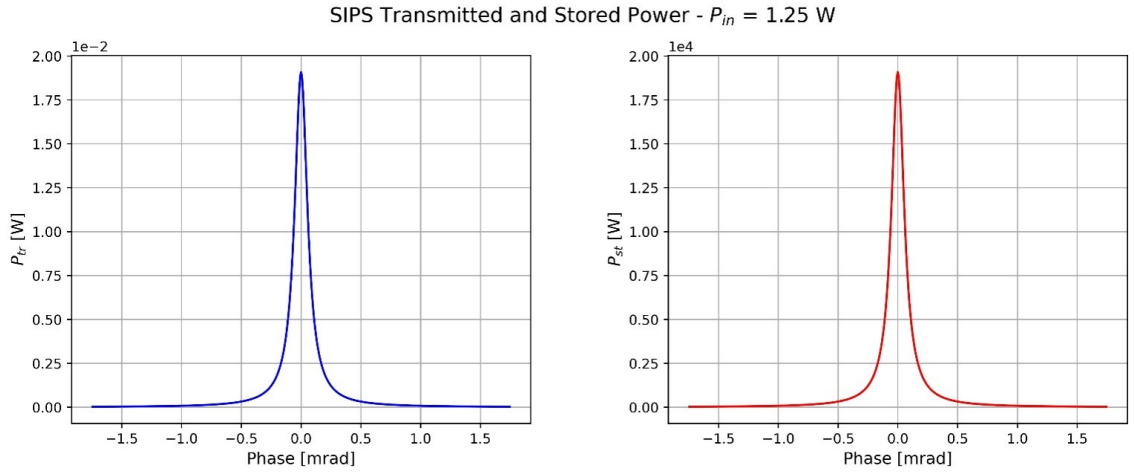

Figure 3.11: SIPS cavity transmitted and stored power obtained from simulation done in [69], considering an input power $P_{in} = 1.25$ W.

This is an important point for the research presented in this thesis, since this level of power assures that the beam exiting from the end mirrors still carries a power $P_{end} = T_{EM} \cdot P_{st} = 18.1$ mW, which is high enough to be detected with a photodiode. This is necessary to acquire information about the status of the cavities, in order to control the cavities and acquire the look to keep them in resonance. Indeed, given the high input power and gain, the circulating power must be monitored. In Table 3.2 are listed the main features of the SIPS Fabry-Perot cavity resonators, some of which also resulting from the analysis done in [69]. As shown in table 3.2,

Parameter	Value
L [mm]	350
T_{IM}	$270 \cdot 10^{-6}$
T_{EM}	$1 \cdot 10^{-6}$
A_{IM}	$1 \cdot 10^{-6}$
A_{EM}	$1 \cdot 10^{-6}$
$\mathcal{F}$	23010
FSR [MHz]	428.3
FWHM [kHz]	18.61
f_p	9.31 kHz

Parameter	Value
TMS [MHz]	270.2
$g_1 g_2$	0.16
P_{st} [kW]	18.1
P_{end} [mW]	18.1
w_0 [μm]	197
I_{max} [kW/cm^2]	29720
$w_{IM;EM}$ [μm]	359.6
$I_{max,IM;EM}$ [kW/cm^2]	8915

Table 3.2: List of some important parameters chosen from design requirements and optical simulations of SIPS FP cavities [69].

the waist of the eigenmode has been founded to fall at the center of the cavity (as expected) with a value of $w_0 = 197.0\mu$m, which corresponds to a beam width of $w_{IM;EM} = 359.6\mu$m on both the input and end mirrors. With the optical set up of the IMC designed by [69], it is not only possible to tune the input power in order to increase the radiation pressure experienced by SIPS arm cavities end mirrors, but also to have a clean Gaussian intensity profile of the beam injected into SIPS, which, thanks to the IMC action, presents a high level of mode-matching with the arms of

the small-scale interferometer.

3.2.5 Summarized consideration on SIPS design

Some main milestones achieved for the realization of the experiment are summarized and listed here:

- realization of the suspension mechanics for the main optics (mirrors and BS);
- simulation of thermal noise and radiation pressure for the interferometer mirrors, for the choice of suitable opto-mechanical parameters [57, 62];
- production of the main optics substrates and coatings;
- production of test fused silica fibers (SiO_2) with diameter $\phi = 50\mu$m in collaboration with the INFN of Perugia;
- simulation of SIPS arm cavities spectrum and power budget [69];
- realization and tests of a local control system for a mini-payload suspension of the main optics;
- design and realization of a new suspension mechanics tailored to optimize the actuation system for alignment and control (implementation in progress in all the mini-payloads of SIPS) [30];
- assembly of the new produced marionette of one end mini-payloads of SIPS, for the implementation of the local control system.

Starting from the initial tests done on LabView code for local control already implemented for old mechanics, some results from test of the control on the new suspension system will be presented in chapter 4.

The choice of high $finesse$ cavities makes the control of such kind of opto-mechanical resonator a more challenging work with respect to the development of a control system already successfully used in GW interferometers, such as Virgo. Moreover, the logic of the global control must be designed also with particular regards to the compatibility with the EPR squeezing experiment setup, which is also under development at the R&D squeezing laboratory at 1500W of EGO, Virgo site, as better explained in section 3.3. As a ponderomotive squeezer, with this choice of optical and mechanical parameters for the design of SIPS setup, we can set the cavity detuning at $\delta = 0.3$ to obtain an optical spring frequency of $\Theta = 2\pi$ kHz and an ideal squeezing factor $\xi = 18$ dB (a real squeezing factor as been estimated as $\xi \sim 7$dB if optical losses are considered for described the setup design).

3.3 SIPS integration with EPR experiment

Currently, INFN is working on a table-top experiment for the generation of frequency dependent squeezed state based on EPR (Einstein Podolosky Rosen's paradox) quantum entanglement [12], until now only theoretically demonstrated and never experimentally observed in the range of frequencies of interest for GW detectors. EPR squeezing functioning has been already demonstrated with linear optical cavities [70, 71], but its functioning has not yet been tested when injected into a Michelson interferometer with suspended Fabry-Perot cavities. For this reason, as anticipated in Chapter 2, a promising short-term application of the SIPS interferometer, which is characterized by optical cavities sensitive to the quantum effect of radiation pressure, is its integration with the setup for testing the EPR squeezing technique [12, 62]. This makes very innovative and challenging the integration of the EPR squeezing in SIPS interferometer. The preliminary EPR table-top experiment is under construction in the squeezing R&D laboratory at the EGO-Virgo site, being carried out by many INFN Italian research groups and Universities, together with some members from the French CNRS. Moreover, a collaboration with a research group from the Korea Astronomy and Space Science Institute (KASI) started in 2019. At present, the KASI team is actively involved in the design of the IR Mode Cleaner cavities for the EPR setup and for the mode-matching reflective telescopes needed for optimising the coupling of the squeezed light with a Test Cavity and SIPS interferometer. According to the original scheme proposed for the EPR experiment, the squeezed light fields (signal and idler) generated by a degenerate OPO cavity are injected into a linear test cavity, which will convert it into FDS light. The test cavity is designed to be resonant at the signal frequency ω_0 while it is detuned with respect to the idler beam.

Although SIPS was designed for exploiting the ponderomotive effect for generation of FDS, since 2019 it has been chosen for the ambitious goal to be used as a test bench for the detection of EPR FDS light, thus for the first demonstration of the advanced EPR squeezing technique inside a Michelson interferometer with Fabry-Perot cavities, before the integration in a real GW interferometer, such as Virgo. The computation of the expected noise budget of SIPS, shown in [62], was carried out adopting a conservative approach, by considering the seismic noise at the R&D squeezing facility at Virgo site as seen by the double-stage suspended mirror and it suggests that even without the use of a superattenuator, SIPS interferometer can be successfully used as a test bench for the EPR experiment. Indeed, in the current year SIPS will be moved to the EGO squeezing laboratory in order to integrate it with the EPR optical set up, which is under development. This plan foreseen a modification of the EPR setup, in order to include a mode matching telescope to inject the EPR squeezing beams into the dark port of SIPS interferometer, while it is operating in dark fringe condition. Moreover, the design of the integration must be optimized to reduce the losses between the OPO that generates the EPR squeezed beams and SIPS. A simplified scheme of the possible implementation of this project is shown in figure 3.12.

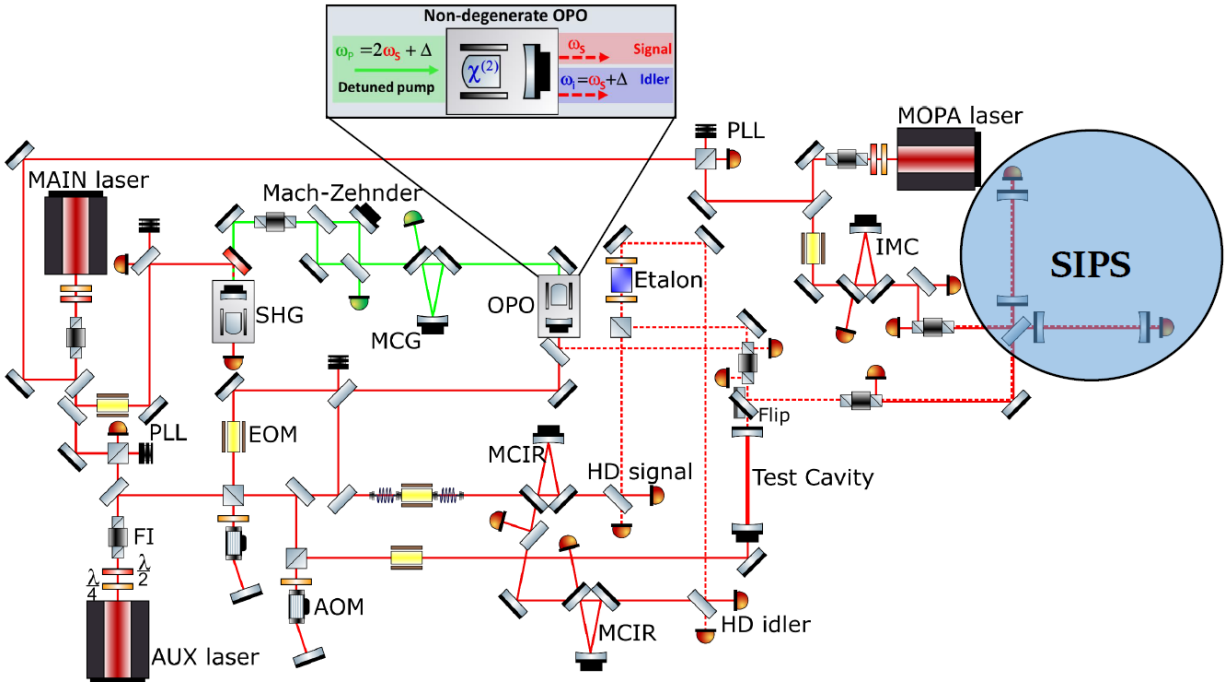

Figure 3.12: Conceptual design of integration of the optical bench of the EPR squeezing table-top experiment with the SIPS interferometer. The entire setup is under construction in the R&D squeezing laboratory at the EGO-Virgo site. See [69] for a more detailed description of the optical elements in the set up.

In the configuration proposed for the integrated design, the EPR signal field has the same frequency of the laser light injected in the interferometer SIPS (coming from a MOPA laser), therefore it is resonant in the Fabry-Perot arm cavities, while the EPR idler beam is slightly detuned and sees the interferometer as a filter cavity which rotates the squeezing ellipse. The two beams are then separated by an Etalon cavity before being detected by two balanced homodyne detectors, providing two signals that are finally electronically recombined to perform a conditional FDS on the EPR signal beam. This mechanism allows to obtain a squeezing factor just below that obtainable by injecting a field of squeezed light in pure phase (frequency independent), but it has the great advantage of extending the gain in sensitivity in all the frequency range of interest of GW interferometers.

SIPS and EPR setups are growing up in parallel and their integration is expected in 2023. The work required to exploit SIPS as a test interferometer for EPR squeezing technique, thus for the integration of the two experimental setup, can be divided into the following steps:

- preparation of the R&D EPR squeezing laboratory at EGO to host SIPS experiment and installation of SIPS vacuum chamber, including assembly and integration of all optical components of EPR setup.
- assembly of the new marionettes for the mini-payloads of SIPS, realized after the study on optimization of the design for suspension system done and described in this thesis

- implementation of an improved local control system on all mini-payloads: starting from the initial tests done on LabView code for local control already implemented, an auto-alignment system will be designed to improve these results [30]
- finalization of the mechanical design to host the optics needed for the interface between SIPS and EPR optical bench
- transportation of SIPS setup from Rome to R&D squeezing laboratory at EGO
- SIPS integration to EPR setup with the assembly of the new monolithic suspensions
- EPR squeezing production, measurements and injection into SIPS for validation of this technique.

A fundamental stage will be also the realization of global control based on the analytical model developed in Chapter 5 and its implementation on SIPS, taking into account the optical and mechanical properties of the system. In this way, it will be possible to realize the locking of all the Fabry-Perot cavities, which means keeping in place all the mirrors of the cavities to ensure the laser resonance condition inside them, and to reach the optimal working point. For this application, SIPS working point can be considered as in dark fringe condition, which is the case of GW interferometers. When integrated with the EPR setup, SIPS interferometer can assure a quantum radiation pressure limited bandwidth of (40 - 700) Hz, thus allowing to observe the frequency-dependent squeezing in a wide range of frequency, coincident with those of GW interferometers. Therefore, this integration would be an important test for the functioning of both SIPS experiment and EPR principle for the reduction of quantum noise in audio frequency band, before a future integration in GW detectors [30]. Furthermore, this technique greatly reduces the optical losses associated with the EPR optical cavity (i.e. the interferometer itself) compared to those typically found in a conventional filter cavity for the production of frequency-dependent squeezing [40].

Chapter 4

Local control of suspended elements

To carry out the SIPS experiment and achieve its scientific goal, it is essential to realize the control of all the main suspended optics, as well as define the strategy for the global control of the entire suspended interferometer. The local control has been developed and tested on a single mini-payload with a dummy mirror, corresponding to the 1 inch diameter end-mirror. In a preliminary stage, the mirror has been suspended using a configuration with two wires, according to the analysis already done in [57]. As will be explained in section 4.2, the preliminary test of local control on the dummy end mirror, gave results that show the need for an improvement of the mechanical design of the suspension system for the mini-payload. The new design foresees to suspend the mirrors with four SiO_2 fibers (2 for each side of the mirror) rather than only two fibers as previously established from [57]. This new design is one of the main results of this PhD thesis work. The detailed study carried out to find the new optimized suspension configuration started in July 2021 and took several months, and the production of the new mechanical elements took one year, mostly due to Covid-19 pandemic, which affected both the production company on the availability of manpower and on the procurement of the raw materials to be machined. Therefore, we only received the new mechanics in November 2022. The new mechanical component for one end mini-payload has been assembled in December and it is currently under test (see section 4.2). Once improved and tested, local control will be implemented also on the mini-payload with the 3 inches diameter dummy mirror, and then on each mini-payload of SIPS interferometer. A LabView-based feedback loop has been designed to damp and control the position of each suspended elements, by means of optical lever read-out system and coil-magnet actuators. In parallel, the global control system of the entire SIPS interferometer must be developed and carefully designed first from the theoretical point of view. Then, in the next development it is foreseen to validated this system, using a prototype with test suspensions, before being integrated into SIPS with the high-finesse and monolithically suspended optics.

4.1 Local control digital system

The optical local control system based upon optical levers has been designed in Virgo, with the aim to damp the angular and longitudinal modes of the suspended

mirrors and to drive their pre-alignment towards the operation setpoint . For the design, inspiration has been taken from the solution adopted for the Virgo last-stage-suspension control system [72]. This active control system allows to perform the alignment and damping of mirror suspension resonance peaks by using the error signals acquired from ground-based sensors and the actuation force applied on the mirror suspension (i.e. internal-force action), with the aim of setting and recovering the reference angular position of each mirror, keeping the interferometer aligned within the accuracy range required to lock the operation point. The mirror angular and longitudinal motions are controlled both acting at the mirror and the marionette levels, with a system based on Virgo local control solution [72]. In the following, we describe the features of the experimental setup used to perform the tests on the local control for the end mini-payload of SIPS. A simplified scheme of this setup is shown in figure 4.1.

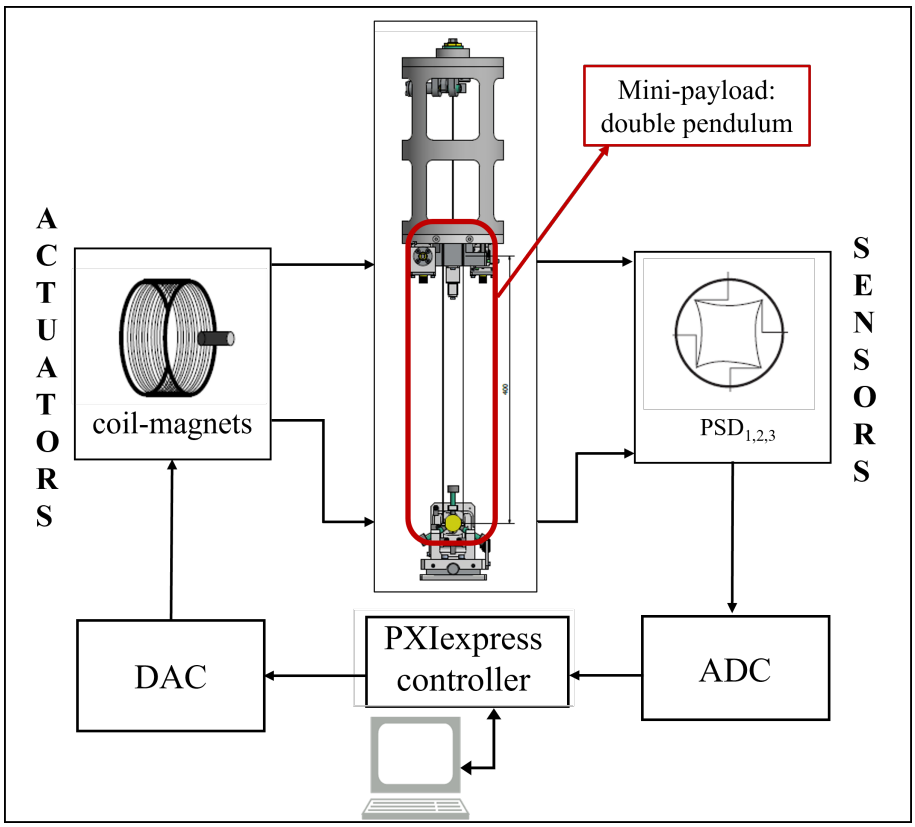

Figure 4.1: Logic scheme of the experimental setup for local control tests: the mechanical system is the end mini-payload of SIPS ITF and is monitored by three position-sensitive detectors ($PSD_{1,2,3}$). Signals from the sensors pass through an ADC and are processed by a PCI-based express embedded controller (PXI-express), allowing the construction of the desired feedback signals which are sent to the actuators through a DAC. The PXIe provides also the excitation signals (white noise) in the transfer function measurements.

It can be divided into four logical block:

- **mechanical system**: SIPS end mini-payload, with a double pendulum configuration;

- **readout system/sensors**: 3 displacement sensors to monitor both mirror and marionette motion;

- **actuators**: four coil-magnet actuators placed on both mirror and marionette for positioning and active control;

- **electronics**: it includes the sensors readout, the ADC and DAC boards, and a PXI-express controller.

4.1.1 Mechanical system

As already explained, SIPS has been designed to be dominated by the radiation pressure noise (RPN), thus being in the RPN-limited regime all over the whole frequency band of GW detectors. The sensitivity of an interferometer, such as SIPS is limited, among other noise sources, by the seismic background, which causes fluctuations of the mirror position, as already mentioned in section 3.2.1. The solution of suspending the optical components is a simple way to limit the unwanted displacements of the mirror, thus filtering the ground vibrations. In this way, for frequencies above the resonant frequency of the pendulum formed by the suspended mass, the mirror can be considered as "free falling". For the specific purpose of testing local control, one end mini-payload has been chosen. As introduced in section 3.2.3, this is composed by the *Marionette*, the suspension wires, and the mirror. The marionette is the last stage of suspension, supporting the mirror. It has been designed for steering and alignment of the optical components, mirrors, and BS, in order to ensure the desired working point, thus allowing the final step of interferometer locking. It is essentially a rectangular structure suspended to the upper plate of SIPS through a steel (C85) wire 30 cm long, and it has a weight of about 1.150 kg. The original marionette mechanical drawing, with some information on dimensions, is shown in figure 4.2. On the marionette, four magnets are attached, through which forces applied by the coils allow fine control of the mirror on the three relevant degrees of freedom: the mirror rotations around its horizontal and vertical axis and the translation along the beam direction. The mirror is the main optical component of the interferometer that must be controlled. For the preliminary tests, the prototype "dummy" end mirror used is a cylinder made of aluminum having the same dimension of the real end mirror (1 inch diameter and 10 mm thickness) where a small cylindrical groove has been done to host a smaller mirror (diam $\sim$ 5mm) used for the optical lever. In addition, a 60 μm groove has been realised in the middle of the circumference for ease the gluing of the suspension wire. This solution has been adopted to operate the local control in a mechanical configuration similar to the final design, providing the overall weight and dimensions (1 inch) of SIPS end mirror. Small corrections may be applied directly on the mirror from four coils mounted on a mechanical holder, shown in figure 4.3, which has been designed also to support the mirror during the assembly of the suspension.

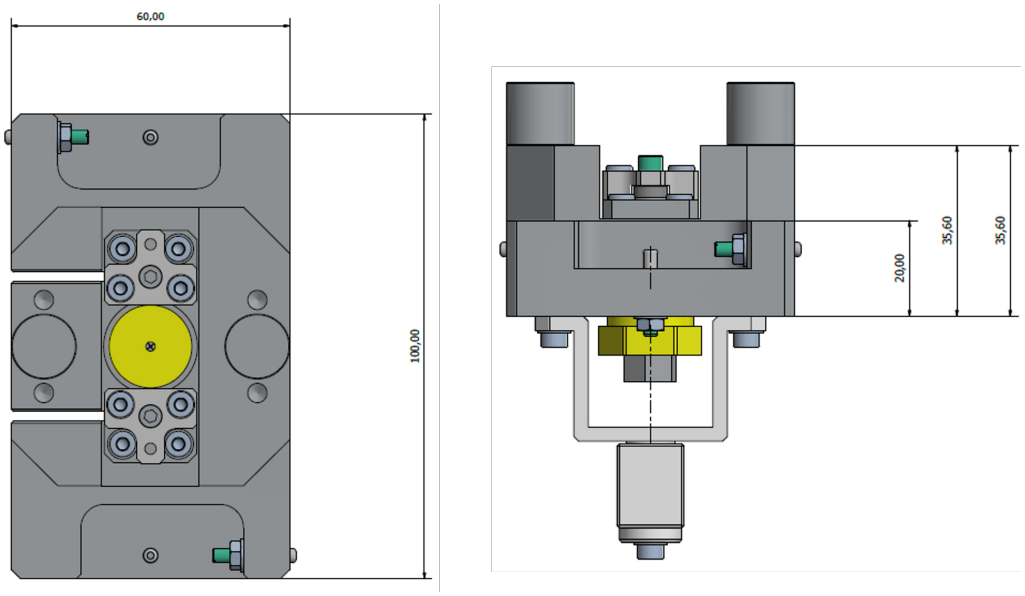

Figure 4.2: Mechanical drawings of SIPS end payload marionette: on the left the marionette top view is represented, while a side view is shown on the right, with the mechanical support which holds the reflector needed for the optical lever system for the readout of local control.

4.1.2 Readout system

The error signals for the local control are obtained using a ground-based readout system. It provides information about longitudinal and angular local position of the suspended mirror and also the angular one of the marionette, making use of two *optical levers* setup, at both mirror and marionette level [73]. The scheme of position measurement is designed to provide the error signals and takes inspiration from the one used for tests on Virgo local control system [65], this is shown in figure 4.5. The beam is generated by a Superluminescent diode (SLED) with a wavelength $\lambda_{SLED} = 633$ nm and it travels through an optical fiber and a collimator, providing ~ 3 mW of output power. This beam is attenuated by passing through an optical filter which gives a final power of about 0.3 mW and then it is sent to center of the suspended mirror. The position of the beam, reflected by the mirror surface, is read by two Position Sensing Detectors (PSD), one placed in the focal plane (PSD_1) and the other in the image plane (PSD_2). These are two-dimensional PSDs (Hamamatsu Photonics S2044), which are opto-electronic position sensors using photodiode surface resistance: continuous output signals, the X/Y coordinate signals, can be obtained for the movement of the light spot, with an excellent position resolution and high spectral response range ($340nm < \lambda < 1060nm$). The PSD photosensitive area is represented by a square with $L_x = L_y = 5.7$ mm and it is illustrated in figure 4.4. Then, given the four photo-currents $I_{X1}, I_{X2}, I_{Y1}, I_{Y2}$, the position conversion formulas for PSD are written as

$$\frac{(I_{X2} + I_{Y1}) - (I_{X1} + I_{Y2})}{I_{X1} + I_{X2} + I_{Y1} + I_{Y2}} = \frac{2x}{L_X} \tag{4.1}$$

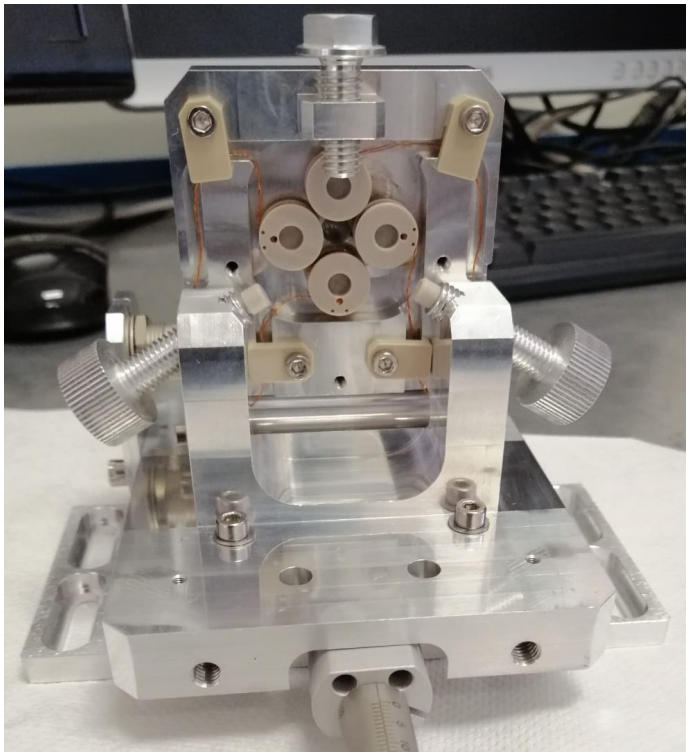

Figure 4.3: Mechanical system used to hold the mirror for assembly operation of the mini-payload suspension, provided with four coils in a cross configuration, for the actuation on the suspended mirror.

$$\frac{(I_{X2} + I_{Y2}) - (I_{X1} + I_{Y1})}{I_{X1} + I_{X2} + I_{Y1} + I_{Y2}} = \frac{2y}{L_Y} \tag{4.2}$$

where x and y gives the position of the light spot on PSD sensitive area and $I_{(X1,X2,X)}$. The full optical path of the optical levers is 42.25 cm for PSD_1 line and 46.25 cm for PSD_2 line: they are the sum of the distance between the SLED and mirror surface, which is 21.25 cm, plus the distances from mirror surface to PSD_1 and PSD_2 respectively.

A second optical lever is used to measure the angular position of the marionette using a small mirror (equal to the one used for the dummy mirror), attached to a dedicated support mounted on the marionette body, called periscope, as shown on the right side of figure 4.7, which reflects the laser light towards PSD_3 placed in the marionette's mirror focal plane. In this way, the light spots on the PSDs are used to reconstruct both the mirror and marionette position: the suitable error signals are reconstructed in a left-handed reference frame with its origin in the mirror center of mass and the z-axis oriented outward as the impinging laser beam, and the same is done for the marionette. This optical levers system allows to control the mirror position along the direction of the laser beam, z, and along the angular degree of freedom.

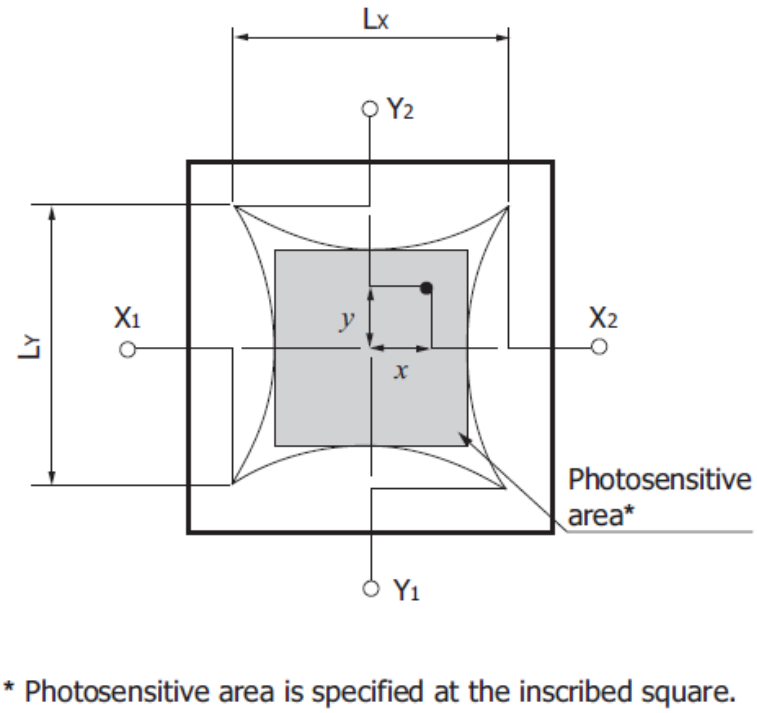

Figure 4.4: Details of the photosensitive area of Hamamatsu two-dimensional PSD S2044. X_1, X_2, Y_1 and Y_2 are the anodes which delimit the photosensitive area where impinging photons are converted in the photocurrent, $I_{X1}, I_{X2}, I_{Y1}, I_{Y2}$.

The following convention is adopted to refer to the three angular degrees of freedom of a mirror [14] (shown in figure 4.6):

- θ_x is the rotation around the horizontal axis in the mirror plane (*pitch*);
- θ_y is the rotation around the vertical axis in the mirror plane (*yaw*);
- θ_z is the rotation around the axis perpendicular to the mirror, (*roll*), which corresponds with the beam axis, conventionally assumed to be z.

Sensing system for the longitudinal and angular degrees of freedom is described in table 4.1. A similar scheme is already successfully used in the context of Virgo [65].

Optical element	Sensor	Controlled DOF
Mirror	PSD_1	θ_x, θ_y
	PSD_2	z
Marionette	PSD_3	θ_y, θ_z

Table 4.1: Specific degrees of freedom (DOF) that can be controlled after the reconstruction of the error signals acquired by PSD_1 and PSD_2 from the mirror reflection and by PSD_3 from the marionette optical lever.

For this preliminary test phase on SIPS, the overall local control position sensing system is located in air (such as the entire SIPS bench) as illustrated in figure 4.7:

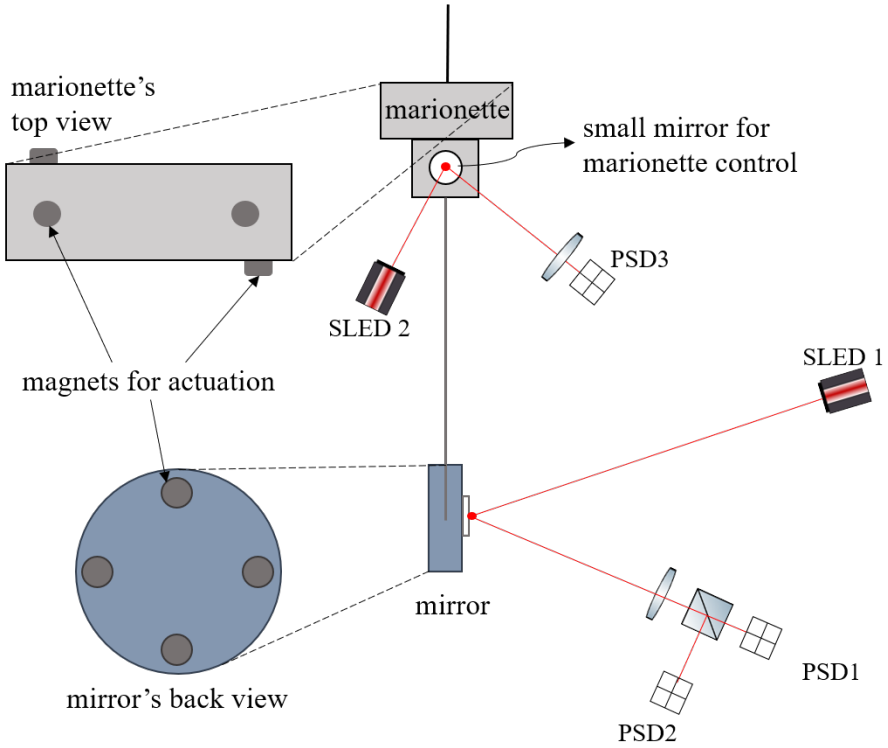

Figure 4.5: Simplified scheme of the readout and actuation systems for one SIPS mini-payload. Four magnets for actuation are placed on both mirror and marionette. Coils are not represented in this scheme for simplicity, but they are located on a mechanical support, behind the mirror, and on the marionette mechanical support. The optical, mechanical and electronic elements are not in scale [30].

PSD_1 and PSD_2, for the position measurements of the mirror, are hosted on the main optical bench, thus rigidly fixed at the base of the vacuum chamber; PSD_3, which senses the position of marionette is instead located on a customized small optical bench, rigidly fixed at the upper auxiliary bench. In this setup for the local control test the vibration from the outside environment, i.e. seismic noise, can be considered negligible, according to the analysis done in [62], already presented in section 3.2.3. Therefore, this test setup can be exploited for the first use of SIPS as EPR squeezing tester, while, for the final aim of SIPS to be exploited as ponderomotive squeezer, some modification must be done to filter seismic noise. Indeed, as discussed in section 3.2.3, the entire bench setup will be suspended to the superattenuator, (SAFE), allowing the entire setup, including optical levers for sensing, to be properly isolated by seismic vibration.

4.1.3 Actuators

For the actuation system, the end mirror is provided with a set of four small cylindrical magnets (1.5 mm diameter $\times$ 1.5 mm thick), glued to the back face of the mirror in a cross configuration, as visible in the pictures of figure 4.8, and placed in correspondence to the four coils mounted on the mechanical holder shown in figure 4.3. By controlling the current flowing through these coils (better explained in the

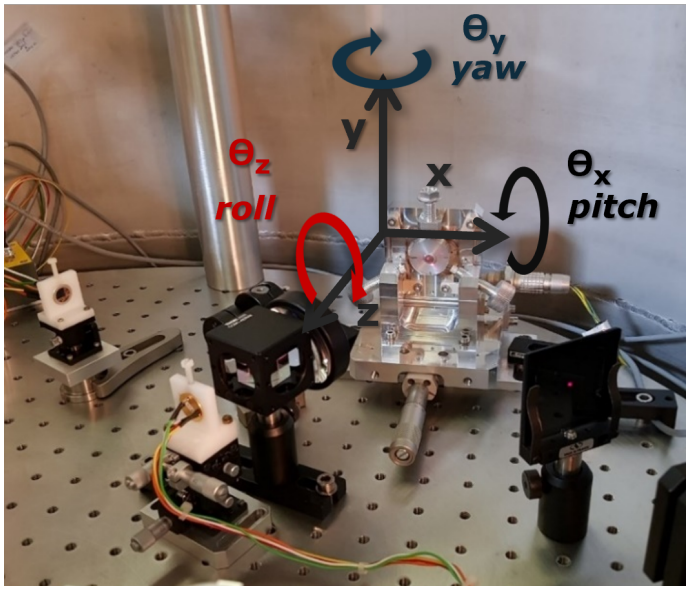

Figure 4.6: Picture of SIPS end mirror used for preliminary tests, with the identification of the three axes and the three angular degrees of freedom of the suspended mirror, according to the convention adopted also in Virgo [14]

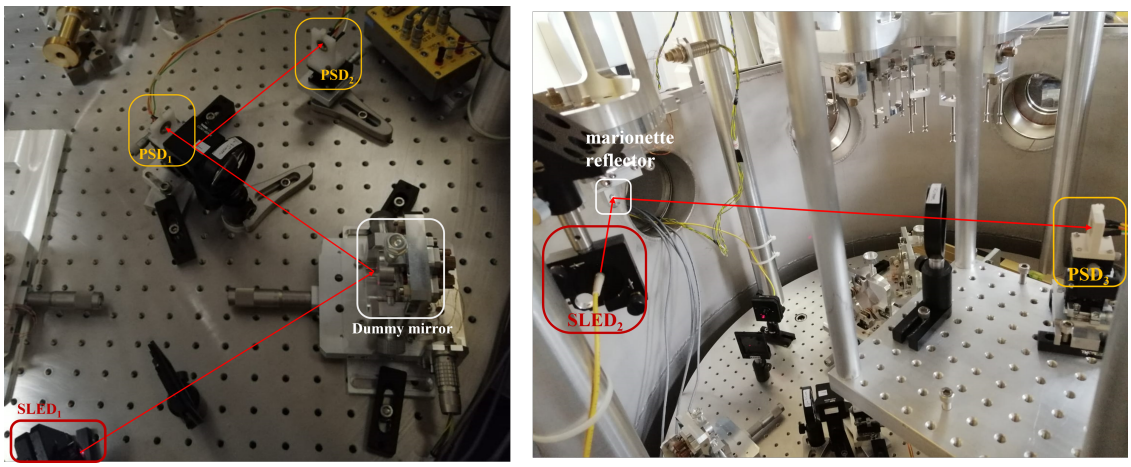

Figure 4.7: Optical levers setup for SIPS end mini-payload: the pictures show the two setups installed on both mirror (left) and marionette (right).

next two subsections) it is possible to apply longitudinal and torsional forces to the mirror: forces applied on suspended masses are related to the current flowing in the coil. As shown in figure 4.9 for the coils placed behind the end mirror, the maximum distance between the center of the coil and the center of the magnet, at which the actuation force of the coils has a linear trend, is about 3 mm. The marionette is provided with other four magnets, glued to marionette body in the configuration shown in figure 4.5, to be in correspondence to four coils that are mounted on the lower plate of a mechanical "cage" rigidly connected to the upper auxiliary bench. Any current applied to these coils results in a force on the marionette, which is thus transmitted by the last pendulum stage to the suspended mirror. This coil-magnet system then provides the control actuation for both marionette and mirror. Coils

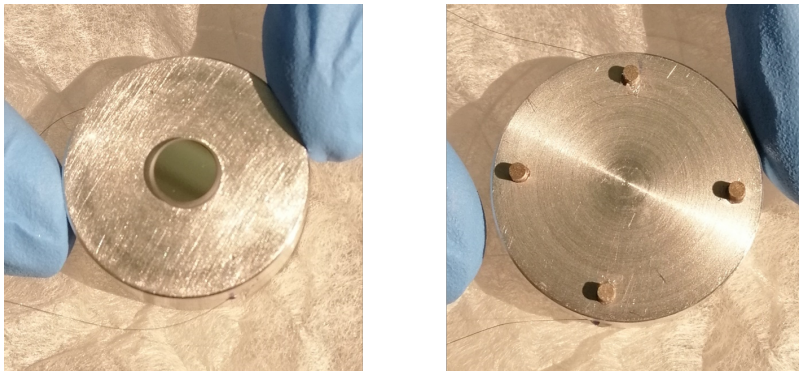

Figure 4.8: Left: front side of the aluminium body where a small mirror is permanently attached, forming the "dummy" mirror used for tests on local control. Right: back side view of the dummy end mirror with four magnet glued for coil-magnet actuation system.

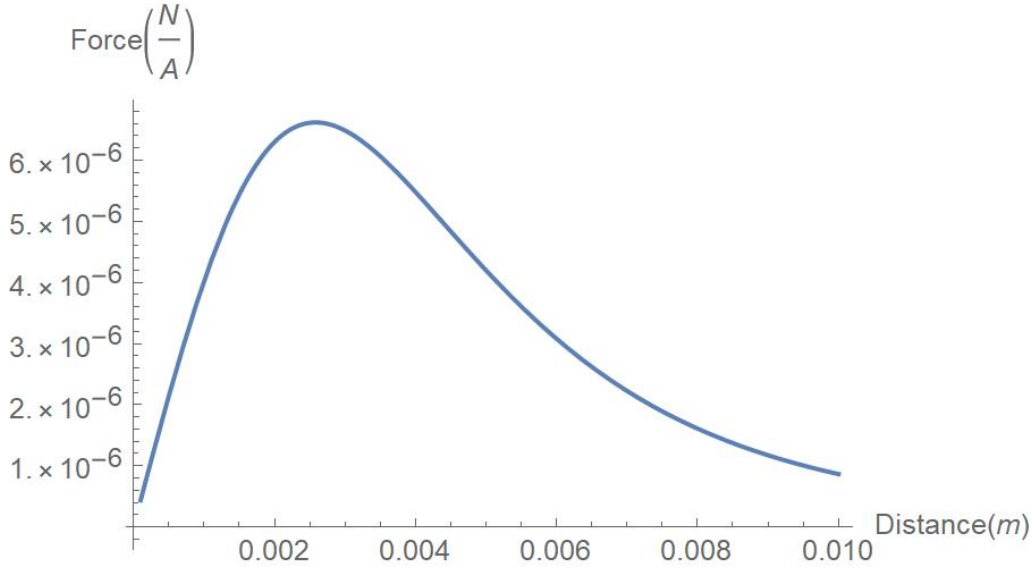

Figure 4.9: Force actuated on the magnet of the end mirror, related to the current flowing in the coil, as a function of the distance between them.

resistance required for the initial design and the related cut-off frequency are shown in table 4.2, while the measured coils resistance and computed cut-off frequency, obtained from the actual experimental setup are shown in table 4.3.
The cut-off frequency, for end mirror and input ones, has been computed using the following formula

$$f_{cut-off} = \frac{R_{(end,input)}}{2\pi L_{end,input}}. \tag{4.3}$$

Here, the inductance L, expressed in μH, is obtained using the approximated formula:

$$L = \frac{0,135 r^2 N^2}{6r + 9l + 10d}, \tag{4.4}$$

where N is coil winding number, l is coil length, r is coil radius and d is the winding depth. These parameters are known for both end mirror and marionette (coils implemented for input mirrors are the same of the marionette ones), thus giving

Coils acting on	R (Ohm)	f_{cutoff} (kHz)
input mirror/marionette	6.34	2
end mirror	3.17	2

Table 4.2: Resistance and cut-off frequency required for the actuation in the initial design.

Coils acting on	R (Ohm)	f_{cutoff} (kHz)
input mirror/marionette	4.5	1.1
end mirror	2.7	3.2

Table 4.3: Resistance and cut-off frequency computed for input and end mirrors of a mini-payload, considering that input mirror and marionette coils have twice as many winding as the end mirror coils.

L_{end}=133.90 μH for the end mirror, and L_{mario}=634.13 μH for the marionette. With these values of inductance, considering the measured values for resistance, R_{end}=2.7 Ω and $R_{marionette}$ = 4.5 Ω, the coils cut-off frequencies are found to be $f_{cut-end}$ = 1.1 kHz and $f_{cut-mario}$ = 3.2 kHz for the end mirror and the marionette, respectively. Even if the actual coils cut-off frequencies are different from the ones estimated in the initial design, direct measurement showed that the amplitude gain drops significantly for f >50 kHz, far from our range of interest, which means that these values are still compatible with the initial design and suitable for both local and global controls [30].

4.1.4 Hardware

All the analog signals extracted from the suspension sensors are first amplified, using customized amplifiers provided by INFN-Napoli, and then acquired by an Analog to Digital Conversion (ADC) board (NI BNC-2111 on the left in figure 4.10), with 12 analog input (AI) channels:

- 4 channels, $AI_{0,1,2,3}$, from PSD_1 on mirror focal plane;
- 4 channels, $AI_{4,5,6,7}$, from PSD_2 on mirror image plane;
- 4 channels, $AI_{8,9,10,11}$, from PSD_3 on marionette focal plane.

The ADC board is connected to a National Instrument Real-Time device (NI PXIe-1082), in particular to PXIe-6363 placed in the slot 2 of PXIe Chassis (see fig. 4.10). Signals are processed in LabView environment: the digital corrections computed by the code are converted by a National Instrument Digital to Analog Conversion (DAC) board, NI SCB68-A (green square in figure 4.10), into a voltage signal suitably amplified and translated into a current flowing in the coil. Even if the ADC board used has a total of 32 AO channels available, the cabling has been done only on 8 analog output channels, used to send analog signals to the actuators on both mirror and marionette: 4 AO channels, $AO_{31,29,27,25}$, for actuation on mirror coils and other 4 AO channels, $AO_{23,21,19,17}$ for marionette's coils. The NI hardware setup,

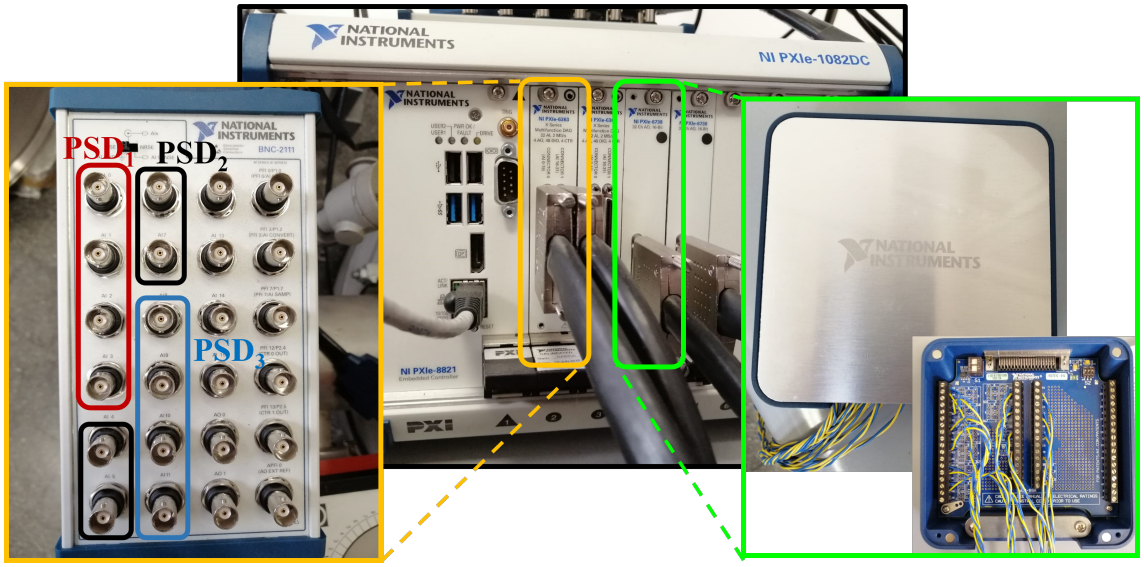

Figure 4.10: National Instrument devices used for real-time acquisition of signal from sensors, signal processing and generation of correction signal for actuation. The Analog to Digital (ADC) board NI-BNC-2111 (orange square on the left) has 16 available channels, 12 of which used for acquisition of signals from $PSD_{1,2,3}$. It is connected to the NI real-time device NI PXIe-1081 (black square), where on the first slot is located the embedded controller NI PXIe-8821, dedicated to processing signals and generating digital correction signals. These digital signals are then sent to the DAC board NI SCB-68A (green square), with 32 AO channels available, 8 of which used for sending actuation signals for the mini-payload.

was chosen to replace a previous one and to be integrated and used for the local control tests, due to the need of higher performances and, in particular, to the need of a higher number of both acquisition and actuation channels. For this technical reason, some preliminary experimental work was carried out for mapping, cabling and testing the electronic connections on the actuation line. The DAC panel SCB-68A has been connected to coils actuator on marionette and mirror by two different cabled 8-pin connectors (the cabling on DAC board is partially shown in the orange square of figure 4.10).

4.1.5 Software: LabView Real-Time system

Signals are processed with the LabView software, dedicated to monitoring tasks and real-time operations for analysis of PSDs data and feedback cancellation, thus providing error and actuation signals. The used real-time system consists of software and hardware components. The software components include LabView, the Real Time (RT) Engine, and the LabView projects and VIs we created. The hardware components of a real-time system include a host computer and an RT target (see section 4.1.4). The host computer is provided with LabView software and the LabView Real-Time Module installed on it. We develop and run the VIs (the code) for the real-time system on the host computer, which communicate with a networked RT Series device through an Ethernet connection, thus providing a user interface:

the Real-Time Module extends the capabilities of LabView with additional tools for creating, debugging, and deploying the VIs. We used an RT target of a networked RT Series hardware, which is a networked hardware platform with an embedded processor and a real-time operating system (RTOS) designed to run only the VIs and device drivers necessary for RT applications. The one we used, and already mentioned in the previous section, is a PXI Controller (PXIe-8821), a networked device installed in an NI PXI chassis (PXIe-1082DC) that communicates with NI PXI modules installed in the chassis, i.e. the two modules installed in slot 2 (PXIe-6363) and slot 4 (PXIe-6738) on the chassis in figure 4.10. The controller is provided with *RT Engine*, which is a version of LabView that runs on a RTOS, also supporting features of the RT Series PXI controller. This allows to write LabView codes using all the input/output (I/O) capabilities of the PXI modules, providing deterministic real-time performance. LabView software allows to implement the digital control loops, which includes the logic and the control filters. It also allows to inject noise for measuring the frequency response of the suspended mirror. The code written in a LabView VI has a readout part, which makes the computation of error signals of mirror and marionette DOFs, Θ_x, Θ_y, Θ_z and z: the signals from sensors are acquired using the NI DAQmx acquisition system, which manage the reading of analog signals from the 12 AI Channels, as already explained in section 4.1.4. These signals are then processed to compute the error signals, obtained by implementing a simple computation of horizontal and vertical displacements of the light spot on the photosensitive are of the three PSDs. The variations along the two coordinates of the PSD are given by:

$$\frac{(UR+DR)-(DL+UL)}{UL+UR+DL+DR} = A_x \tag{4.5}$$

for the horizontal displacement, A_x, and

$$\frac{(UL+UR)-(DL+DR)}{UL+UR+DL+DR} = A_y \tag{4.6}$$

for the vertical displacement, A_y. Here, UL, UR, DL and DR are the four vectors (4 voltage signals) representing the up-left, up-right, down-left and down-right sectors of the photodiode surface respectively. The voltage signals given in UL, UR, DL, DR vectors are the result of the impinging of the light spot on the pothosensitive area of the PSD, which corresponds to an area of $\sim 5,5$ mm^2. We acquire 3 sets of this four signals, for the three different PSDs of the read-out system, as shown in table 4.4. This allows to compute the error signal related to mirror and marionette DOFs. The correction filters implemented in the LabView code, filter these signals and then, two driving matrix, for both mirror and marionette, allow to generate the digital correction signals for the actuation: signals from 8 AO channels are first sent to the DAC board (NI SCB68-A) and finally sent to the coil for actuation.

Sensor	Signal	AI channel	output
PSD_1	UL	AI_0	
	UR	AI_1	$A_x = \theta_y$ (mirror)
	DL	AI_2	
	DR	AI_3	$A_y = \theta_x$(mirror)
PSD_2	UL	AI_4	
	UR	AI_5	
	DL	AI_6	z
	DR	AI_7	
PSD_3	UL	AI_8	
	UR	AI_9	$A_x = \theta_y$ (marionette)
	DL	AI_{10}	
	DR	AI_{11}	$A_y = \theta_z$ (marionette)

Table 4.4: List of AI channels and associated signals from which output error signals, representing mirror and marionette longitudinal motion and angular tilt, are computed. A_x and A_y are the horizontal and vertical displacement given in equations 4.5 and 4.6.

4.1.6 Mirror mechanical Transfer Functions

Since the main duty of the designed local control system is to perform alignments of suspended optics, in order to be effective, the system has to control the DC position of the mirrors and damp its modes in the two angular DOF: θ_x ($pitch$) and θ_y (yaw) (see fig. 4.6). In order to study the frequency response of the double pendulum system used for tests, the transfer functions of dummy end mirror DOFs have been measured. Taking inspiration from the scheme of control used for Virgo (multistage suspension system [21]), the angular corrections should be applied, in our case, on two actuation point: at the level of the mirror and at the level of the mass from which the mirror is suspended, that is the marionette. One advantage of this solution is that the local control actuator noise at mirror level is filtered by another stage of suspension, represented by the marionette, also at the cost of a narrower control bandwidth [65]. Our first step was to characterize the frequency response of the double pendulum system, in order to optimize the design of the corrector filter. The measurement of the mechanical transfer functions of the system are illustrated in figures 4.11,4.12 and 4.13. This measurements has been obtained by sending an external disturbance only at the mirror level, by means of a LabView code developed on purpose for the generation of white noise: this has been set on 60 mV, with a sampling frequency of 1 kHz. Then, the motion is sensed at the mirror level, using PSD1 to obtain yaw and pitch modes, and PSD2 to extract information about the pendulum frequencies (from the displacement along z axis). LabView code allows to compute both magnitude and phase for pitch, yaw and z-pendulum modes. Moreover, the analysis of the transfer functions allows to extract information from their structures: the number of modes present in the TF is relevant for the optimization of the design of the digital filters for the generation of the actuation signals [65].

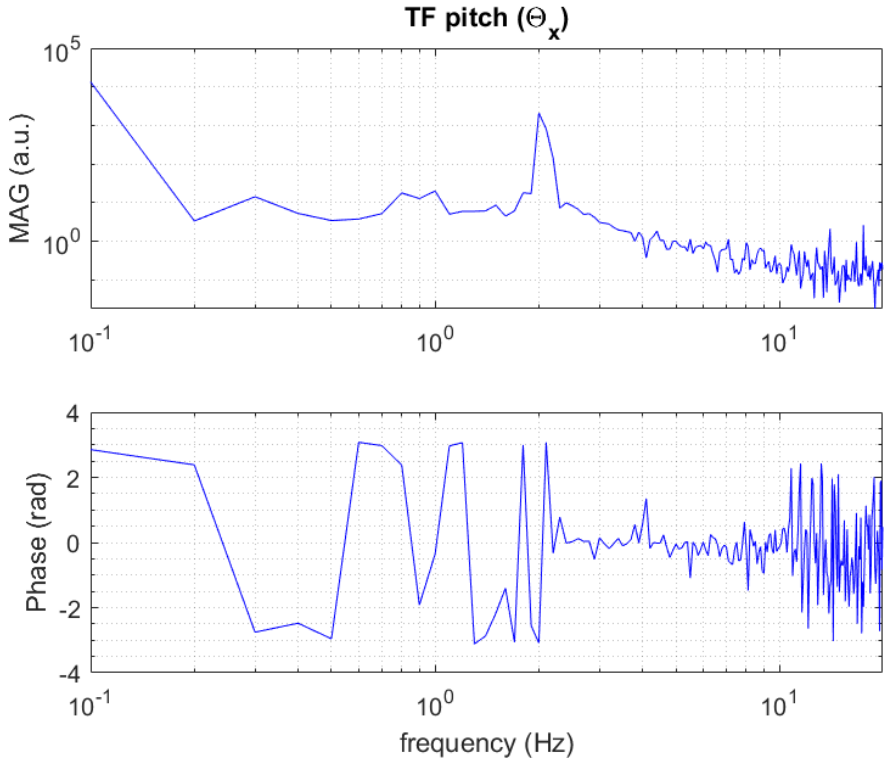

Figure 4.11: Magnitude and phase of torque-to-angle transfer function of the pitch mode for the SIPS dummy end mirror.

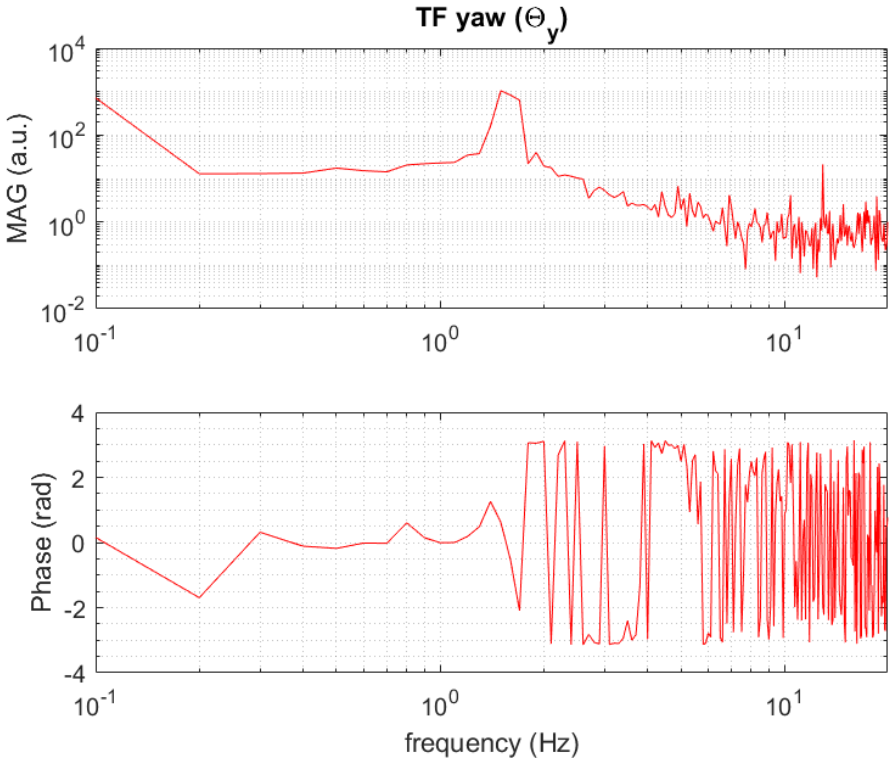

Figure 4.12: Torque-to-angle transfer function (magnitude and phase) of the yaw mode for SIPS dummy end mirror.

The yaw DOF in figure 4.12 is characterized by one relevant resonance at a frequency

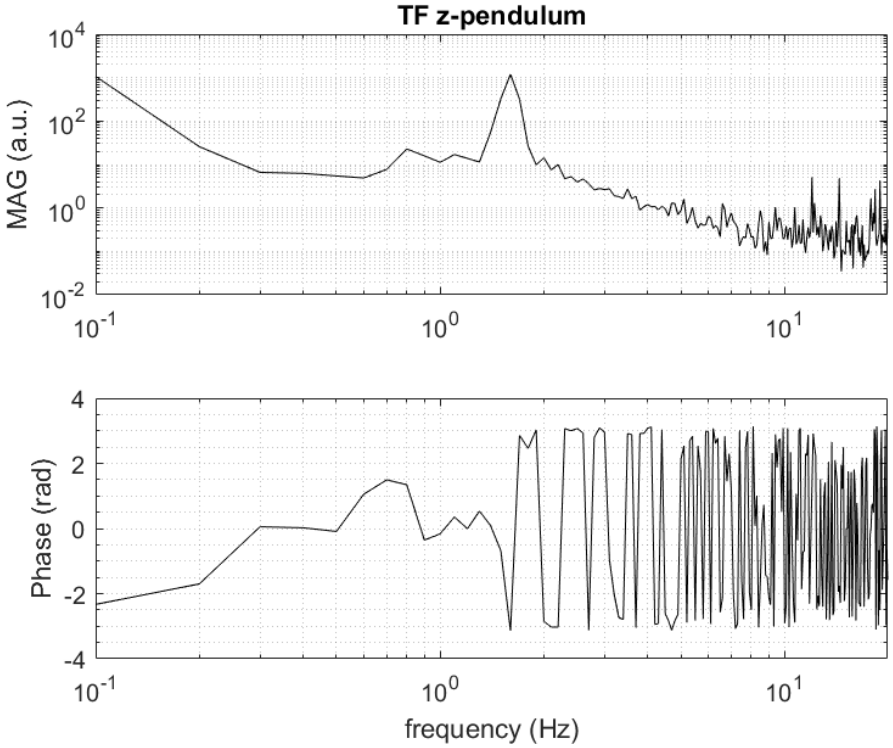

Figure 4.13: Magnitude and phase relative to transfer function of the z pendulum mode for the dummy end mirror.

of about 1.5 Hz: this can be related to internal mode of the payload, explained by a torsional motion of the mirror, in opposition of phase with the marionette motion. Moreover, in figure 4.11, the pitch DOF presents a visible resonance at about 2 Hz. By comparing this with the yaw mode, it seems that the pitch DOF is more excited with respect the yaw mode (for the same excitation noise level). This can bring some unexpected instability and it can be linked to a basic structural problem of the suspension system. Indeed, in the configuration used for this measurements, the mirror was suspended to the marionette by means of only two suspension wires. This is one of the reasons that led us to improve the mechanical design of the suspension system, as will be better explained in section 4.2. The frequencies of the double pendulum system of SIPS mini payload can be computed using the analytical model of sequential pendulums [57]. The analytical coupled pendulum-modes peaks are expected to be at frequencies $f_1 = 0.79$ Hz and $f_2 = 0.91$ Hz. Moreover, from the power spectrum computed with LabView, it has been possible to extract the coupled pendulum frequencies, which has been found to be 0.775 Hz and 0.925 Hz. In particular, from figure 4.13, two resonance can be identified at about 0.85 Hz and 1.55 Hz, when the system is excited by the already defined external disturbance (white noise). The last characteristic shown in this plot is that all the mechanical transfer functions measured show the typical asymptotic behavior, with a slope f^{-4} after the resonances, as it is expected for a double pendulum system.

4.1.7 Pre-alignment performance

The local control system described here, is designed essentially to perform alignments of suspended optics, without exciting the mechanical modes of the mirror suspension last stage (the marionette), in order to finally set the detector in the interference condition. The mirror position can be controlled either by acting directly on it or by acting on the marionette. Acting on marionette allows to re-allocate part of the control force to higher stage of suspensions, thus reducing control noise at mirror level. As already explained, tests have been carried out on one end mini-payload, before its implementation in all SIPS suspended elements. As a first step, the optical levers system designed, and here described, demonstrates that it is possible to control angular and linear motion of the 1 inch mirror within an accuracy of 10 nrad and 0.1 μm RMS. This constitutes only an initial achievement since we foresee to design an auto-alignment system which will improve this result. Figure 4.14 shows the functioning of the local control for a pre-alignment recovery of the end mirror of one mini-payload. This allows the attenuation of Θ_x, Θ_y and z, while to control the Θ_z degree of freedom, it will be necessary to act also on the marionette, improving in this way the position recovery of the entire mini-payload (see section 4.2). Since the

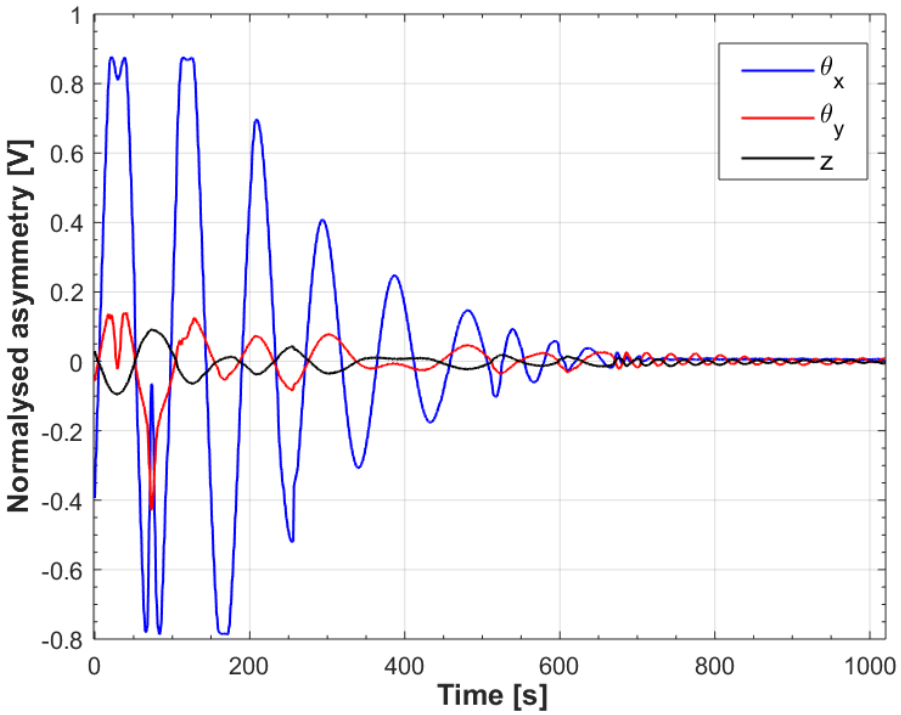

Figure 4.14: Attenuation of the amplitude relative to Θ_x (blue), Θ_y (red) and z (black) oscillations in function of time. The position recovery is done using a low gain control. The control is applied only at mirror stage [30].

local control system has a ground-based readout system, it can not be used when the interferometer is in its working condition, i.e. in dark fringe. For this reason a global control for the locking of the entire interferometer is needed: this is an important topic of this thesis and it has been studied, as discussed in Chapter 5.

4.2 New suspension system

According to the analysis done in [57], a suitable suspension system, composed of a double pendulum with a monolithic suspension was adopted for the SIPS Fabry-Perot cavities, assuring a suspension thermal noise lower than the radiation pressure noise. The mechanical prototype of SIPS has been developed with a double stage suspension configuration, taking into account the experimental feasibility for the fiber production, and assuring a significant clearance between RPN and ThN. The tests on the local control for suspended optics, described in 4.1, allows to obtain the preliminary results for the attenuation on the dummy end mirror, as shown in figure 4.14. Although this results shows an accuracy of 10 nrad and 0.1 μm RMS, the aim is to implement the local control on the entire mini-payload, including the marionette suspension stage. In the attempt to improve the control, acting also on marionette's coils, some problems have been encountered. The first is the instability of the mirror itself, which shows a rotation around the θ_x degree of freedom, probably due to the current suspension system of the mirror with only two suspension wires. Therefore, accordingly to these tests done on the mechanical system, already present at the Physic Department of La Sapienza, we decided that a first step toward the optimization of the control strategy, was to improve the mechanical design of the suspension system. Then it was necessary to investigate a new suspension strategy aiming at an optimized design for the mirror monolithic fibers and suspensions, and for a new shape of marionette allowing the control of all DOFs. This study started in July 2021 and lasted several months, until in the end of the same year an optimized design was achieved. The CAD drawings for the design of the new marionettes have been finalized in October 2021 and, as already mentioned, the manufacturing of new mechanics took more than one year, being finalised only in November 2022. This long delay was due to unavoidable problems related to COVID-19 pandemic, which impacted both on the available manpower of the manufacturing company and on the difficulties in supplying the raw materials to be machined. Finally in December, we could only assemble the new mechanical component for one end mini-payload which is now ready for testing local control.

4.2.1 Monolithic suspension

In order to introduce the new suspension system, it is useful to better describe the previous configuration design, chosen after the analysis previously done on thermal noise [57].

For the monolithic suspension of the optical elements (mirrors and beam splitter) through fused silica fibers, a suitable ear-anchor system and anchor-flat mirror surface silica bonding was developed. The method used was the same developed for the monolithic suspension of the heavy mirrors of Advanced Virgo, adapting this concept to our case. The main differences are first, the mirrors weight, 42 kg in AdVirgo, while 10 g and 300 g for end mirror and input mirror/beam splitter respectively, and the number of fibers used to suspend SIPS optics, which in the original design should be suspended with only two silica fiber instead of the four silica fibers used for Virgo. This is a choice that comes from results of the analysis for the thermal

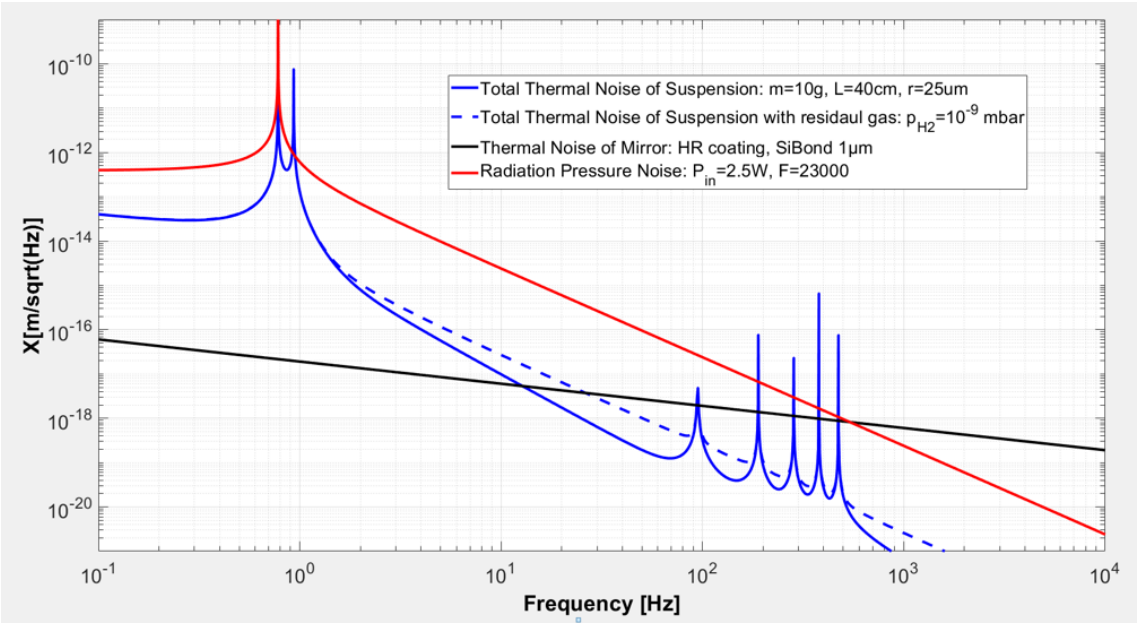

Figure 4.15: Expected noise budget for 1 inch diameter end mirror of 10 g of mass, in the new double suspension configuration with four fibers. Blue curve represents the total suspension thermal noise, the blue-dashed curve represents the total suspension thermal noise and the black curve represents the mirror thermal noise estimated with finite element analysis (the same method used in [57]).

noise dissipation due to the suspensions, shown in figure 3.1. For the new suspension system we decide to adopt four fibers (two for each flat part of the mirrors), as used for Virgo, and also a new geometry for the bonding between mirror and fibers. The geometrical design was finalized in 2021, while the work for the production of the new fibers and the silicate bonding with the mirror is almost finalized. The tests for the production of final fibers are in progress, and some preliminary finite element analysis and simulation (of the same kind done in [57]) was performed to estimate the effect on the mirror thermal noise due to different geometry of the fibers and bonding layers and the presence of two additional wires. The results of this simulation are shown in figure 4.15. The results are very promising, because great effort has been done in improving the geometry of the fused silica suspensions elements in order to reduce the bonding area. Indeed, in the new design with two additional wires, we have decided to remove the presence of additional ears on the mirror, which is possible by silicate-bonding the flat realised at the extremities of the fiber seed directly to the mirror flat sides. This plot (fig. 4.15) demonstrates that, with this new monolithic suspension geometry, we can keep both mirror and suspension thermal noise enough below the radiation pressure fluctuations, which is the fundamental condition to have the radiation pressure noise dominant in the desired frequency range.

4.2.2 New Marionette design

The new configuration, with four suspension fibers led to the need of a new design of the marionettes for the suspension of the main optical elements of SIPS. Figure 4.16 shows the conceptual design of the new end marionette, compared to the original one.

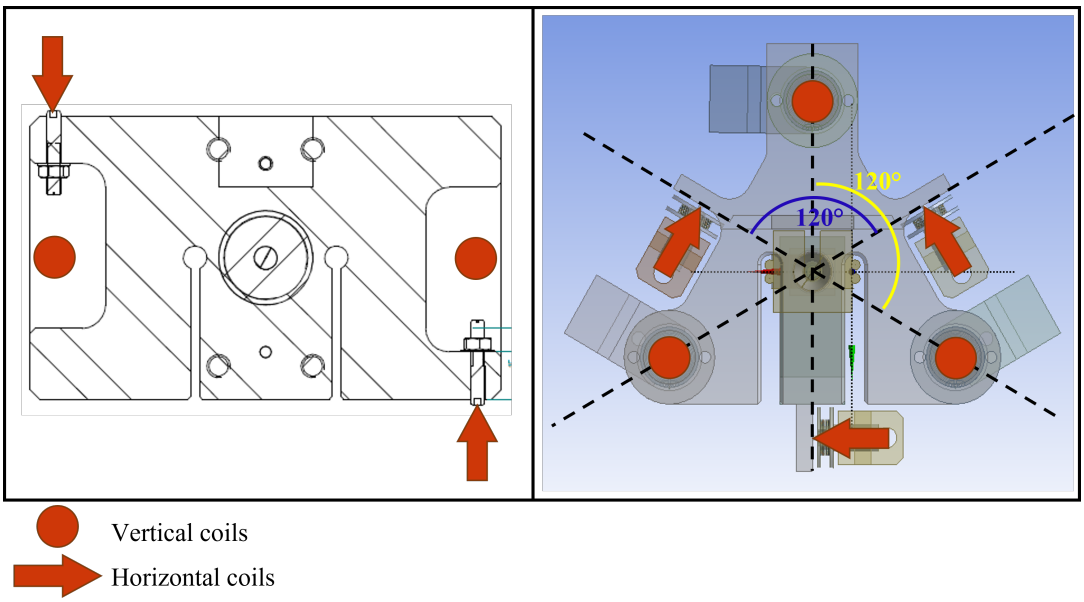

Figure 4.16: Left side: top view of the old design of the marionette for the end mirror mini-payload, with four coil-magnet pairs for the actuation (two vertical and two horizontal). Right side: Top view of the conceptual drawing of new marionette design with six coil-magnet actuators (three vertical and three horizontal) and the SiO_2 C-shape block located at the center of marionette body. The three horizontal coil-magnet pairs are positioned at 120° to ensure the stability to control θ_y; red circles represent the vertical coils (all pointing downwards), while red arrows show the direction and points of application of the forces on the horizontal plane.

The main difference, with respect to the old design is in the shape required by the need to implement two more coil-magnet pairs for the actuation, in order to improve the control of θ_x and θ_y degrees of freedom. In particular, in the top views of figure 4.16, the red circles represent the vertical coils (all pointing downwards), while red arrows show the direction and points of application of the forces on the horizontal plane of the marionette. In the new design, the three horizontal coil-magnet pairs have been chosen to be positioned at 120° with respect to each other, ensuring the stability to control θ_y. The same concept is used for the three vertical coil-magnet pairs, for acting on θ_x degree of freedom. Another important difference is the presence of a SiO_2 C-shape block, which is a component of the new monolithic suspension system (as represented in figure 4.16). This small C-shaped fused silica element is required to attach the flats machined at the extremities of the cylinder seed of the SiO_2 fibers. Two fibers are silicate-bonded on each side of this element, which in turn needs to be bonded to the marionette.

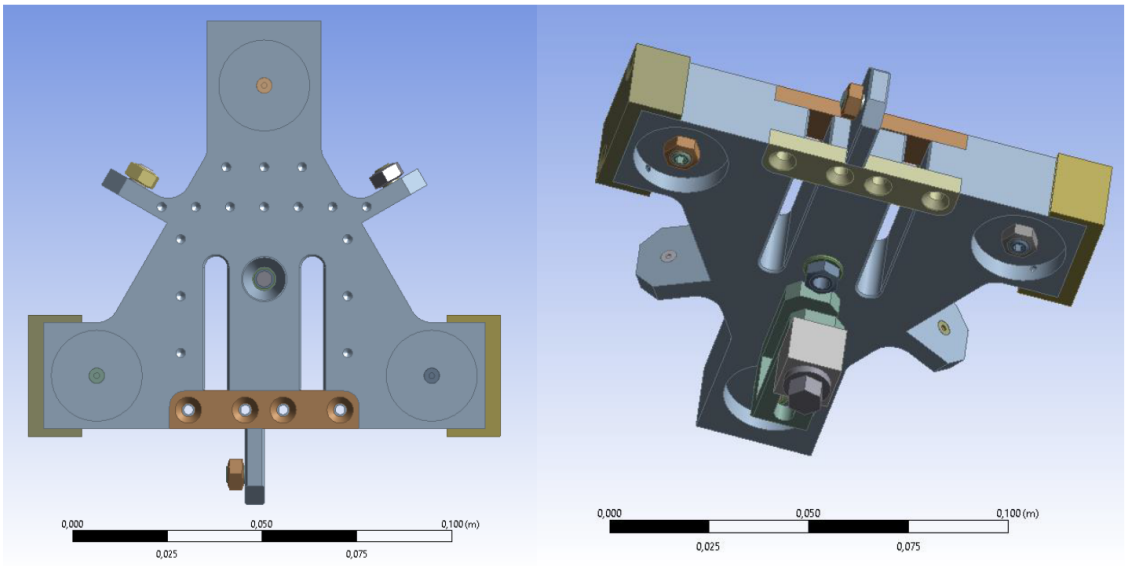

Figure 4.17: Left side: top view of the new design of the marionette for the end mirror mini-payload. Right side: Perspective view from the bottom. Here is visible the periscope element to attach the mirror used for the optical lever of the marionette.

4.2.3 First suspension tests with the new mechanics

In this section, some pictures related to the assembly of the new marionette for the end mirror are depicted. Figure 4.18 shows the new end mirror marionette com-

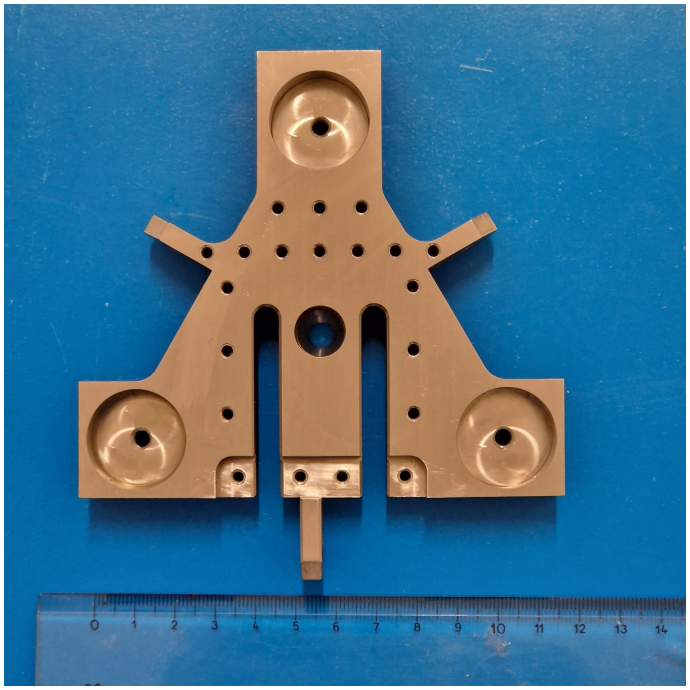

Figure 4.18: The picture shows the new end mirror marionette compared to a ruler, before assembling the suspension.

pared to a ruler, before assembling the suspension of the dummy end mirror. After

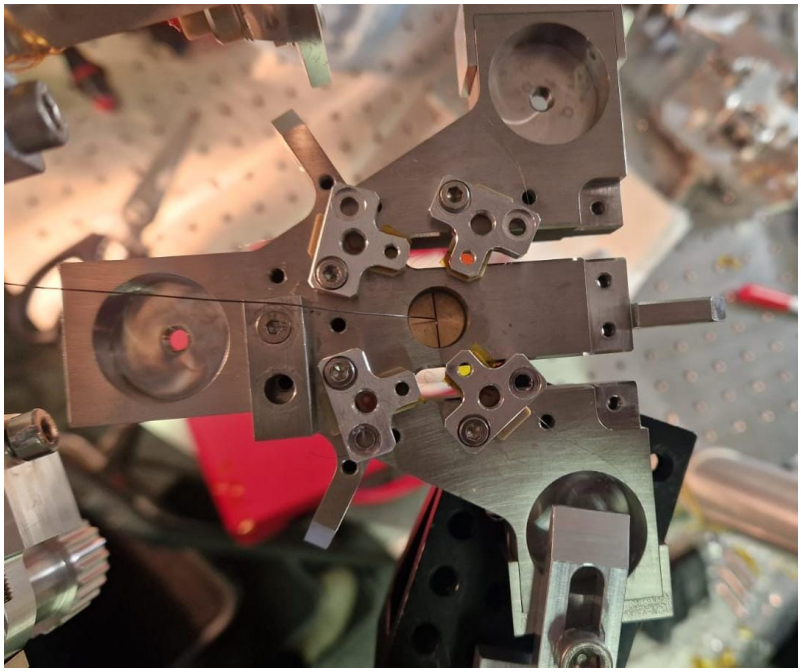

Figure 4.19: This picture shows the new end mirror marionette during the suspension operation.

suspending the marionette to the upper plate, we had to attach the dummy mirror to the marionette with four niobium wires (the same kind of wired used in the first control tests). The marionette has been suspended to the upper plate using only one steel wire, as by design. Some elements, having a T-shape, and taken from the former mechanical design, have been necessary to fix the upper part of the mirror niobium wires to the upper part of the marionette, as visible in figure 4.19. This operation was quite challenging, but in the end we succeeded in suspending the dummy end mirror, as shown in the picture of figure 4.20. Once finalised the delicate phase of suspending the dummy mirror, and having restored all the electronic connections for the coils, the system is ready for testing the performance of the local control with the new upgraded mechanics.

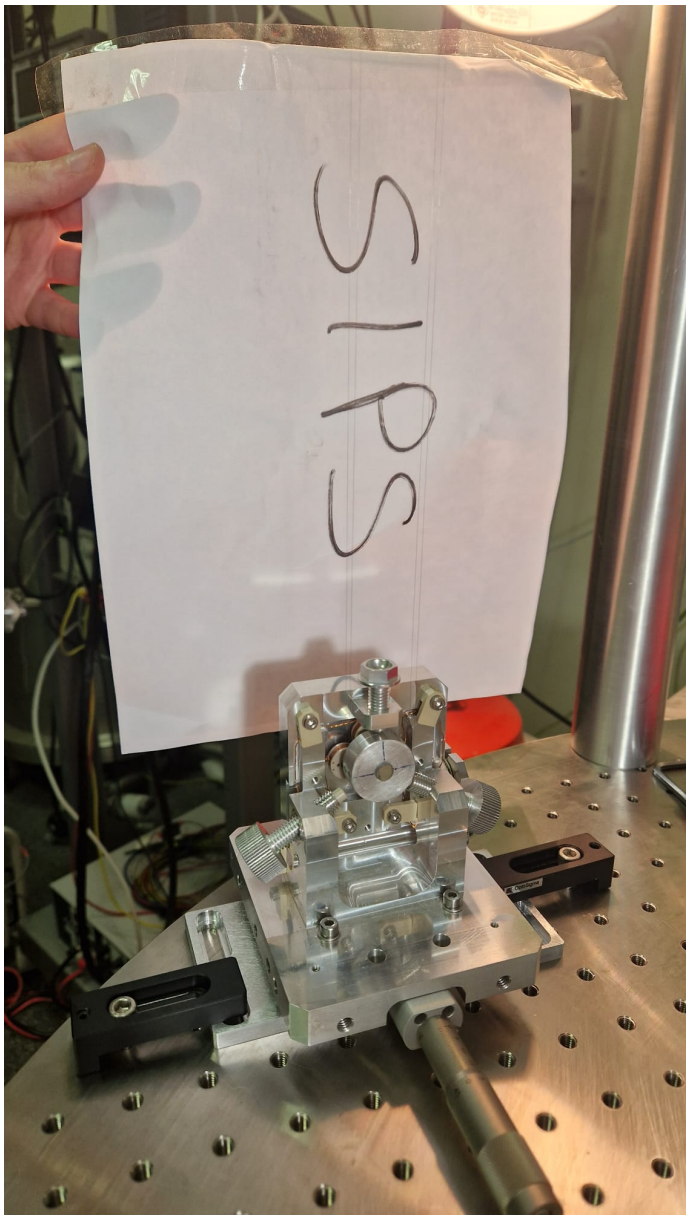

Figure 4.20: The picture shows the new end mirror suspended in December 2022.

Chapter 5

SIPS cavity length control

As mentioned in the previous chapter, the final goal of this research work is the optimization of the control system for a complex physical experiment, such as SIPS. Indeed, even with the local control engaged, the optics would experience a residual motion that brings the interferometer out of its working point. For this reason an active control is needed to act on the optics and keep them on the desired position. Moreover, as already explained, since local control system uses ground as a reference, it can not be used when the ITF is in its working condition (dark fringe), even if it plays a crucial role in damping the mirror oscillations in order to allow the engagement of the longitudinal and angular control. Interferometer active control and feedback loop needs an error signal, coming from photo-detectors to provide permanent information about the position of the optics with respect to the working point, thus to compute the forces that must be applied to the main optics to maintain the correct resonance conditions of Fabry-Perot (FP) cavities. The system devoted to this task is called the **Global** control. According to the system already successfully used in Advanced Virgo, it is first designed considering the FP cavities as a linear optical resonator.

In general, this kind of control operates with the following steps:

i it collects suitable error signals from sensors (the *sensing*);

ii the computed error signal is sent to a controller or *digital filter*, which performs all the needed computation and generate the output correction signal needed to bring the mirrors to their working point;

iii the correction is sent to the appropriate actuators, which are the coils acting on the magnets glued on mirrors and marionettes.

The design of the control filters and the choice of actuators for driving, taking inspiration from the system used for Virgo, is as well a task of the PhD work presented in this thesis.

The design of a global control system for SIPS is a challenging goal, due mostly to the high power circulating inside high finesse ($\mathcal{F}$=23000) Fabry-Perot cavities designed for this experiment. Therefore this control system must be carefully designed,

starting from a theoretical point of view, by initially developing the analytical model for the opto-mechnical interaction inside the FP cavities, which is part of the work done for this thesis and will be described in section 5.3.2. Then, the designed system should be tested on the new prototype with test suspensions before being integrated in SIPS with high finesse optics, monolithically suspended with SiO_2 fibres. For this reason, in parallel, we worked on the design and fabrication of the new mechanics of monolithic suspension (see section 4.2), which has been finalized in November 2022, together with the installation of the new marionette and test suspension system on the end mini-payload for the tests on the designed local control. Some work on both simulation and implementation of the longitudinal and angular loops in the entire SIPS interferometer must be also carried out, in the near future, to finalize the SIPS experiment and test its functioning, before its integration with EPR setup (see section 3.3).

5.1 Fabry-Perot optical resonator

In this section, some basic concepts and general properties of a Fabry-Perot cavity will be discussed, with the aim to present the specific problem of the SIPS Fabry-Perot arm cavities, linked to their opto-mechanical characteristics (see figure 3.9). This will also motivate the choice of the experimental techniques, described in section 5.2 and which can be used as a first solution to bring them to their optimal working point.

5.1.1 Fabry-Perot basic concepts

As already mentioned in Chapter 1, a Fabry-Perot cavity is an optical resonator, consisting of two reflecting mirrors facing each other at a distance L. In the plane wave approximation, the beam entering in an optical system can be described by its complex amplitude and its frequency as:

$$E(t) = E_0 e^{i\omega t}, \tag{5.1}$$

where ω is the frequency of the mail laser (in general expressed ad $f = \omega/2\pi$). If we first consider the beam impinging on a single semi-reflecting mirror [14], its effect can be described by the complex amplitude of the transmitted and reflected fields, written as:

$$E_T = tE_0$$
$$E_R = irE_0$$

where t and r are real amplitude transmission and reflection coefficients. Assuming that the mirror is moving along the x axis, this motion can be defined by the displacement from a fixed reference point (rest position) as $x(t)$. If the variation of the displacement is small in the time the light needs to cover it, which means that the mirror velocity must be much lower than the speed of light, the effect on the reflected field of a moving mirror is a time-varying dephasing and, since this is the

case, we can write the reflected field as:

$$E_R(t) = ire^{2ikx(t)}E_0 \tag{5.2}$$

with $k = \omega/c$. Then, if $|x(t)|/\lambda_L \ll 1$, which means that the displacement of the mirror is smaller than the laser wavelength, we can approximate the previous equation to the first order, i.e. the linear order, as

$$E_R(t) \sim ir[1 + 2ikx(t)]E_0. \tag{5.3}$$

The transfer function of the mirror mechanical motion due to the interaction with the laser field can be computed considering mirror motions, given as

$$x(t) = x_0 \cos(2\pi\omega_x t) = \frac{x_0}{2}(e^{2i\pi\omega_x t} + e^{-2i\pi\omega_x t}). \tag{5.4}$$

Moreover, an optical system can be completely characterized at the linear order, considering an input field simply composed by two components: one oscillating at the main laser frequency ω and one at a frequency shifted as $\omega + \omega_x$. Then, we can compute the transmission coefficients of both components at the output port, taking into account the effect of the perturbation added inside the system (noise). The equation of motion of this system can be expressed using the matrix notation, as an input-output relation, with input and output fields written as bi-dimensional vectors, that is

$$\begin{pmatrix} E_0 \\ E_x \end{pmatrix}_{out} = \mathbf{M} \begin{pmatrix} E_0 \\ E_x \end{pmatrix}_{in}, \tag{5.5}$$

where $\mathbf{M}$ is a 2×2 matrix, which for a moving mirror can be written as

$$\mathbf{M} = ir \left[1 + \begin{pmatrix} 0 & 0 \\ 2ikx_0 & 0 \end{pmatrix} \right]. \tag{5.6}$$

It is also possible to find the propagation over a distance L which, according to the previous consideration, can be defined as

$$\mathbf{P}(L) = \begin{pmatrix} e^{ikL} & 0 \\ 0 & e^{i(k+k_x)L} \end{pmatrix}. \tag{5.7}$$

For a Fabry-Perot cavity with two mirrors having masses m_1 for input one and m_2 for the end one, with reflection coefficients r_1, r_2, transmission coefficients t_1 and t_2, placed at a relative distance L (see Figure 5.1), we can compute the field inside the cavity E_cav, together with the reflected and transmitted fields, E_R and E_T. The first can be expressed in matrix form as [14]

$$E_{Cav} = t_1[1 + r_1 r_2 \mathbf{P}(L)(1 + R_2)\mathbf{P}(L)]^{-1}E_0, \tag{5.8}$$

where R_2 is a matrix operator related to the end mirror, generally defined as

$$R_i = 2ikx_i \begin{pmatrix} 0 & 0 \\ 1 & 0 \end{pmatrix}. \tag{5.9}$$

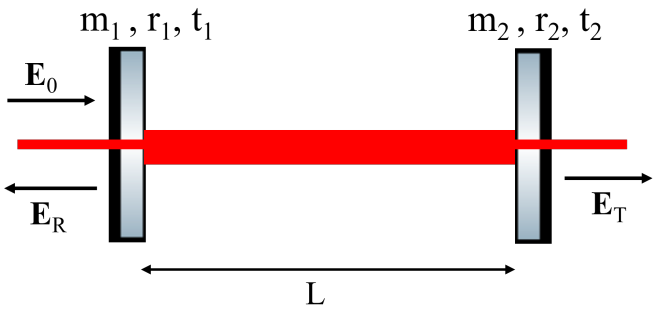

Figure 5.1: Scheme of the Fabry-Perot cavity, with input, reflected, and transmitted fields.

Then, the reflected and transmitted fields are derived:

$$E_R = i[r_1 + r_2 t_1^2 \mathbf{P}(L)(1+R_2)\mathbf{P}(L)\times \\ (1 + r_1 r_2 \mathbf{P}(L)(1+R_2)\mathbf{P}(L))^{-1}]E_0 \tag{5.10}$$

$$E_T = t_1 t_2 \mathbf{P}(L)[1 + r_1 r_2 \mathbf{P}(L)(1+R_2)\mathbf{P}(L)]^{-1} E_0. \tag{5.11}$$

The (1,1) component of the matrix in eq. 5.8 is:

$$\frac{t_1}{1 + r_1 r_2 e^{2ikL}} \tag{5.12}$$

from which, the intracavity field can be written as [15]

$$E_{Cav} = \frac{t_1}{1 + r_1 r_2 e^{2ikL}} E_0. \tag{5.13}$$

The intracavity reflected and transmitted fields are expressed as complex amplitudes of the respective fields, therefore they are not measurable quantities. As already explained in Chapter 1, in practice the measurable quantity is the power. Starting from the equation for the transmitted field, written as

$$E_T = \frac{t_1 t_2 e^{ikL}}{1 - r_1 r_2 e^{2ikL}}, \tag{5.14}$$

the power transmitted by a Fabry-Perot cavity can be written as:

$$P_T = E_T \cdot E_T^* = P_i n \frac{t_1^2 t_2^2}{1 + r_1^2 r_2^2 - 2 r_1 r_2} \cos(2kL). \tag{5.15}$$

This expression of the transmitted power, also known as the Airy function, shows its dependence on the phase accumulated during one round-trip, that is $2kL$. This function contains all the important information that can be extracted from a Fabry-Perot cavity. First of all, the resonance condition, which occurs when the phase shift $\Delta\phi = 2kL = 2n\pi$. This phase shift corresponds to a maximum of the transmitted power, and it also corresponds to a maximum of the intra-cavity power and a minimum of the reflected power [15]. The other important parameter of a resonant

Fabry-Perot cavity has been already defined in Chapter 1. It is useful to have a brief reminder: they are the free spectral range (FSR) in eq. 1.55, which is the frequency difference between two consecutive resonances; the linewidth (eq. 1.56) which is the full width at half maximum (FWHM) and it is related to the pole frequency of the cavity, expressed in eq. 1.65, such that $f_p = FWHM/2$. The linewidth depends on the reflectivities of the mirrors, then for cavities with high reflectivities r_1, r_2 (which is our case) it becomes very small, which means that the light makes more roundtrips inside the cavity. The most important parameter of a Fabry-Perot cavity is the finesse, already defined in eq. 1.54, which gives information about how much the cavity is able to separate adjacent spectral orders, in relation to the linewidth. Last, the storage time, defined in eq. 1.61, a parameter representing the mean storage time of a photon inside a cavity before it escapes through one of the mirrors, and it is related to the finesse of the cavity.
It is possible to distinguish three types of cavities, depending on the field reflected by the cavity. In particular, a cavity can be:

- **Undercoupled**: when $r_1 - r_2(1 - l_1) > 0$;
- **Critically coupled**: when $r_1 - r_2(1 - l_1) = 0$;
- **Overcoupled**: when $r_1 - r_2(1 - l_1) < 0$,

where l_1 are the losses at the input mirror, expressed in the equation $r_1^2 + t_1^2 + l_1 = 1$.

5.1.2 Dynamical effects

From the preliminary tests of local control for the alignment of SIPS 1 inch end mirror, it has been demonstrated that is possible to control its angular and linear motion within an accuracy of 10 nrad and 0.1 μm RMS (figure 4.14). Nevertheless, seismic noise at the suspension point of the pendulum can cause some residual motion of the suspended mirror (as better discussed in section 5.3.1), which affects the relative displacement between the two mirrors in the cavity. Therefore, it is interesting to study which are the dynamical effects derived from seismic or other vibrational noise. In particular, in this section, the evolution of the electromagnetic fields of the cavity when a mirror is moving will be presented. If we suppose that one of the mirrors of the cavity is moving, we can define its position with the function $X(t)$, as shown in figure 5.2. Therefore, the light travels for a path defined by the position of the mirror when its surface is hit by the light, given by $X(t^{'})$. Thus, the additional optical path can be written as

$$\Delta X = X(t^{'}) - x = c(t - t^{'}). \tag{5.16}$$

This translates into an additional phase of the electromagnetic field reflected by the mirror, given as

$$\phi(t) = \omega_0 t - 2kX(t^{'}), \tag{5.17}$$

where ω_0 is the nominal frequency of the laser and k is the wavenumber. This can be seen as a frequency shift due to a transfer of energy from the mirror to the wave,

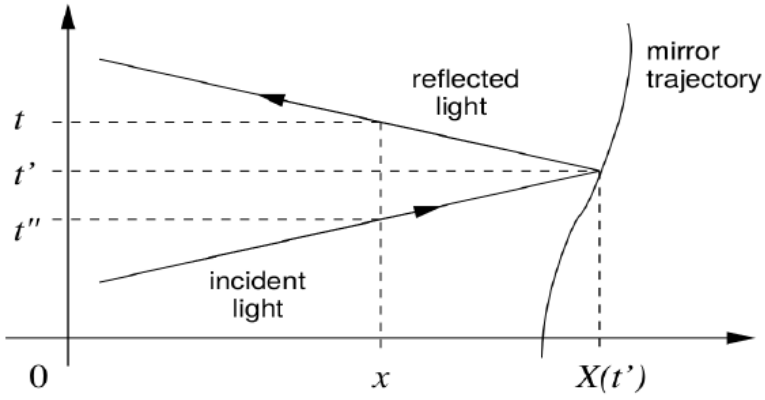

Figure 5.2: Scheme of the reflected light from a moving mirror [74]

and the new frequency can be calculated by deriving the phase in eq. 5.18:

$$\phi^{'}(t) = \omega_0 - 2k\frac{dX}{dt'}\frac{dt'}{dt} = \frac{c - v_m(t')}{c + v_m(t')}\omega_0 = \omega_{new}, \tag{5.18}$$

where v_m is the relative velocity of both mirrors, that is the cavity velocity. This expression shows that the movement of a mirror of the Fabry-Perot cavity causes a Doppler effect on the circulating wave. For low velocity motions, i.e. $c \gg v_m$, the reflection can be considered as instantaneous, $t^{'} = t$, and the previous expression can be simplified as:

$$\omega_{new} = \left[1 - 2\frac{v_m(t)}{c}\right]\omega_0 \tag{5.19}$$

If we consider a single mirror velocity such as the ones expected for SIPS in free motion, $v_m \sim 0.1\mu$m/s, the induced Doppler effect is very small (around 0.1 Hz). Nevertheless, for high finesse cavities (23000 for SIPS) this effect will accumulate on each round-trip of the beam inside the cavity and it can be of the same order of magnitude of the cavity linewidth, generating dynamical effects. Considering the effective number of round-trips made by a photon N_{eff}, related to the storage time τ by the relation $\tau = 2LN_{eff}/c$, we can write the total frequency shift induced by the Doppler effect as:

$$\delta\omega = \frac{1}{N_{eff}}\frac{|v_m(t)|\omega_0\tau}{L}. \tag{5.20}$$

From this, we can write the expression for the mirror velocity that makes the total Doppler shift equal to the linewidth, i.e. the FWHM of the resonance peak of the cavity, also called *critical velocity*:

$$v_{cr} = \frac{\lambda}{2\mathcal{F}\tau} = \frac{c\lambda\pi}{4\mathcal{F}^2 L} \tag{5.21}$$

For mirrors velocity $v_m \geq v_{cr}$, dynamical effects of the cavity start to be relevant. From this consideration, we can describe the behaviour of the intra-cavity field considering the mirror movement and so accounting for dynamical effects. Referring to figure 5.3, we can define the total distance traveled by a photon, at any time, inside the cavity as:

$$d(t) = L + x_2(t - T) = L + \xi(t) \tag{5.22}$$

where $T = L/c$ is the time needed for a photon to travel from one mirror to the other. Taking into account the variable optical path due to the mirror movement,

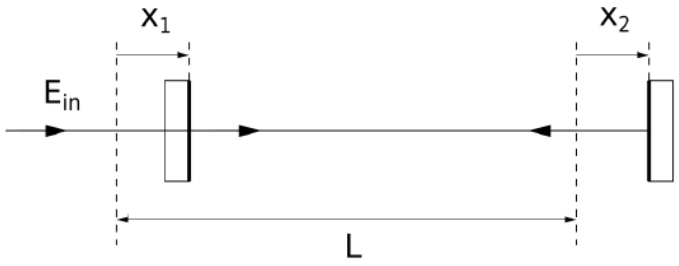

Figure 5.3: Fabry-Perot cavity with mirrors moving around a reference point [74]

we can write the intra-cavity field E_{Cav}: the total optical path will be determined by the number of round-trips made by the light field, so we can write the expression for E_{Cav} after N round-trips, can be simplified if we are in the large-N limit. For a number of round-trips $N \gg N_{eff}$ (the large-N limit [15]), the intra-cavity field is:

$$E_{cav}(t) = t_1 E_{in} \sum_{n=0}^{\infty} (r_1 r_2)^n e^{-2ikS_n(t)} \tag{5.23}$$

where S_n is a partial sum, which represents the total optical path after n round trips. Equation 5.23 can be re-written in terms of the finesse of an optical cavity $\mathcal{F}$ and of the storage time τ, as

$$E_{cav}(t) = t_1 E_{in} \sum_{n=0}^{\infty} e^{[i(2kv_m Tn^2 - 2kv_m tn) - \frac{2Ln}{c\tau}]} \tag{5.24}$$

This equation gives information about the behaviour of the intra-cavity field, for velocities of the mirrors v_m. When this velocity is $\geq v_{cr}$, some oscillations can appear once the resonance is passed: this effect is known as *ringing*. Even if the mirror movement is very slow the shape of the resonance peak changes and the power inside the cavity is smaller than the stored power expected for the cavity. Moreover, the mirror motion affects also the reflected and transmitted fields.

5.2 Longitudinal control

In the previous sections, we have shown how the seismic noise causes the suspended mirrors to move, thus generating a variation in the cavity length, which would change permanently if not controlled. This leads to the need for a longitudinal control, to actively correct the cavity length in order to keep it on resonance. The process which allows to measure the output of a system and feed it back to its input, with the aim to keep the system at the desired working point, is called a *feedback control loop*. Taking inspiration from Virgo experience, as a first approach, we decided to consider SIPS arm cavities as a linear optical resonator, or a *Linear Time Invariant* (LTI) system. When applied to LTI systems, such as the ones we find in interferometric

detectors, we can understand and predict the behaviour of our complex system by applying frequency domain techniques. A more detailed description of the basics of linear feed-back systems can be found in [75].

5.2.1 Linear systems

Most of the systems involved in interferometric detectors are well described by *linear time-invariant system* (LTI). A *linear* system is the simplest model of a physical system, characterized by a linear input-output relation. If the response of the system is the same independently of the time, it is called a *time-invariant* system. The most general expression of an LTI system is written as

$$x(t) = \int_{-\infty}^{0} h(\tau)y(t-\tau)d\tau \tag{5.25}$$

where $y(t)$ represents the input of the system, also called the forcing function, $x(t)$ is the output or response function, and $h(\tau)$ is the integral kernel. The damped harmonic oscillator is an example of a second order LTI system. The Laplace transform is a frequency-domain technique widely used in the theory of control systems, since it allows to find the time response of complex systems, by solving the differential equation on the s-domain. Given a signal $y(t) = 0$ when $t < 0$, its Laplace transform is defined as

$$\tilde{y}(s) = \int_{0}^{\infty} y(t)e^{-st}dt \tag{5.26}$$

where $s = \sigma + i\omega$ is a variable varying in a defined domain of the complex plane. This is a single-sided integral, which makes it perfect to analyse physical systems starting at t=0, because it can take into account initial conditions. Applying the Laplace transform to eq. 5.25 we obtains

$$\tilde{x}(s) = \tilde{h}(s)\tilde{y}(s), \tag{5.27}$$

where $\tilde{h}(s)$ is called the (Laplace) Transfer Function (TF) of the linear system, and it characterizes the behaviour of an LTI system on the s-domain. The TF of LTI systems can be described by rational functions, characterized by their poles and can therefore be written as [21, 15]:

$$\begin{aligned} G(s) &= \sum_i \frac{K_i}{(s-p_i)^{n_i}} \\ &= k \cdot \frac{(s-z_1)\cdot(s-z_2)\cdots(s-z_i)}{(s-p_1)(s-p_2)\cdots(s-p_i)}. \end{aligned} \tag{5.28}$$

In the first line of 5.28, n_i are the pole multiplicities and K_i are the corresponding residuals; in the second line, k represents the **gain**, all the z_i's are called the **zeros** of the TF, since they cancel its numerator, and all the p_i's that cancel the denominator of the TF are called **poles**. All the information needed to reconstruct the TF will be given by its zeros, poles, and gain. The analysis of the response of a system to an input function (such as an impulse), expressed by its TF, gives important information on system ***stability***. Indeed, eq. 5.27 tells that the response of a

system to an impulse signal can be found by simply making the anti-transform of the transfer function, being the Laplace transform constant at $t = 0$. Thus, it will contain oscillating terms at frequencies given by the imaginary part of each pole. Different situations can occur:

- if $\mathrm{Re}(p_i) < 0$, that is the pole has negative real part, the oscillation is damped;
- if $\mathrm{Re}(p_i) = 0$, means that the pole is purely imaginary and the oscillation has constant amplitude;
- if $\mathrm{Re}(p_i) > 0$, which means the pole has positive real part, the oscillation grows up exponentially.

Therefore a system is *stable* when, given an arbitrary function as input, such as an impulse, its response decrease asymptotically with time, which means that its TF has only poles with negative real part, $\mathrm{Re}(p_i) < 0$. On the contrary, a system is *unstable* if for an arbitrary input, the system response is an oscillation that increases with time, never returning to a quiescent state: this happens when TF$\rightarrow \infty$, which means the denominator of the TF goes to zero. In order to describe the properties of mechanical and optical systems, and develop a feed-back control system, transfer functions are described in terms of pole and zero frequencies and quality factors. A real first order zero, or simple zero, is usually called *differentiator* since it derives the input value in the time domain, while a simple pole is also known as *integrator*, because in the time domain it integrates the input value: at a given frequency f_0, they can be written respectively as [14]

$$\begin{aligned} Z_1(s) &= s - 2\pi f_0 \\ P_1(s) &= \frac{1}{s - 2\pi f_0}. \end{aligned} \tag{5.29}$$

Complex, or double, zero and pole, at frequency f_0 are given by [14]

$$\begin{aligned} Z_2(s) &= s^2 + \frac{2\pi f_0}{Q} + (2\pi f_0) \\ P_2(s) &= \frac{1}{s^2 + \frac{2\pi f_0}{Q} + (2\pi f_0)}, \end{aligned} \tag{5.30}$$

where Q is the *quality factor*: in particular if $Q = 0$, the system has a simple zero or pole given in eq. 5.29. The last equation describes a system with an impulse response which is represented as a damped oscillation at frequency $f = f_0\sqrt{1 - 1/4Q^2}$. Moreover, the time constant is related to the quality factor Q by the expression $\tau = Q/(\pi f_0)$. This tells us that the higher the Q, the longer the oscillation will last. To better understand the behaviour of such a system, consider as an example the damped harmonic oscillator with friction, described by a second order pole. The general solution for a free vibration of a damped second order system can be written as

$$x(t) = e^{-\zeta\omega_n t}[A_1 e^{\sqrt{\zeta^2-1}\omega_n t} + A_2 e^{-\sqrt{\zeta^2-1}\omega_n t}], \tag{5.31}$$

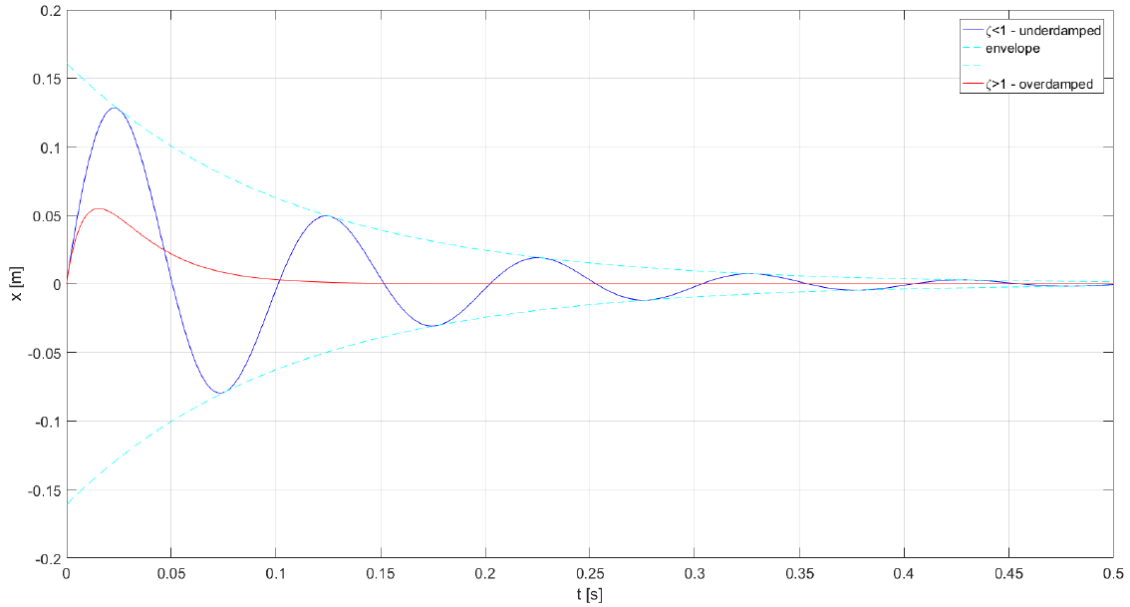

Figure 5.4: Impulse response of a damped harmonic oscillator for different values of the viscous damping factor ζ, in time domain.

where ζ is the viscous damping factor and is related to the quality factor by the expression

$$\zeta = \frac{1}{2Q}. \tag{5.32}$$

Thus, in eq. 5.31, the nature of the roots depends on the value of ζ, which means also that the behaviour of this system is determined by the value that the quality factor can assume. In particular, three cases can occur:

- $Q > 1/2$ ($\zeta < 1$): the system is **Underdamped** (complex and conjugate roots represent a damped harmonic motion);
- $Q < 1/2$ ($\zeta > 1$): the system is **Overdamped** (real roots, with a not periodic damped motion);
- $Q = 1/2$ ($\zeta = 1$): the system is **Critically damped** (real and coincident roots).

The response of the damped harmonic oscillator to an impulse of velocity as input is illustrated in figure 5.4, for the three values of ζ. At the same time, the global behaviour of this system in frequency domain is described by poles and zeroes of the TF, as shown in figure 5.5 for different values of the quality factor.

5.2.2 Feed-back control system

The most common control systems, which is suitable for the longitudinal control of a Fabry-Perot cavity of an interferometer device such as SIPS, are those working in feed-back configuration. In the following, some useful basics concepts of control system theory are described focusing on linear control systems.

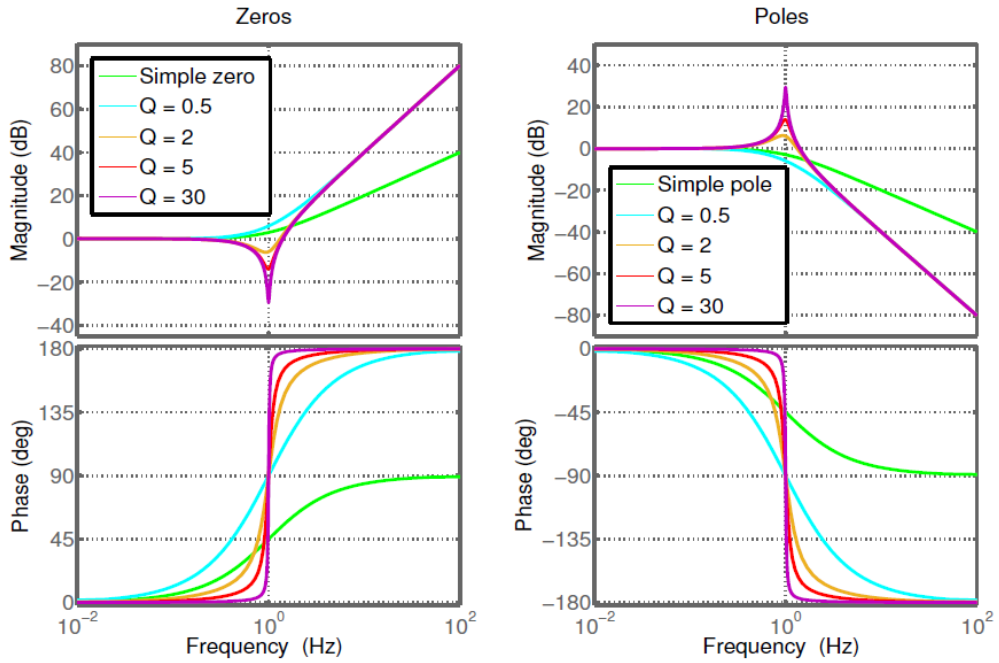

Figure 5.5: Frequency response of a second order system for different values of Q [15]. **Left**: Transfer function of a second order system with a zero. **Right**: Transfer function of a second order system with a pole.

In order to implement a feedback loop to control the length of the cavity, we must define the elements in the control problem, as in figure 5.6, where the simplest situation in a problem of control is shown. They are:

- **Plant**: the physical object that must be controlled, which in our case is a Fabry-Perot cavity and its length and it can be described as a linear system with one single input and one single output (SISO).
- **Error Signal**: it provides information on the parameters to be controlled. In our case, it is the length of Fabry-Perot cavity and its distance from the resonance condition. It will be a PDH signal, as will be better explained in the next section.
- **Corrector or feedback filter**: the error signal passes through this element which computes the *correction signal* to be sent to the plant.
- **Actuator**: it acts on the plant by feeding the correction signal, calculated by the filter, in order to recover the working point. In the case of SIPS the actuators will be the same used for local control, the coils-magnets pairs already described in chapter 4, for which the TF is a simple pole given by its particular RLC circuit.

The response of the plant is described in general by a linear transfer function $G(s)$, depending on the Laplace variable s. The error signal can be affected by noise coming from the sensors itself, the *sensing noise* $n(s)$ (grey square in figure 5.6), or

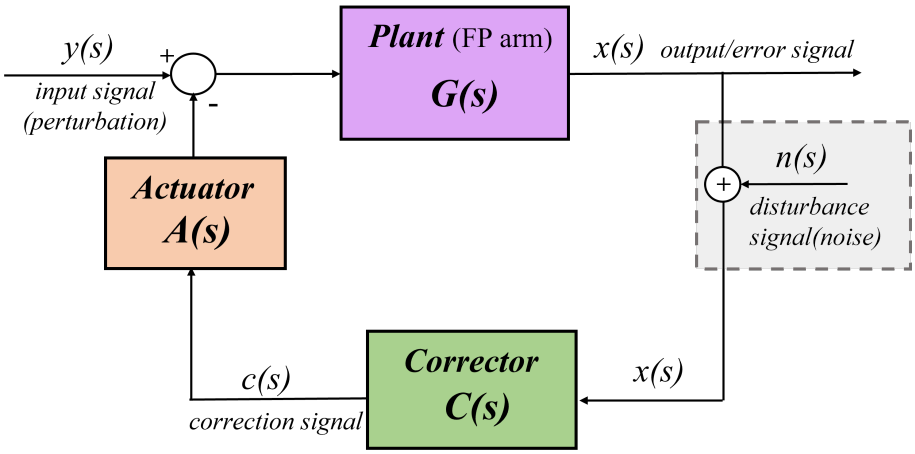

Figure 5.6: Scheme of a simple feedback loop for the control of the length of Fabry-Perot cavities, the *Plant* $G(s)$ [14]: the filter $C(s)$ calculates the correction needed to bring the cavity on resonance, taking information from the error signal $x(s)$, then correction $c(s)$ is sent to the coils, the *Actuator* $A(s)$, that act on magnets attached to the mirror. Disturbance noises are eventually also considered (grey square).

can be injected on purpose to measure the features of the system. Indeed, the input function, $y(s)$ in figure 5.6, is a perturbation that brings the plant out of its working point. Moreover, the output function, $x(s)$, can be considered as the error signal. Since the goal of a control system is to keep the input degree of freedom as close as possible to a *reference* value and considering that we deal with a linear system, the reference value can be taken as equal to 0 [14]. In our case, error signal $x(s)$ can be used as a reference value, which means that controlling the input degree of freedom is equivalent to keep the error (output) signal close to zero. This also explains why we refer to this scheme of control system as ***feedback control loop***: the output of the system is also used as part of the input. In particular, when the feed-back signal is disconnected from the input signal, the system is in the open loop configuration, and the *open loop transfer function* $TF_{OL}(s)$, also called *open loop gain* [14], is given by:

$$TF_{OL}(s) = G(s)C(s)A(s), \tag{5.33}$$

which is the product of the individual TF of the elements composing the loop. It is useful to measure the open-loop transfer function of the feed-back systems. Indeed by adding a disturbance signal $n(s)$ to the controlled DOF, through the actuators, the output signal $x(s)$ will give the residual motion of the physical systems (already done for a single mini-payload, as discussed in chapter 4). In particular, the frequency at which the gain equals to one, that is $TF_{OL}(s) = 1$, is called *unity gain frequency* (UGF) or *band-width* of the loop. When $TF_{OL}(s) > 1$ at a given frequency s, the error signal gives a good estimate of the residual motion of the free system. When the feedback loop is closed, which means the feedback signal is connected to the input, the control system is in a closed loop configuration, and we can define the *closed loop transfer function* $TF_{CL}(s)$, or *closed loop gain* as

$$TF_{CL}(s) = \frac{1}{1 + G(s)C(s)A(s)}, \tag{5.34}$$

which represents a suppression factor that tells us how much signals are reduced with respect to the free motion of the system. The performance of a linear feedback system, described by $TF_{CL}(s)$, can be studied by analyzing the response of such a system to an input step function, which in the Laplace domain is expressed as $y(s) = 1/s$. Thus, the system output is

$$x(s) = TF_{CL}(s)y(s) = \frac{TF_{CL}(s)}{s}. \tag{5.35}$$

Computing the anti-transform of this expression for large times, by using the final value theorem [14], the response of the linear system to the input step goes to zero only if its transfer function includes a zero at $s = 0$, i.e. the output $x(s) \to 0$ when $TF_{CL}(0) = 0$. Therefore the transfer function of the system, given in eq. 5.34, has a zero at the origin only if $TF_{OL}(s)$, has a simple pole for $s = 0$, also called a *pure integrator*. For this reason, real poles at $s = 0$ are usually added to the correction filter [14]. With this considerations, the behavior of the full linear system, in closed loop configuration can be easily computed and the transfer function of such system can be written as [15]:

$$TF_{FP}(s) = \frac{x(s)}{y(s)} = \frac{G(s)}{1 + G(s)C(s)A(s)}. \tag{5.36}$$

which means that the signals of the system will be reduced, with respect to the uncontrolled state, by an amount given by the suppression factor in eq. 5.34.

5.2.2.1 Loop Stability

In section 5.2.1, the response of second order linear system, the damped harmonic oscillator, to an impulse of velocity as input is has been introduced, together with the subject of stability of a system. As already explained, the stability of the feed-back system of figure 5.6, requires that the poles of the closed-loop system must have negative real parts and lie in the left half plane. The behaviour of a feed-back system, which is also linear, will be then completely characterized by the impulse response, whatever the input. In particular, it will be stable when the response to an input impulse is a limited output signal, or better it will be asymptotically stable when the output goes to zero at $t \to \infty$ [14]. The link between the behavior of the system transfer function and the requirements of stability for the closed-loop feed-back system can be derived using the Nyquist stability criterion [75]. The Nyquist diagram provides some graphical information on how the poles of the closed-loop control system move, by changing the gain of the controller in the complex plane. Moreover, the stability of a feed-back control system can be determined from its open loop TF, $TF_{OL}(s)$. Indeed, the feedback system is asymptotically stable if and only if its closed loop transfer function $TF_{CL}(s)$ has no pole for $Re(s) \leq 0$. This means that the closed-loop system is stable if and only if the function $1 + TF_{OL}(s)$, i.e the denominator of $TF_{CL}(s)$ in eq. 5.34, has also no zeros in the right half plane. If this condition does not occur, any external disturbance will result in the amplification of the input signal, which will soon diverge exponentially and the system becomes unstable. Therefore, the Nyquist stability criterion for the stability of

closed-loop feed-back system is determined: given a system with stable open-loop transfer function, it will also be stable in the closed-loop configuration if and only if its Nyquist plot does not encircle the critical point $TF_{OL}(s) = -1$ in clock-wise sense [14].

Another common way used to represent the open loop transfer function of a system is through the **Bode plot**: it is composed of two different plots representing the absolute value of the TF (the magnitude in dB) and the phase of this TF as a function of frequency. This plot is useful to determine the phase and the gain of the open loop TF, knowing where the UGF is located in the plot. Moreover, the range of stability of the system can be defined by two parameters, that are the **phase margin** and the **gain margin**. They can be determined knowing two particular frequency values: i) the UGF, already defined, and ii), the **180° crossover**, which is the frequency, closest to the UGF, at which the phase becomes 180 [15]:

- the **phase margin** is the phase computed at the UGF$-(\pm 180°)$: when the crossover frequency is positive ($+180°$) the system will be stable, when it is negative ($-180°$), the system will be unstable, while its absolute value gives the information about the amount of margin you can have on the phase, before the system become unstable;
- the **gain margin** is given by the values of the amplitude at both $\pm 180°$ and gives as well information of system stability range.

In figure 5.7, the Bode diagram for the open loop TF of the Advanced Virgo arm cavities is shown: the red bar represents the UGF, that is 65 Hz, while the blue bars define the 180° crossover points, which is at frequencies of 2.8 Hz and 215 Hz [15]. Nevertheless, the Bode diagram is not useful to have information on the stability of the closed-loop system.

An alternative representation of the system's frequency response is the **Nichols chart** [76]: it is obtained by plotting the magnitude of the open loop transfer function $TF_{OL}(s)$, expressed in dB, versus its phase, when the frequency varies from 0 to $+\infty$. Assuming that no unstable pole/zero cancellation takes place in $TF_{OL}(s)$, the stability criterion is obtained by mapping the critical point $(-1, 0)$, the ray $\mathcal{R}_{(-\infty,-1)}$ and the Nyquist plot of $TF_{OL}(s)$ into the Nichols chart. Moreover, the relationship between the Nyquist and Nichols stability criteria is fully described by using the 180° crossing concept [77]. The request of Nyquist criterion that the critical point -1 is not encircled translates into the request that the Nichols plot crosses the unity gain axis between the two points corresponding to $-180°$ and 0 phases [14]. An example of the Nichols chart is illustrated in figure 5.8. This plot is particularly useful for easily obtaining information on the behavior of the closed-loop transfer function TF_{CL} near the UGF, giving information about the amplification of the system for each frequency. Indeed, even if your system is stable, if the open loop transfer function passes close to the critical point, the motion of the system can be enhanced instead of reduced at that frequency, since TF_{CL} can be much greater than 1. This enhancement is called *overshoot* and a limit on it can be imposed, only knowing the behavior around the UGF [14].

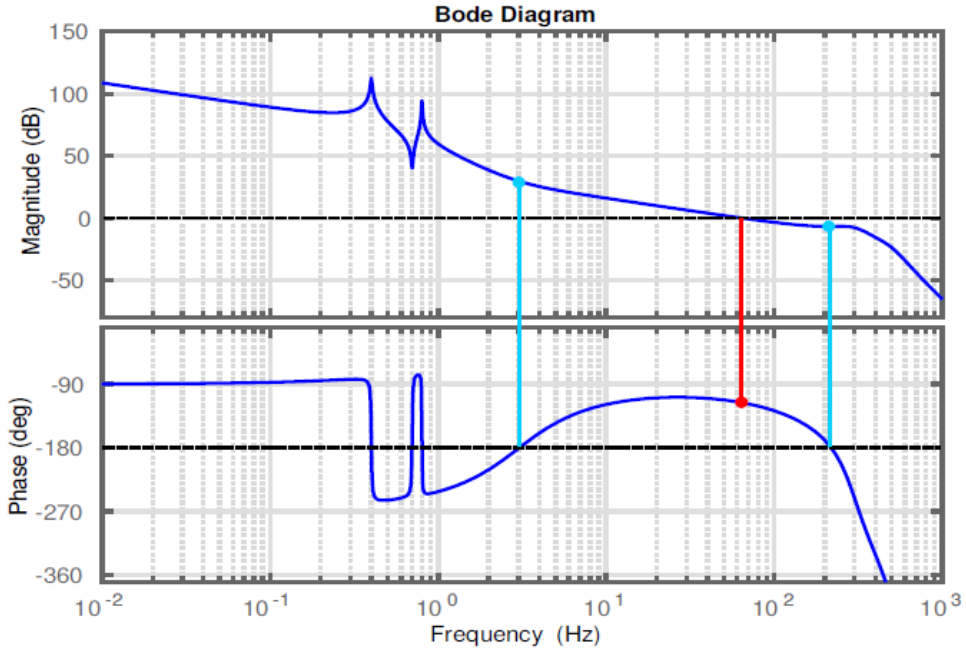

Figure 5.7: Example of Bode plot: the magnitude of the transfer function and its phase are shown in two different panels as a function of frequency. See [15] for more detail.

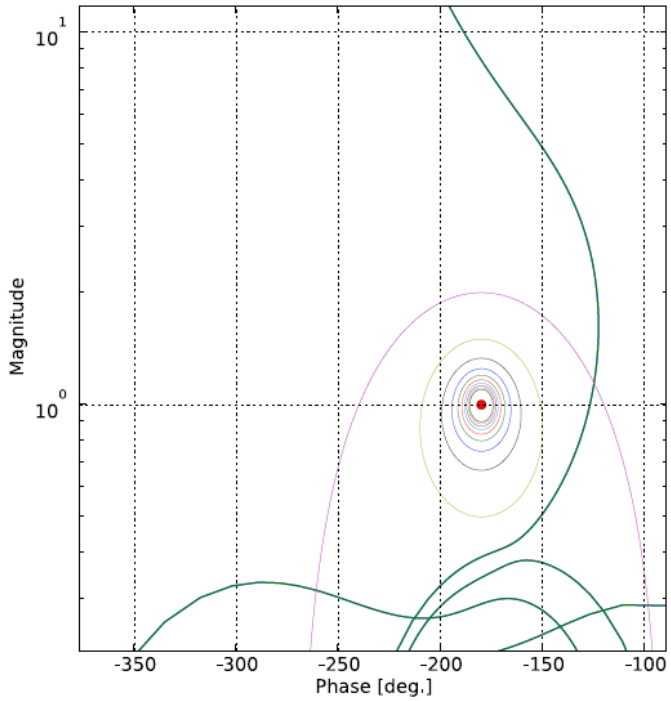

Figure 5.8: Example of Nichols chart of a stable system: the magnitude (in dB) of the open loop transfer function and its phase are plotted for frequency varying from 0 to $+\infty$. The curves around the critical point show the minimum margin allowed with an overshoot varying from 1 to larger values, in steps of one unity [14].

Moreover, Nichols chart allows to extract the stability margins. The *phase margin* is represented by the horizontal line going from the critical point to the Nichols plot, and it is an important information since it gives an indication of the robustness of the control, also if there are changes in the system transfer function. The *gain margins*, which is the maximum possible changes in the overall gain of $TF_{OL}(s)$ that leave the system stable, is represented by the vertical translation of the critical point from the Nichols plot. If it is large enough to make the curve cross the critical point, the system becomes unstable, thus instability oscillations occur with typical frequencies given by the two points of the Nichols plot that intersect the 180° degrees vertical line.

5.2.3 Pound Drever Hall locking technique

In a control scheme, the error signal is an important element, since it contains information about the length of the cavity with respect to the resonance point. An ideal error signal has to satisfy the following conditions:

- it must be *bipolar*, that means that it changes sign depending on which side of the working point we are;
- it is linear, meaning it is proportional to the parameter we want to measure
- it crosses the zero at the desired working point.

to obtain an error signal with all these requirements, the method used in a GW interferometer is the Pound-Drever-Hall technique (PDH) [19]. We have shown that the resonance condition for a Fabr-Perot cavity is satisfied when the length of the cavity is $L = n\lambda$, which, in terms of frequency is satisfied when the laser frequency is an integer number of the cavity the FSR ($2L/c$). For this reason a little change in the distance between the two cavity mirrors leads the cavity out of the resonance condition. To solve this problem, this distance must be actively adapted to the beam wavelength. To obtain this, a suitable voltage signal must be sent to the actuator. In particular, the PDH technique was first developed with the aim of stabilizing the laser frequency on reference cavities, but it is used in GW interferometer to lock a resonator to the laser cavity, making possible to compute the error signal and thus to understand what is the suitable signal to send to the actuator. In general, assuming that the laser frequency is stable, this technique is applied in a configuration as the one shown in figure 5.9. In this scheme, an Electro Optic Modulator (EOM) is placed to modulate the incident light (usually it is the Pockel Cells). In our experiment, at this purpose an EOM will be placed in the SIPS main laser injection line. For a better understanding, it is useful to first introduce the light modulation concept. If we consider first the no-modulated light, being the cavity input and reflected electromagnetic fields, respectively written as

$$E_{in} = E_0 e^{i\omega t} \qquad E_{ref} = E_1 e^{i\omega t} \tag{5.37}$$

it is possible to define the reflection coefficient as

$$F(\omega) = \frac{E_{ref}}{E_{in}} = \frac{r \exp\left(i\frac{\omega}{FSR}\right) - 1}{1 - r^2 \exp\left(i\frac{\omega}{FSR}\right)}, \tag{5.38}$$

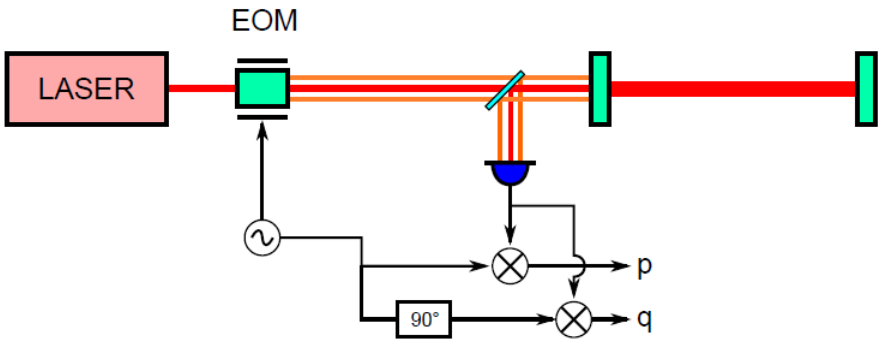

Figure 5.9: Scheme of the Pound-Drever-Hall technique for measurements of a Fabry-Perot cavity length. [14]

where FSR is the free spectral range of the cavity. If the input beam is phase-modulated, its electromagnetic field can be written as

$$E_{inc} = E_0 e^{i(\omega t + \beta \sin \Omega t)} \tag{5.39}$$

where β is the amplitude of the phase modulation called *modulation depth*, while Ω is the radio frequency modulation. Expanding the exponential in terms of the Bessel functions, we can write:

$$\begin{aligned} E_{inc} &\simeq [J_0(\beta) + 2iJ_1(\beta)\sin\Omega t]e^{i\omega t} && (5.40)\\ &= E_0[J_0(\beta)e^{i\omega t} + J_1(\beta)e^{i(\omega+\Omega)t} - J_1(\beta)e^{i(\omega-\Omega)t}] && (5.41) \end{aligned}$$

where the first term is the carrier beam at a frequency ω and the other two terms are the lower and the upper sidebands, respectively at frequencies $\omega - \Omega$ and $\omega + \Omega$. The total reflected beam can be written as

$$E_{refl} = E_0[F(\omega)J_0(\beta)e^{i\omega t} + F(\omega+\Omega)J_1(\beta)e^{i(\omega+\Omega)t} - F(\omega-\Omega)J_1(\beta)e^{i(\omega-\Omega)t}]. \tag{5.42}$$

Usually, high order sidebands have a much smaller amplitude and they are often neglected. Thus, for a modulation depth $\beta < 1$ we can approximation of the Jacobi functions as [21]

$$J_0(\beta) \sim 1 - \frac{\beta^2}{4} \tag{5.43}$$

$$\tag{5.44}$$

$$J_1(\beta) \sim \frac{\beta}{2}, \tag{5.45}$$

and the total power is the sum of the carrier power P_c and of the power of the two sidebands $2P_s$:

$$P_0 \sim P_c + 2P_s. \tag{5.46}$$

If we choose properly the modulation frequency we can ensure that the sidebands are not resonant inside the cavity when the carrier is. When a field is resonant inside the cavity, the phase of its reflection changes very fast as a function of the cavity

length, while when a field is not resonant, its phase is roughly constant even when the cavity length varies a bit around the working point. We can therefore use the sidebands as static phase references for the measurement of the carrier phase. The beating between sidebands and carrier is the error signal we are interested in because it gives the phase difference between them. Thus, we want to extracting the beat note at the modulation frequency [21], which is the basic idea of PDH technique. The power of the reflected modulated beam, that arrives to the photodetector is

$$\begin{aligned} P_{ref} &= P_c|F(\omega)|^2 + P_s\{|F(\omega+\Omega)|^2 + |F(\omega-\Omega)|^2\} \\ &+ 2\sqrt{P_cP_s}\{Re[F(\omega)F^*(\omega+\Omega) - F^*(\omega)F(\omega-\Omega)]\cos\Omega t \quad (5.47) \\ &+ Im[F(\omega)F^*(\omega+\Omega) - F^*(\omega)F(\omega-\Omega)]\sin\Omega t]\} \quad (5.48) \\ &+ (2\Omega \quad \text{terms}). \quad (5.49) \end{aligned}$$

For a low modulation frequency

$$\Omega \ll \frac{FSR}{F} \qquad \Leftrightarrow \qquad \Omega \ll FWHM \tag{5.50}$$

where FWHM is the cavity linewidth, the dominating interference term is

$$P_{ref}^{c-SBs} = 2\sqrt{P_cP_s}Re[F(\omega)F^*(\omega+\Omega) - F^*(\omega)F(\omega-\Omega)]\cos\Omega t; \tag{5.51}$$

while, for a high modulation frequency

$$\Omega \gg \frac{FSR}{F} \qquad \Leftrightarrow \qquad \Omega \gg FWHM \tag{5.52}$$

$$P_{ref}^{c-SBs} = 2\sqrt{P_cP_s}Im[F(\omega)F^*(\omega+\Omega) - F^*(\omega)F(\omega-\Omega)]\cos\Omega t. \tag{5.53}$$

In order to isolate the term which contains the relevant information, the photodiode output power is multiplied by a local oscillator signal (LO). This process is also known as demodulation of the error signal. The result will contains several components, each one oscillating at different frequencies: low frequency DC term, which is the one containing the beating note, Ω and 2Ω. However, since we are interested only in the low frequency, i.e the DC component we can neglect the higher frequency terms by applying a low pass filter to the result [21]. Therefore, this signal will be sent to a mixer (see figure 5.9), together with a local oscillator signal $\sin\Omega_{LO}$. The mixer output will be

$$\sin(\Omega t)\sin(\Omega_{LO}t) = \frac{1}{2}\{\cos[(\Omega-\Omega_{LO})t] - \cos[(\Omega+\Omega_{LO})t]\} \tag{5.54}$$

and, if $\Omega_{LO} = \Omega$, the first term provides us a DC signal. If the local oscillator signal is $\cos\Omega_{LO}t$, the output of the mixer will be

$$\sin(\Omega t)\cos(\Omega_{LO}t) = \frac{1}{2}\{\sin[(\Omega-\Omega_{LO})t] - \sin[(\Omega+\Omega_{LO})t]\} \tag{5.55}$$

this means that, when $\Omega_{LO} = \Omega$, the DC signal vanishes. For this reason, after the local oscillator and before the mixer a phase shifter is placed [33]. The signal in low modulation frequency regime ($\Omega \ll FWHM$) will be

$$\epsilon = P_0\frac{d|F|^2}{d\omega}\Omega\beta \approx 2\sqrt{P_cP_s}\frac{d|F|^2}{d\omega}\Omega \tag{5.56}$$

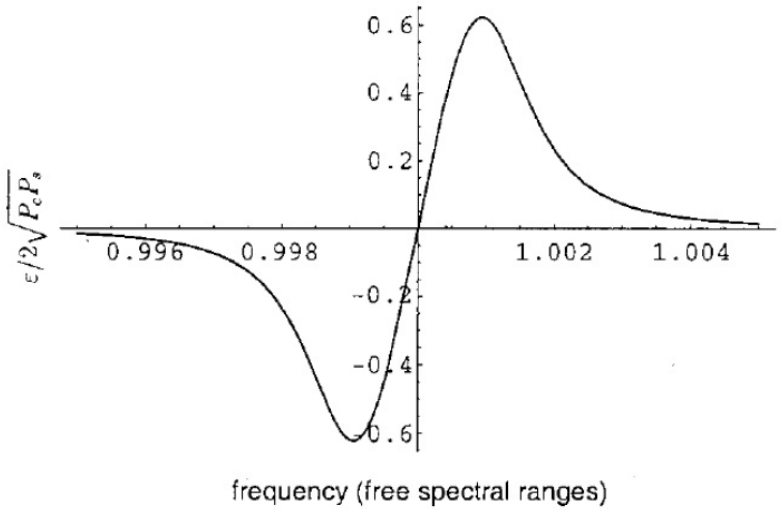

Figure 5.10: Pound Drever Hall signal in low modulation frequency regime. [19]

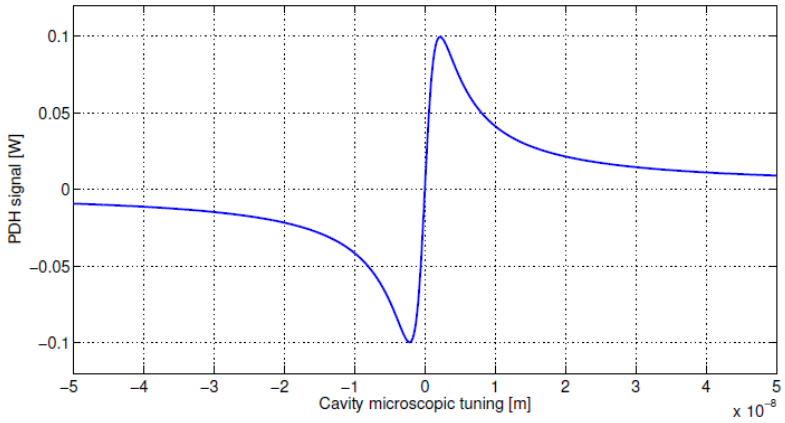

Figure 5.11: Pound-Drever-Hall signal in reflection of a Fabry-Perot cavity with Advanced Virgo parameters and an input power of 1 W. [15]

and this represents the error signal which is sent to the servo controller. The shape of this signal is shown in figure 5.10. Since we deal with measurable quantity, we can consider only the real part of the result. There are only two independent signal that can be used to reconstruct all possible values of the demodulation phase. Indeed, depending on the phase of the demodulation signal, the information obtained will be different. Thus, the signal is multiply by a sine or a cosine, obtaining two signals which are respectively called *in-phase* signal, when $\phi = 0$, and *quadrature* signal, when $\phi = \pi/2$. In this way, we can obtain information on the behavior of the in-phase signal as a function of the cavity displacement from resonance. An example of PDH signal for an Advanced Virgo cavity is shown in figure 5.11: it is interesting to note that the signal shows a linear dependence on the cavity displacement when close enough to the resonance, and the width of the linear region is proportional to the cavity line-width [21]. Without going into detailed computation (see [21] for a deeper analysis), it is possible to compute the slope of the linear region, by making the derivative of the in-phase signal P with respect to the mirror longitudinal

displacement, evaluated at the origin. If we assume a high cavity finesse we obtain:

$$\frac{dP}{dz} = J_0(\beta)J_1(\beta)P_{in}\frac{8\mathcal{F}}{\lambda}. \tag{5.57}$$

This expression tells us that the slope of the error signal depends on the finesse of the cavity. This means that, the larger the finesse is, the more our signal will be sensitive to the cavity length variation. Nevertheless, this would also imply a smaller linewidth and so a narrower linear region. Then, to design a good control of the cavity length, we must find a compromise between both parameters. The signal is also proportional to the input power, while the shot noise increases only with the square root of the power. We can therefore have a gain in the signal to noise ratio which is proportional to the square root of the power we are injecting into the cavity. Finally, since the error signal can only be used within its linear region, we want to increase the width of this region. This can be done with a linearization process of the error signal (as better described in [14]). It can be shown (see [15]) that, if we write the PDH signal in terms of the transmitted cavity power, we can use it to remove the limitation on the linear region of the reflected power, normalizing it by this transmitted one. In the case of SIPS, for the locking of its optical cavity and of the entire interferometer, a system of auto-alignment is foreseen to be used. Thus, the transmission signals from each Fabry-Perot cavity must be acquired and processed to compute the error signal applying the Pound-Drever-Hall technique [19], in order to keep the interferometer in its working condition. A preliminary optical bench design, including two photodiodes in trasmission from Fabry-Perot cavities, is shown in figure 5.12.

5.3 Optimization of SIPS control system

In order to design an efficient optical control system for SIPS, we need first to study the analytical model of the system to be controlled, thus to design a controller based on the proposed model, which means to have equations describing the different part of the control scheme: plant, sensors, correction filters and actuators. From the preliminary results of the tests of local control for SIPS mini-payload, it has been decided to work on optimization of control system by first introducing some modification of the physical system, that is the "plant" of this system. This is the work on new design of SIPS mechanics and the suspension system already described in Chapter 4. Nevertheless, an important part of the realization of an optimal control design is the study and development of the mathematical model of the system which has to be controlled (the plant), which is part of this PhD work discussed in sec. 5.3.2.

5.3.1 Locking requirements

The requirements about force and bandwidth needed for the lock acquisition of the SIPS high finesse Fabry-Perot cavities has been computed, according to the design: they are preliminary computations and a more precise result can be obtained by performing time domain simulations. Moreover, a very important parameter is the

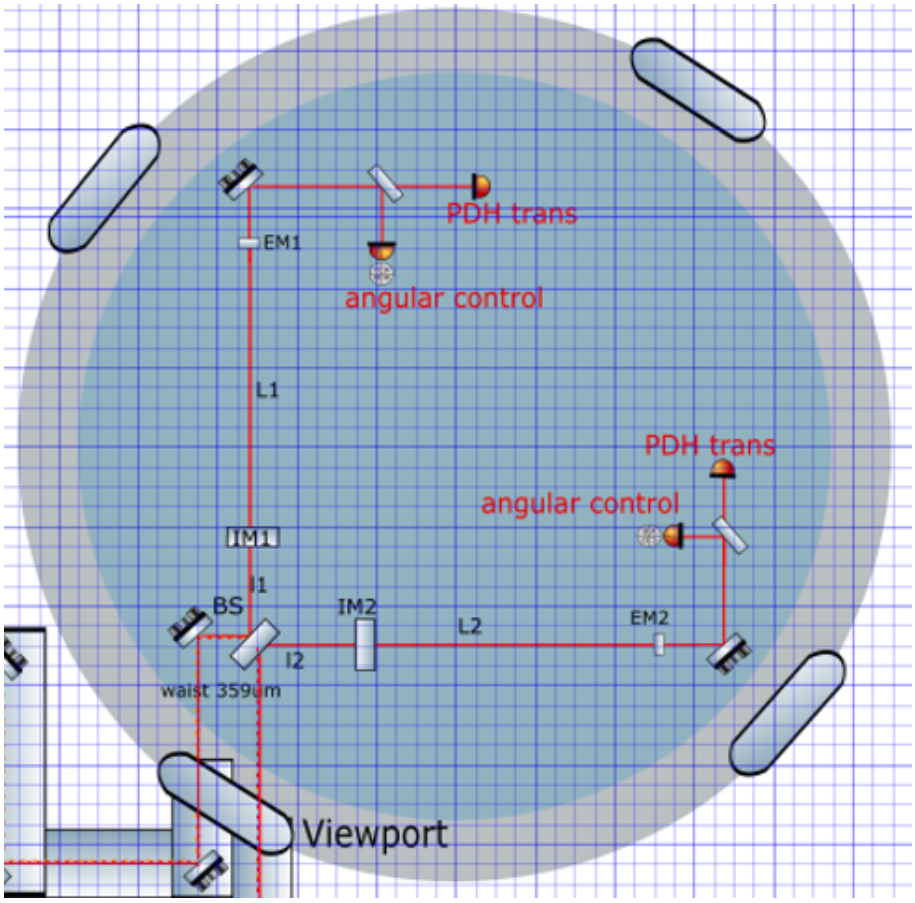

Figure 5.12: Preliminary optical bench design of SIPS: two photodiodes will be placed in transmission from each Fabry-Perot cavities for locking and angular control, taking inspiration from the system used in Virgo [15]

relative displacement (and relative speed) between the two mirrors of each Fabry-Perot cavity. Although it is difficult to estimate, it can be computed analytically from the model developed and described in section 5.3.2 and, when SIPS interferometer setup will be finalized according to the final design, it can be measured and compared with the analytical equations, also for the validation of the theoretical model. The first requirement to be considered is on the relative seismic displacement between the two mirrors of the cavity. Considering that both end and input mirrors are independently suspended with two single pendulums at the same auxiliary bench, and assuming that the seismic common mode rejection between the two mirrors is negligible, the seismic noise at the suspension point of the two pendulum has been computed to be $\sim 0.2\mu$, dominated by a 0.1 Hz displacement, thus giving the corresponding speed of $v_m \sim 0.1 \cdot 2\pi \cdot 0.2 = 0.1\mu m/s$ (refer to eq. 5.18). The second important requirement is the minimum force needed to acquire the lock, i.e. the force needed to put the relative mirror velocity v_m to zero, which can be simply defined as:

$$F\Delta t = mv_m, \tag{5.58}$$

where Δt is the time interval in which the error signal has a linear trend, $\lambda = 1064$ nm is the main laser frequency, while m and v are the mirror mass and speed,

respectively. The crossing time of the resonance, defined by the time needed to cross the half width at half maximum (HWHM), is:

$$\Delta t = \frac{\lambda}{4\mathcal{F}v}, \tag{5.59}$$

where $\mathcal{F}$ is the cavity finesse. Considering SIPS finesse of $\mathcal{F} = 23000$, and combining the previous two equations, we obtain the lower limit of the forces that must be applied to both cavity mirrors, in order to be in a stable condition which allows the locking of the cavity, that is:

$$F = \frac{4m\mathcal{F}v^2}{\lambda} = 3.6 \times 10^{-4}(\frac{v}{0.1\mu m/s})^2 N, \tag{5.60}$$

for the end mirror with 10 g of mass, while for the input mirror with a mass of 300 g this formula gives

$$F = \frac{4m\mathcal{F}v^2}{\lambda} = 1.2 \times 10^{-5}(\frac{v}{0.1\mu m/s})^2 N. \tag{5.61}$$

The effective time during which the loop is acting can be increased by linearizing the Pound-Drever-Hall error signal and the efficiency of the linearization technique depends on the noise of the photodiodes and by the presence of high-order modes, as already explained in section 5.2.3. Another important parameter, in particular for the design of a control loop, is the bandwidth B, which determines the reaction time of a control loop. Indeed, we have seen in section 4, when SIPS local control is active mirror displacement is approximately $0,1\mu m$ RMS. In order to acquire lock, the loop needs to react faster than the time to cross a resonance, which means:

$$v_{max,B} < \frac{\lambda}{2\mathcal{F}} 2\pi B \tag{5.62}$$

Then, the minimum bandwidth needed to acquire the lock has been computed for SIPS and it is given by:

$$B \sim \frac{1}{\Delta t} = 4.6 \text{ kHz}. \tag{5.63}$$

Finally, as anticipated in section 5.1.2, the ringing effect is present when the time to cross a resonance is smaller than the time needed to fill the cavity with the light. In this case the quasi-static approximation can not be used anymore, and the errors signals for the cavity control become oscillating during the crossing of the resonance (ref. a PDH). The condition for ringing for SIPS arm cavities is given by

$$v \geq \frac{c\lambda\pi}{4\mathcal{F}^2 L} \tag{5.64}$$

where the last terms is the critical velocity expressed in eq. 5.21, which for SIPS arm cavities has been computed to be $v_{cr} \sim 1.35\mu m/s$. Therefore, with the expected speed, $v_m \sim 0.1\mu m/s$, the condition $v < v_{cr}$ can be satisfied, meaning that we expect no ringing effect.

5.3.2 Analytical model for opto-mechanical coupling

In this section the analytical model for the opto-mechanical interaction inside the FP cavities, is developed, with the aim of build an optimal control algorithm for the implementation of the control system for the cavities length control. In particular, the equation of motion of the wave field coupled with the resonator by boundary condition are derived, using the Hamilton **variational principle** approach. The results obtained from this analysis will be used to develop an integro-differential model using Pontryagin's maximum principle, which will allow to find efficient control equations to be implemented in a complex systems like SIPS, in order have a complete control of all the optical elements, simultaneously, thus to optimize SIPS performance. The case of the opto-mechanical resonators requires also considerations on additional effects related to quantum mechanics, which can be considered as the same of the elastic waves if very low energy and small scales are taken into account [78]. We first develop a nonlinear theory of the scattering phenomenon describing the expression for the radiation pressure acting on a body moving in the wave field by using Hamilton's variational principle. The Hamilton's principle permits to determine a general procedure to study the scattering of acoustic and electromagnetic waves on a moving surface. This will lead us to determine the final expressions of the wave field and the resonator motion. The approach used is placed in the context of classical acoustics and electrodynamics. The mathematical method used for describing the coupling is conceptually the same of the wave-body interaction problem in acoustic or electromagnetic waves. As explained in [78], the one-dimensional problem has been treated for both acoustic and electromagnetic waves, deriving the wave-body interaction for both cases, in order to compare them to understand differences and commonalities for the two kinds of propagation phenomena. In the case of acoustic waves, some non-linearities appears both in the boundary conditions and also in the equation of motion of the wave. However, parts of the boundary terms are common to acoustic and electromagnetic waves, in particular the Lagrangian pressure.

We analyse the one dimensional problem of a light beam impinging and reflecting on a dielectric mirror with surface S, and mass m, connected to a spring of stiffness k (shown in figure 5.13). Lets introduce the scalar and vector potentials, ϕ and A for the electric and magnetic field, E and B respectively:

$$\mathbf{E} = -\nabla\phi - \mathbf{A}_t \tag{5.65}$$

$$\mathbf{B} = \nabla \times \mathbf{A} \tag{5.66}$$

In order to apply the variational principle approach, we define the generalized Lagrangian L for the opto-mechanical system, as the difference between the total kinetic energy and the total potential energy of this system. For the electromagnetic field, kinetic energy is represented by the magnetic energy, while the energy of the electrical field replaces the gas elastic potential energy storage [78], thus the

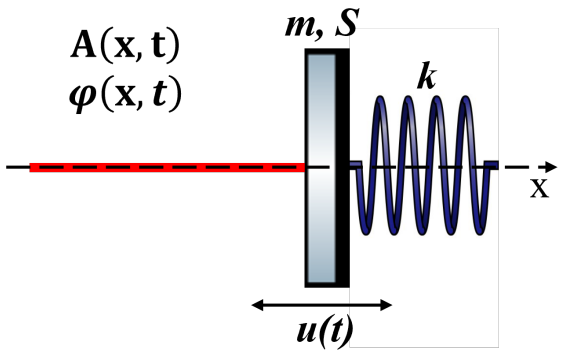

Figure 5.13: Schematic view of the interaction between laser field and a Fabry-Perot cavity mirror.

Lagrangian density can be written as:

$$\begin{aligned}\mathcal{L}_{e.m.} &= \frac{1}{\mu_0}|\mathbf{B}|^2 - \epsilon_0|\mathbf{E}|^2 \\ &= \frac{1}{\mu_0}|\nabla \times \mathbf{A}|^2 - \epsilon_0|\nabla\phi - \mathbf{A_t}|^2\end{aligned} \tag{5.67}$$

On the other hand, the mirror has its own kinetic and potential energies of pure mechanical nature due of its stiffness k and mass m, which gives the Lagrangian

$$\mathcal{L}_{mech} = \frac{1}{2}m\dot{u}^2 - \frac{1}{2}ku^2. \tag{5.68}$$

, where, u is the mirror axial displacement. Thus, assuming that the only non-zero derivatives are those with respect to the x propagation axis, the Hamilton's principle gives the total Action of system, which can be written as:

$$\begin{aligned}\mathcal{A}_{tot} &= \mathcal{A}_{mech}(u.\dot{u}) + \mathcal{A}_{em}(\phi_x, \mathbf{A}_t, \mathbf{A}_x) \\ &= S\int_{t_1}^{t_2}\left[\frac{1}{2}m\dot{u}^2(t) - \frac{1}{2}ku^2(t) + \left(\int_u^l \mathcal{L}_{e.m.}dx\right)\right]dt\end{aligned} \tag{5.69}$$

where ϕ_x is the first derivative with respect x of the scalar potential, while $\mathbf{A}_t = (A_{x,t}, A_{y,t}, A_{z,t})$ is the time derivative of the vector potential, and A_x, A_y, A_z represents the three components (here derived with respect to time). Then, the electric and magnetic fields for the one-dimensional case simplifies as:

$$\begin{aligned}|\mathbf{E}|^2 &= (\phi_x + A_{x,t})^2 + (A_{y,t})^2 + (A_{z,t})^2 \\ |\mathbf{B}|^2 &= (A_{y,x})^2 + (A_{z,x})^2\end{aligned} \tag{5.70}$$

According to variational principle, we must minimize the total action of the system, that is

$$\delta\mathcal{A}_{tot} = 0. \tag{5.71}$$

Thus, we must compute the variation for all the Lagrangian variable, which are δu, $\delta\phi$, δA_x, δA_y, δA_z. After some mathematics and using integration by parts, we

obtain the variation of the action as:

$$\begin{aligned}\delta\mathcal{A}_{tot} = &-\int_{t_1}^{t_2} \left(m\ddot{u}(t) + ku(t) + S\left[\mathcal{L}_{e.m.}\right]_u\right)\delta u dt \\ &+ S\int_{t_1}^{t_2}\int_u^l [2\epsilon_0(\phi_{xx} + A_{x,xt})\delta\phi + 2\epsilon_0(\phi_{x,t} + A_{x,tt})\delta A_x \\ &+ (2\epsilon_0 A_{y,tt} - \frac{2}{\mu_0}A_{y,xx})\delta A_y + (2\epsilon_0 A_{z,tt} - \frac{2}{\mu_0}A_{z,xx})\delta A_z] \\ &+ S\int_{t_1}^{t_2} \frac{2}{\mu_0}[A_{y,x}\delta A_y]_u^l + \frac{2}{\mu_0}[A_{z,x}\delta A_z]_u^l - 2\epsilon_0[\phi_x + A_{x,t}\delta\phi]_u^l dt\end{aligned} \tag{5.72}$$

where with the notation ϕ_{ii} and $A_{j,ik}$, with $i, j, k = x, y, z, t$ we refer to the second derivatives of the electromagnetic potentials. Here, the last integral represents the boundary terms. Thus, Hamilton's principle produces the coupled potential field equations:

$$\begin{aligned}\phi_{xx} + A_{x,xt} = 0 \\ \phi_{xt} + A_{x,tt} = 0,\end{aligned} \tag{5.73}$$

that can be combined together, eliminating A_x, obtaining:

$$\begin{aligned}\frac{1}{c^2}\phi_{tt} - \phi_{xx} = 0 \\ \frac{1}{c^2}A_{y,tt} - A_{y,xx} = 0 \\ \frac{1}{c^2}A_{z,tt} - A_{z,xx} = 0.\end{aligned} \tag{5.74}$$

This tells us that the potential fields propagate along x axis as a D'Alembert wave (without non-linearities). Then, the boundary conditions associated to equations 5.74 are determined by integration by parts in the Hamilton's principle, giving:

$$\begin{aligned}(\phi_x + A_{x,t})\delta\phi|_u = 0 \\ A_{y,x}\delta A_y|_u = 0 \\ A_{z,x}\delta A_z|_u = 0\end{aligned} \tag{5.75}$$

The additional boundary conditions for the mirror is:

$$\begin{aligned}m\ddot{u} + ku &= \mathcal{L}|_u \\ &= S\Big\{\frac{1}{\mu_0}\left[A_{x,y}^2 + A_{z,x}^2\right] - \epsilon_0\left[(\phi_x + A_{x,t})^2 + (A_{y,t})^2 + (A_{z,t})^2\right]\Big\}\Big|_u .\end{aligned} \tag{5.76}$$

In the equations 5.73, the integration of the first of equation with respect to x produces $\phi_x + A_{x,t} = F(t)$, while the integration of the second one with respect to time is $\phi_x + A_(x,t) = G(x)$, then it is possible to state that $F(t) = G(x) = const.$. Therefore, we can eliminate the static component and write the mirror equation of motion as:

$$\begin{aligned}m\ddot{u} + ku &= \mathcal{L}|_u \\ &= S\Big\{\frac{1}{\mu_0}\left[A_{x,y}^2 + A_{z,x}^2\right] - \epsilon_0\left[(A_{y,t})^2 + (A_{z,t})^2\right]\Big\}\Big|_u ,\end{aligned} \tag{5.77}$$

and the boundary conditions can be re-written as

$$\begin{cases} \phi|_u = 0 \\ A_{y,x}\delta A_y|_u = 0 \\ A_{z,x}\delta A_z|_u = 0 \end{cases} \tag{5.78}$$

From equation 5.74, we can write the potential fields at the mirror boundary as

$$\begin{aligned} \phi(x,t) &= \phi_i(x+ct) + \phi_r(x-ct) \\ A_y(x,t) &= A_{y;i}(x+ct) + A_{y;r}(x-ct) \\ A_z(x,t) &= A_{z;i}(x+ct) + A_{z;r}(x-ct) \end{aligned} \tag{5.79}$$

where ϕ_i, $A_{x,i}$, $A_{z,i}$ are known, while ϕ_r, $A_{x,r}$, $A_{z,r}$ are unknown. This allows to solve the reflection problem in terms of the four unknowns, in order to find the wave solution in the general propagation D'Alembert form, for the local non-resonant coupling model, by solving the system of equations:

$$\begin{aligned} m\ddot{u} + ku &= S\Big\{ \frac{1}{\mu_0}\left[A_{x,y}^2 + A_{z,x}^2\right] - \epsilon_0\left[(A_{y,t})^2 + (A_{z,t})^2\right] \Big\}\Big|_u \\ \phi|_u &= 0 \\ A_{y,x}\delta A_y|_u &= 0 \\ A_{z,x}\delta A_z|_u &= 0. \end{aligned} \tag{5.80}$$

From analytical model developed with the same technique, but for the case of acoustic waves, it has been observed that the nonlinear opto-mechanical coupling leads to generate some spurious frequencies in the rensponse of the mirror, thus in the reflected light spectrum [78]. This can be manipulated to both permits the theoretical analysis of the opto-mechanical coupling and to be useful for numerical simulations, with the final goal to tune an optimal control technique, suitable for the design of SIPS global control.

5.3.3 Pontryagin control equations

From this preliminary results, we foresee to apply a mathematical approach based on Pontryagin's maximum principle, in order to solve the main problem of control coupled dynamical systems. If the system is supposed to be linear (as has been considered in section 5.1), then the used standard methods are the Linear Quadratic Regulator (LQR) or the Linear Quadratic Gaussian (LQG) control. When the system is nonlinear, then the Pontryagin's method can be a suitable approach. This is clearly a more complicated approach, with respect to the techniques which make direct use of the transfer function (like the one used for Virgo and initially meant to be applied also for SIPS). Indeed, it presents some difficulties in producing the feedback control. Nevertheless, this method gives much more accurate results from the point of view of the system response to control actuation, allowing to find efficient control equation for complex systems like SIPS experiment. The prototype of the control problem is represented by the equations 5.80, of the previous section. The

control force must be considered in the equation of motion of mirror: in particular, the control vector has a single component f_c, which represents the control force applied to the mirror, operated by actuators (coil-magnet pairs in our case). Our first step will be to transform a partial derivative system (PDE) into an ordinal differential equation system (ODE), which is the simpler form for the study of a dynamical system. After, the equations for the evolution of the system can be written in the form

$$\dot{x} = Ax + Bf_c(s), \tag{5.81}$$

where the second term is related to the part of the system to be controlled with the actuation, and it is associated with a control matrix. Since we aim to realize a feedback control loop, it is important to define a criterion for the choice of the function $f_c(s)$, where s is the vector which represent signals from the sensors, and it will be associated to a sensing matrix. The idea is then to build a suitable *Objective Function*, J, which is a functional of the state of the system and of the control and gives information about the performance of the system. We can write J in a quadratic form as

$$J = \int_0^T (Qu^2 + Rf_c^2)dt \tag{5.82}$$

Then, we introduce a modified functional $\tilde{J}$, adding a constrain, as

$$\tilde{J}(\mathbf{x}, \mathbf{f_c}, \lambda) = \int_0^T \left[\mathcal{L} + \lambda^T(\cdot\mathbf{x} - A\mathbf{x} - B\mathbf{f_c})\right]dt, \tag{5.83}$$

with $\lambda = \lambda(t)$. Then, using the method of Lagrange multipliers, we must find the possible control vector $\mathbf{f_c}$ which satisfies the condition for which $\delta J \to 0$. The advantage of this model is that, even if now we have a more complicated system with three variable, $(\mathbf{x}, \mathbf{f_c}, \lambda)$, they are independent variables, then they can be easily obtained analytically. $\mathbf{f_c}$ must be in a range of value that will define the actuation ability of the system. In this way, it is possible to simultaneously obtain all the components of u, then all the control actuation, which in our case means being able to control mirrors motion in every direction and simultaneously, This results in the ability to build a simultaneous integrated feedback control, leading to an optimization of the performance of the system analysed in this thesis.

Conclusions

Quantum noise is one of the most important noises limiting the sensitivity of interferometric gravitational wave (GW) detectors. As a first solution to this limit, the frequency independent squeezing (FIS) technique was adopted by the current generation of GW detectors [79]. The main principle at the basis of this technique consists in injecting squeezed vacuum states from the detection port of the interferometer, which produces reduced fluctuation on one quadrature, due to the Heisenberg uncertainty principle, at the expense of increased fluctuation on the other quadrature. In such conditions, quantum shot noise at high frequency (above 200 Hz) can be reduced, an effect that can be also achieved by increasing the power stored in the arm-cavities. However, this choice implies the drawback of increasing quantum radiation pressure noise at low frequencies (typically below 100 Hz). The upgrades of the 2nd generation of GW detectors lead these instruments to face the limit due to the quantum nature of light, and it has been necessary to introduce FIS to observe quantum shot noise reduction above 200 Hz. At the same time, a small, but not negligible, quantum noise increase was observed at low frequency, due to amplitude noise [79]. These observations are consistent with the Heinseberg principle and the standard quantum limit (SQL). However, within such a framework, suitably manipulated squeezed vacuum states with a frequency-dependent squeezing angle (FDS) can be produced and injected into the asymmetric detection port, thus achieving a broadband quantum noise reduction. Very recent developments of Advanced Virgo foresee the use of FDS reached manipulating the squeezed vacuum state ellipse through an external 285 m long optical cavity [40].

In the meantime, we are developing a table-top experiment, called SIPS (Suspended Interferometer for Ponderomotive Squeezing), as a promising challenging alternative to filter cavity-based FDS. SIPS's final aim is to operate on squeezed vacuum states via the ponderomotive technique [57, 30]. This technique exploits the effect of radiation pressure in opto-mechanical cavities with suspended mirrors to generate a quantum correlation between phase and amplitude quadrature fluctuations, respectively related to shot noise and radiation pressure noise. In particular, the analysis of the opto-mechanical coupling in a detuned cavity allowed us to set the requirements for the choice of the parameters for the design of the experimental setup [57]. They must ensure a large squeezing factor and a suitable squeezing band. For this reason, the suspended mirrors should have the proper pendulum resonance below the frequency band of GW detectors, and the suspension system must be tailored in such a way that the thermal noise will be lower than the radiation pressure noise. Although originally designed with the main goal of generating ponderomotive squeezing, since

2018, SIPS has been chosen as the demonstrator of another frequency-dependent squeezing experiment that aims to reduce quantum noise through the injection of entangled vacuum states, i.e. Einstein Podolsky Rosen (EPR) states [62]. Hence, SIPS is planned to be used as a demonstrator for the EPR squeezing in a frequency band between 40 Hz and 700 Hz.

In this thesis, I performed both experimental work and theoretical studies devoted to the final goal of designing an optimized control system, for the control of the entire SIPS interferometer. An important part of the work carried out during these years of PhD, was devoted to the finalization of the experiment setup. Starting from the analysis done in [57], and from simulation on the noise budget for SIPS end mirror, it has been demonstrated that it is possible to obtain a table-top radiation pressure-limited ITF. Indeed, it has been found that the use of two optical cavities, with suspended mirrors of different low masses, is the optimal configuration allowing to keep the thermal noise low enough below the radiation pressure effect in the frequency range between 10 Hz and 10 kHz [57]. According to the requirements derived and described in this thesis, we expect to use SIPS experiment to generate tunable ponderomotive squeezing in a frequency range below 10 kHz. The mechanical and optical bench design has been described in detail in this work, together with the problematic linked to the mechanical feasibility of the experiment. With the optical and mechanical parameters chosen for the design of SIPS setup, we have seen that it is possible to obtain a squeezing factor $\zeta = 18$ dB, with an optical spring frequency of $\Theta = 2\pi$ kHz. Some experimental milestones have been also achieved.
In a preliminary phase, the local control system has been studied, developed, and tested on dummy elements that reproduce the main optics of the interferometer. The experimental work was slowed down because of some technical issues related to the real-time hardware used for local control operations that have been encountered during the test of the local control code. Moreover, the experimental work was retarded due to Covid-19 pandemic, which seriously impacted the production of the new mechanics. Nevertheless, some important results have been obtained, as already shown in figure 4.14: we are able to perform a pre-alignment of the 1 inch dummy end mirror, controlling its angular and linear motion, within an accuracy of 10 nrad and 0.1 μm RMS [30]. However, we learned that some improvements are needed both for local control itself and in view of the transition to the final design of SIPS experiment. This led to another aspect related to this issue, which is the design and realization of a new suspension system and mechanics tailored to optimize the actuation system for alignment and control. I designed a new marionette that allows the control of the pitch of the mirror without direct actuation on SIPS mirrors. Then, I took care of the design of the new monolithic suspension system for all the five mini-payloads. Recently, one end mini-payload of SIPS has been assembled and is ready for the new tests for the local control system, while the implementation on all the mini-payloads of SIPS should be realised in the following months.

As already mentioned, the manufacturing of new mechanics has being finalised only in November 2022, with a long delay due to unavoidable problems related to Covid-

19 pandemic, and only in December 2022 I was able to re-assemble the new mechanical components for one mini-payload placed at the end of one arm of SIPS. The mini-payload, at present, has been assembled adopting a suspended dummy mirror in order to check the mechanical behaviour. The readout electronics and the actuators to control the mini-payload, the electronics cabling for the sensing, and the actuation system to control it are now restored and ready for testing the performance of the local control improved with the new mechanics.

Another part of this thesis work, was devoted to the study for the optimization of SIPS global control. The high power circulating inside high finesse ($\mathcal{F}$=23000) SIPS Fabry-Perot cavities makes the design of an optimized control system a very challenging goal. The problem of the control of coupled dynamical systems has been studied, and an analytical model for the optomechanical interaction between mirrors and the wave field of the laser has been developed. The model presented in this thesis uses the equations of the wave field coupled with the resonator (end mirror) by the boundary conditions, with a variational approach. The final expressions of the wave field and the resonator motion $u(t)$ are determined, together with the boundary condition. The results can be manipulated to both permit the theoretical analysis of the opto-mechanical coupling and to be useful for numerical simulations, thus to tune an optimal control technique. From the analytical model, we will be able to apply Pontryagin's maximum principle, which allows finding efficient control equations for complex systems like the SIPS case, based on wave models close to boundaries (mirrors). This is proposed as an alternative approach on the control problem, with respect to those techniques that make direct use of the transfer function, which are the ones used for Virgo and also meant to be used in SIPS in its preliminary stage. Pontryagin's approach is a more complicated approach, but it gives more accurate results from the point of view of the system response to control actuation.

As mentioned in Chapter 2, a frequency dependent squeezing technique has been demonstrated in 2020 by [10]: this allowed to induce a rotation of the squeezing ellipse below 100 Hz using a suspended 300 meter long *filter cavity*. Nevertheless, this technique requires the use of long-scale filter cavity, which means a huge infrastructure for hosting its setup, and therefore high construction costs.

In the next future, FDS techniques will be applied to reduce the quantum noise in the second and third generation of interferometric gravitational waves detectors, like Advanced Virgo+ or Einstein Telescope (ET). Advanced Virgo+ adopted the filter cavity-based FDS technique. ET, which is still under design, in the case of FDS with filter cavities, will require 9 filter cavities on km scale (see figure 5.14). Thus, the development of a more compact FDS setup, such as the one proposed with SIPS and EPR experiments, will be of great advantage in view of the third generation detectors.

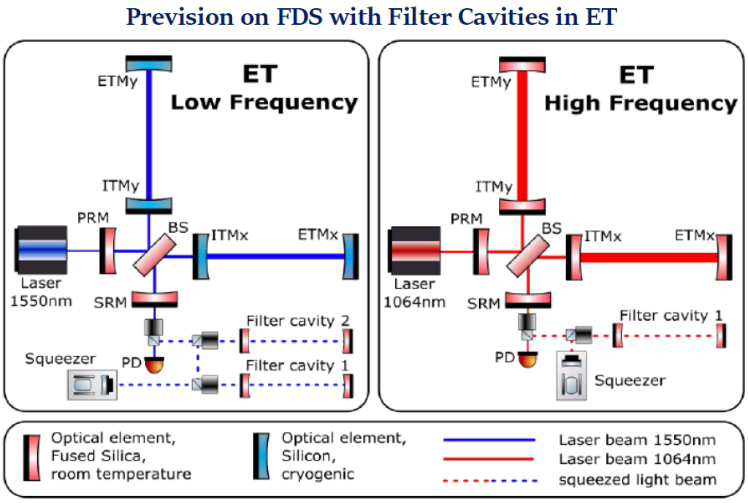

Figure 5.14: Frequency Dependent Squeezing prevision for filter cavity integration in ET design.

The work presented in this thesis still requires further investigation before being adopted for GW detectors, but it represents an important step toward the realization of an optimal control system for a complex system like SIPS. Moreover, as already mentioned, it seems a very promising alternative to current FDS techniques, especially in view of the construction of the third generation GW detectors.

Bibliography

[1] B P Abbott et al. "*Observation of Gravitational Waves from a Binary Black Hole Merger*". In: *Physical Review Letters* 16 (2016), p. 061102.

[2] C M Caves. In: *Phys. Rev. D* 23 (1981), pp. 1693–1708.

[3] R Slusher et al. In: *Phys. Rev. Lett.* 55 (1985), p. 2409.

[4] H Vahlbruch et al. In: *Classical and Quantum Gravity* 27 (2010), p. 084027.

[5] M Tse et al. In: *Phys. Rev. Lett.* 123 (2019), p. 231107.

[6] F Acernese et al. In: *Phys. Rev. Lett.* 123 (2019), p. 231108.

[7] F Acernese et al. In: *Phys. Rev. Lett.* 125 (2020), p. 131101.

[8] H Yu et al. In: *Nature* 583 (2020), pp. 43–47.

[9] S Chelkowski et al. In: *Phys. Rev. A.* 71 (2005), p. 013806.

[10] Yuhang Zhao et al. In: *Phys. Rev. Lett.* 124 (17 2020), p. 171101.

[11] L McCuller et al. In: *Phys. Rev. Lett.* 124 (2020), p. 171102.

[12] Y Ma et al. In: *Nature* 13 (2017), pp. 776–780.

[13] M Maggiore. *Gravitational Waves, Volume 1: Theory and Experiments*. New York: Oxford University Press, 2007.

[14] G Vajente. "Analysis of sensitivity and noise sources for the Virgo gravitational wave interferometer". PhD thesis. Scuola Normale Superiore di Pisa, 2008.

[15] J C Diaz. "Control of the gravitational wave interferometric detector Advanced Virgo". PhD thesis. University of Paris-Saclay, 2017.

[16] The Virgo Collaboration. "*Advanced Virgo Technical Design Report*". In: *Virgo internal note* VIR-0187A-16 (2016).

[17] H. Vahlbruch. "*Squeezed Light for Gravitational Wave Astronomy*". In: *PhD Thesis* (2008).

[18] R Kubo. In: *Reports on Progress in Physics* 29 (1966), pp. 255–284.

[19] E D Black. In: *American Journal of Physics* 69 (1 2001), pp. 79–87.

[20] D Bersanetti. In: *Eur. Phys. J. Plus* 133 (2018), p. 62.

[21] G Vajente. "Readout, sensing and control". In: *VESF School on Advanced Gravitational Wave Detectors* (2012).

[22] Virgo Collaboration. "Advanced Virgo Technical Design Report". In: VIR-0128A-12 (2012).

[23] F Acernese et al. In: *Class. Quantum Grav.* 32.2 (2015), p. 024001.

[24] T Accadia et al. In: *J. Low Freq. Noise V. A.* 30 (2011), pp. 63–79.

[25] S Di Pace and on behalf of the Virgo. "Status of Advanced Virgo and upgrades before next observing runs". In: *Phys. Scr.* 96 (2021), p. 124054.

[26] LIGO Scientific Collaboration and Virgo Collaboration. "*GW170817: Observation of Gravitational Waves from a Binary Neutron Star Inspiral*". In: *Physical Review Letters* (2017).

[27] F Sorrentino and J P Zendri. *Squeezing and QM techniques in GW Interferometers*. Handbook of Gravitational Wave Astronomy, 2021.

[28] Christopher Gerry and Peter Knight. *Introductory Quantum Optics*. Cambridge University Press, 2004. DOI: 10.1017/CBO9780511791239.

[29] H. P. Yuen. "*Two-photon coherent states of the radiation field.*" In: *Physical Review A* 13(6):2226 (1976).

[30] L Giacoppo et al. "Towards ponderomotive squeezing with SIPS experiment". In: *Phys. Scr.* 96 (2021), p. 114007.

[31] M. Vardaro. "*TOWARD A FULLY AUTOMATED AND DIGITALLY CONTROLLED SQUEEZED VACUUM SOURCE FOR GRAVITATIONAL WAVE DETECTORS*". PhD thesis. PhD Thesis, 2018.

[32] Yuen H P and Chan V WS. "*Noise in homodyne and heterodyne detection*". In: *Optics Letters* 8(3) (1983), pp. 177–179.

[33] V. Sequino. "*Development of a squeezed light source for the gravitational wave detector Advanced Virgo*". In: *PhD Thesis* (2016).

[34] Bachor H A and Ralph T C. *A Guide to Experiments in Quantum Optics*. Wiley, 2004.

[35] T Corbitt and N Mavalvala. In: *Journal of Optics B: Quantum and Semiclassical Optics* 6 (2004), S675–S683.

[36] V B Braginsky and F Ya Khalili. In: *Rev. Mod. Phys.* 68 (1996), pp. 1–11.

[37] T Corbitt et al. In: *Phys. Rev. A* 73 (2006), p. 023801.

[38] F Sorrentino and J P Zendri. In: *Contribution to Handbook of GW astronomy: Squeezing and QM techniques in GW Interferometers* (2019).

[39] R. W. Boyd. *Nonlinear optics*. Third edition-Academic Press, 2008.

[40] Valeria Sequino. "Quantum noise reduction in Advanced Virgo". In: *Physica Scripta* 96.10 (July 2021), p. 104014. DOI: 10.1088/1402-4896/ac0d30. URL: https://dx.doi.org/10.1088/1402-4896/ac0d30.

[41] Carlton M. Caves and Bonny L. Schumaker. "New formalism for two-photon quantum optics. I. Quadrature phases and squeezed states". In: *Phys. Rev. A* 31 (5 May 1985), pp. 3068–3092. DOI: 10.1103/PhysRevA.31.3068. URL: https://link.aps.org/doi/10.1103/PhysRevA.31.3068.

[42] Bonny L. Schumaker and Carlton M. Caves. "New formalism for two-photon quantum optics. II. Mathematical foundation and compact notation". In: *Phys. Rev. A* 31 (5 May 1985), pp. 3093–3111. DOI: 10.1103/PhysRevA.31.3093. URL: https://link.aps.org/doi/10.1103/PhysRevA.31.3093.

[43] Einstein A, Podolsky B, and Rosen N. In: *Phys. Rev.* 47 (1935), p. 777.

[44] W. P. Bowen, P. K. Lam, and T. C. Ralph. "Biased EPR entanglement and its application to teleportation". In: *Journal of Modern Optics* 50.5 (Apr. 2003), pp. 801–813. DOI: 10.1080/09500340308235187.

[45] Reid M D and Drummond P D. In: *Phys. Rev. Lett.* 60 (1988), p. 2731.

[46] Z. Y. Ou et al. "Realization of the Einstein-Podolsky-Rosen paradox for continuous variables". In: *Phys. Rev. Lett.* 68 (25 June 1992), pp. 3663–3666. DOI: 10.1103/PhysRevLett.68.3663. URL: https://link.aps.org/doi/10.1103/PhysRevLett.68.3663.

[47] Jing Zhang. "Einstein-Podolsky-Rosen sideband entanglement in broadband squeezed light". In: *Phys. Rev. A* 67 (5 May 2003), p. 054302. DOI: 10.1103/PhysRevA.67.054302. URL: https://link.aps.org/doi/10.1103/PhysRevA.67.054302.

[48] H J Kimble et al. In: *Phys. Rev. D* 65 (2001), p. 022002.

[49] V B Braginsky, A B Manukin, and M Yu Tikhonov. In: *Zh. Eksp. Teor. Fiz.* 58 (1970), pp. 1549–1552.

[50] C M Caves. In: *Phys. Rev. Lett.* 45 (1980), pp. 75–79.

[51] B S Sheard et al. In: *Phys. Rev. A* 69 (2004), p. 051801.

[52] S Di Pace. "Towards the Observation of Quantum Radiation Pressure Noise in a Suspended Interferometer: the QuRaG experiment". PhD thesis. University of Nice - Sophia Antipolis and University of Rome - La Sapienza, 2014.

[53] T P Purdy et al. In: *Phys. Rev. X* 3 (2013), p. 031012.

[54] N Aggarwal et al. In: *Nat. Phys.* 16 (2020), pp. 784–788.

[55] T Corbitt et al. In: *Phys. Rev. A* 74 (2006), p. 021802.

[56] L Naticchioni et al. In: *J. Phys.: Conf. Ser.* 957 (2018), p. 012002.

[57] S Di Pace et al. In: *Eur. Phys. J. D* 74 (2020), p. 227.

[58] Alessandra Buonanno and Yanbei Chen. "Signal recycled laser-interferometer gravitational-wave detectors as optical springs". In: *Phys. Rev. D* 65 (4 Jan. 2002), p. 042001. DOI: 10.1103/PhysRevD.65.042001. URL: https://link.aps.org/doi/10.1103/PhysRevD.65.042001.

[59] Alessandra Buonanno and Yanbei Chen. "Quantum noise in second generation, signal-recycled laser interferometric gravitational-wave detectors". In: *Phys. Rev. D* 64 (4 July 2001), p. 042006. DOI: 10.1103/PhysRevD.64.042006. URL: https://link.aps.org/doi/10.1103/PhysRevD.64.042006.

[60] G I Gonzalez and P R Sailson. In: *J. Acoust. Soc. Am.* 96 (1994), pp. 207–212.

[61] Yu Levin. In: *Phys. Rev. D* 57 (1998), pp. 659–663.

[62] S Di Pace et al. In: *Proc. 2nd GRAvitational-waves Science & technology Symposium (GRASS 2019), Padova, Italy* (2020). DOI: https://doi.org/10.5281/zenodo.3569196.

[63] A V et al Cumming. In: *Class. Quantum Grav.* 90.3 (2012), p. 035003.

[64] M Lorenzini and (on behalf of the Virgo Collaboration). In: *Class. Quantum Grav.* 27.8 (2010), p. 084021.

[65] F Acernese et al. In: *Astr. Part. Phys.* 20 (2004), pp. 617–628.

[66] S. Braccini and other. "Measurement of the seismic attenuation performance of the VIRGO Superattenuator". In: *Astroparticle Physics* 23.6 (July 2005), pp. 557–565. ISSN: 0927-6505. DOI: 10.1016/j.astropartphys.2005.04.002.

[67] G. Ballardin et al. "Measurement of the VIRGO superattenuator performance for seismic noise suppression". In: *Review of Scientific Instruments* 72.9 (2001), pp. 3643–3652. DOI: 10.1063/1.1392338. eprint: https://doi.org/10.1063/1.1392338. URL: https://doi.org/10.1063/1.1392338.

[68] Fiori I and Paoletti F. In: *Virgo internal note, VIR-0647B-10* (2017). URL: https://tds.virgo-gw.eu/?content=3&r=8207.

[69] F De Marco. "Optical design of the laser injection line into a small-scale suspended interferometer for Quantum Noise reduction in gravitational wave detectors". Master Thesis. Sapienza University of Rome, 2021.

[70] Yap M.J., Altin P., McRae T.G., et al. "Generation and control of frequency-dependent squeezing via Einstein–Podolsky–Rosen entanglement." In: *Nat. Photonics* 14 (2020), pp. 223–226. DOI: 10.1038/s41566-019-0582-4.

[71] Jan Gniesmer et al. "Frequency-dependent squeezed states for gravitational-wave detection through EPR entanglement". In: Optica Publishing Group, 2019, S2B.4. DOI: 10.1364/QIM.2019.S2B.4. URL: https://opg.optica.org/abstract.cfm?URI=QIM-2019-S2B.4.

[72] F Acernese et al. "A local control system for the test masses of the Virgo gravitational wave detector". In: *Astroparticle Physics* 20.6 (2004), pp. 617–628. DOI: 10.1016/j.astropartphys.2003.10.001.

[73] E Majorana. "AdV OpLev concept". In: *Virgo TDS* (2016). URL: https://tds.virgo-gw.eu/ql/?c=11375.

[74] M. Rakhmanov. "Dynamics of Laser Interferometric Gravitational Wave Detectors." PhD thesis. California Institute of Technology Pasadena, 2000.

[75] J. Doyle, B. Francis, and A. Tannenbaum. *Feedback control theory.* Macmillan Publishing Co., 1990.

[76] H.M. James, N.B. Nichols, and R.S. Phillips. *Theory of Servomechanisms.* Dover Publications; New Ed edition, 1965.

[77] S. M. Mahdi Alavi and Mehrdad Saif. *On stability analysis by using Nyquist and Nichols Charts.* 2015. DOI: 10.48550/ARXIV.1511.04752. URL: https://arxiv.org/abs/1511.04752.

[78] M. Boldrini et al. "Mechanical oscillator interacting with an acoustic or light beam: challenging nonlinear mechanical models". In: *ISMA-USD Noise and Vibration Engineering Conference*. 2022, pp 2577–2586.

[79] The Virgo Collaboration. "Gravitational wave detectors join forces for a new year-long signal hunt (start of O3 press release and figures)". In: (2019).